Chapter V

THE INSTRUMENT BACKGROUND

In this chapter I return to the instrument background. To show how one identifies it, isolates it or minimizes it through the ToF spectrum, the E2 spectrum and variations with veto-rates. An overview of the instrument background was presented in chapter III. I begin with a fit the ToF spectrum to the determine the ToF-peak rates that contained the CDG signal. In section V.B the total energy spectrum is discussed in the context of long-lived and prompt background. The components of the long-lived background are addressed next in section V.C. I sketch the E2 spectrum fitting method used to determine the radioactive isotope activity. In section V.D the veto-scaler measurement are introduced followed by a discussion of the prompt background and the veto-extrapolation technique used to estimate the prompt background in section V.E.

V.A. The ToF Spectrum

V.A.1 Overview

The ToF spectrum using livetime corrected Gamma-1 and Gamma-2 data is shown in figure V.A.1. The ToF spectrum can be described by gaussian-like peaks at around channel 80 and 120 on top of a broad continuum centered around channels 100. The peaks near channel 120 and 80 contain, the downward- and upward-scattered photons, respectively. These peaks correspond to a time-of-flight of ~±5.0 ns. The COMPTEL signal of external (cosmic) down-scattered events is contained in the peak at channel 120. The significance of the ToF measurement is seen by realizing that the down-scattered events constitute only a small fraction (about 10%) of the total events.

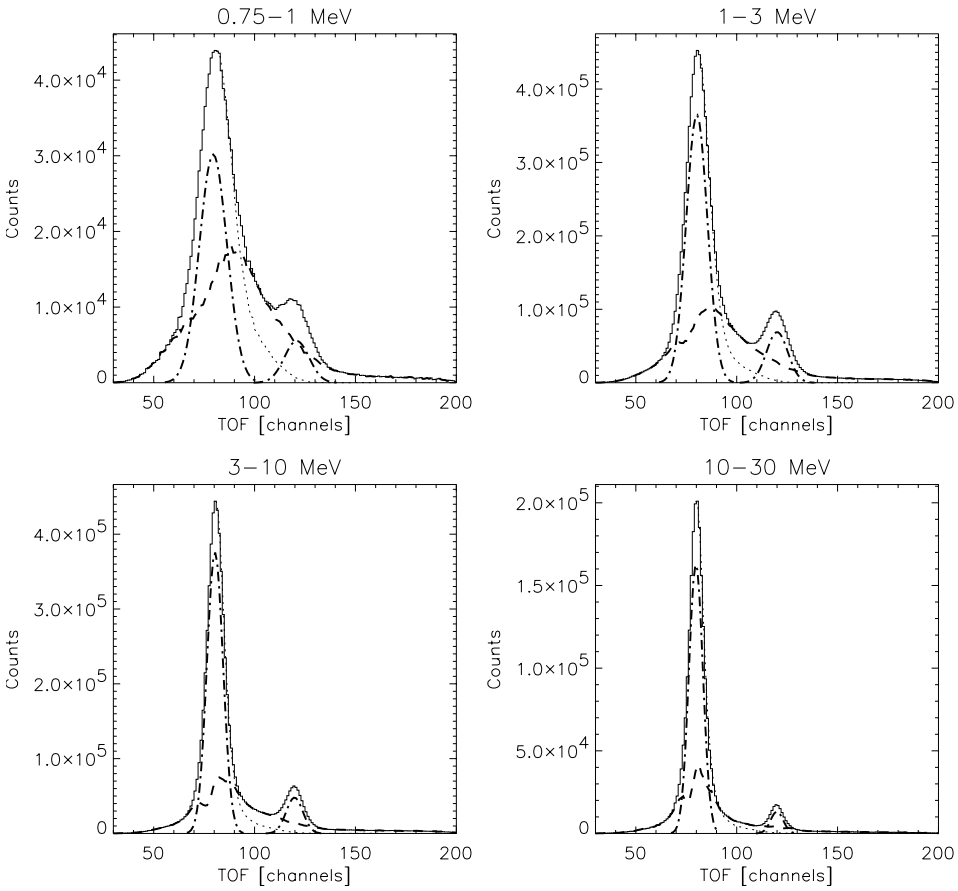

Figure V.A.1 The ToF spectrum accumulated over the entire coincidence time window using livetime corrected Gamma-1 and Gamma-2 data. Solid line: event data; dashed-dotted line: gaussian fits to the backward and forward peaks; dashed line: the remaining data after subtracting the gaussian fits from the data; dotted lines: the left wing of the backward peak mirrored on channel 80. The figure is reproduced with the permission of Rob van Dijk (1996).

V.A.2 The ToF Fit

The CDG signal is contained in the ToF-forward peak of Gamma-1 EVP data. The Gamma-1 data have restricted ToF values from ~100 to ~150 channels due to the on-board event selection criteria. The ToF spectra are fit above channel 108 to accurately determine the counts in the ToF-peak. This eliminates on a statistical basis a large fraction of the background due the ToF-continuum. In fitting the ToF spectrum, the forward-peak is modeled by a gaussian, positioned at channel 120, superimposed over a smooth continuum. Internal photon events of type A and type C produced in or around D1 also register events near ToF 120 and contribute to the peak. The ToF-continuum events are generally believed to consist of type B, C and D events. The ToF-continuum model is a constant (type B events)

plus an exponential function (representing multiple-photon events, type C and D). A generalized quadratic can also be used instead of the exponential since the true shape of the ToF-continuum is not known.

To study the behavior of the corrected-ToF spectrum with total energy, the ToF spectrum was fit for 30 logarithmic energy bins from 800 keV to 30 MeV. The ToF spectrum has been fit using two different models: Quadratic-ToF model and Exponential-ToF model.

The Quadratic-ToF model: The ToF spectrum with a gaussian plus a general quadratic. There are 6 free parameters in this model, where t is the ToF value in channels. The ToF fit range is channels 108–140 below ~7.5 MeV, channels 111–135 between 7.5–17.5 MeV and channels 109–135 above ~17.5 MeV. The ToF-peak width varies with energy therefore the ToF fit ranges are different since the fits are optimized to fit the forward peak.

$$\text{Quadratic–ToF} = P_1 + P_2 \times t + P_3 \times t^2 + P_4 \times \exp\left(-\frac{(t-P_5)^2}{2P_6^2}\right) \tag{5.1}$$

The Exponential-ToF model: The ToF spectrum with a gaussian plus a general exponential and a constant. There are 6 free parameters in this model. The ToF fit range is channels 108–145 below ~2.5 MeV and channels 108–140 above it.

$$\text{Exponential–ToF} = \exp(P_1 + P_2 \times t) + P_3 + P_4 \times \exp\left(-\frac{(t-P_5)^2}{2P_6^2}\right) \tag{5.2}$$

The constant (accidental) component is directly determined in the Exponential-ToF fits. Things are slightly more complicated when we want to determine the accidental events for the Quadratic-ToF model since we cannot directly separate the constant component from the normalization of the quadratic component. For the Quadratic-ToF model a separate fit to a constant is made at higher ToF channels (channels 140-145 below 9 MeV and channels 135-143 above 9 MeV) to determine the magnitude of the accidental component. There are now 6 plus 1 (=7) free parameters for the Quadratic-ToF model.

V.A.3 Results for the ToF Fits in ETOT

The ToF spectral fits using both the Exponential- and Quadratic-ToF models are shown below for different ETOT bins in figures V.A.2–5. These figures illustrate the quality of the ToF fits and the varying character of the ToF spectrum with ETOT (as discussed later).

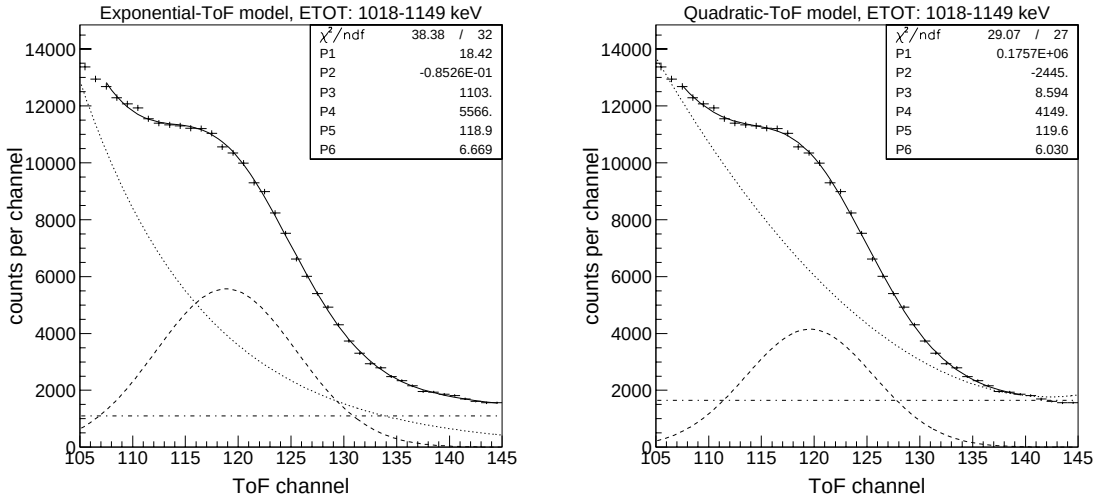

Figure V.A.2 The ToF fits for 1018–1149 keV in ETOT with the Exponential- and Quadratic-ToF model.

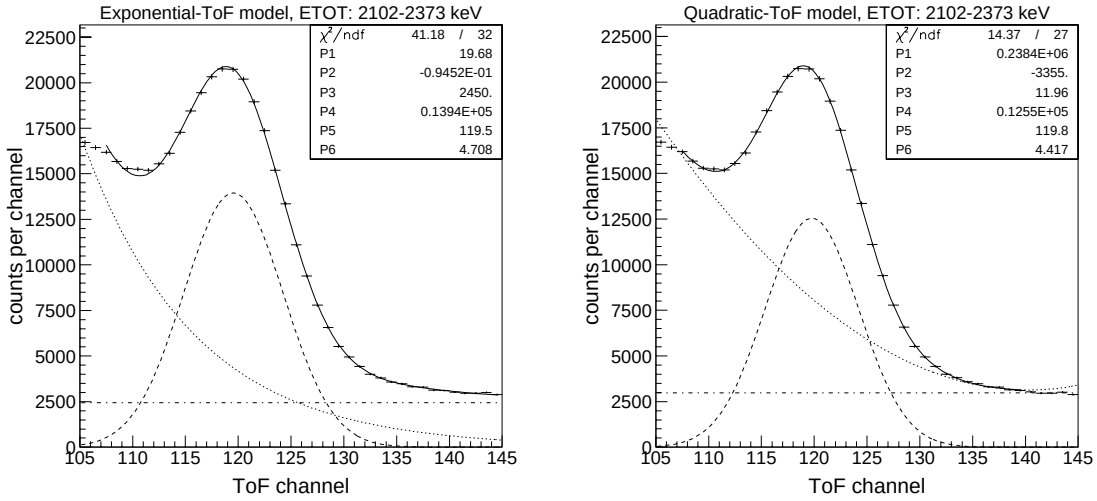

Figure V.A.3 The ToF fits for 2102–2373 keV in ETOT with the Exponential- and Quadratic-ToF model.

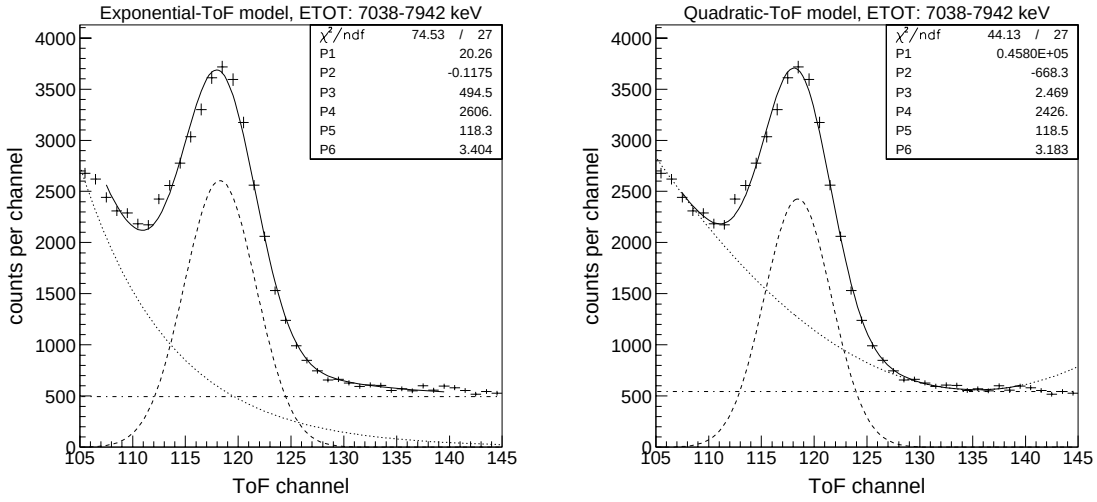

Figure V.A.4 The ToF fits for 7038–7942 keV in ETOT with the Exponential- and Quadratic-ToF model.

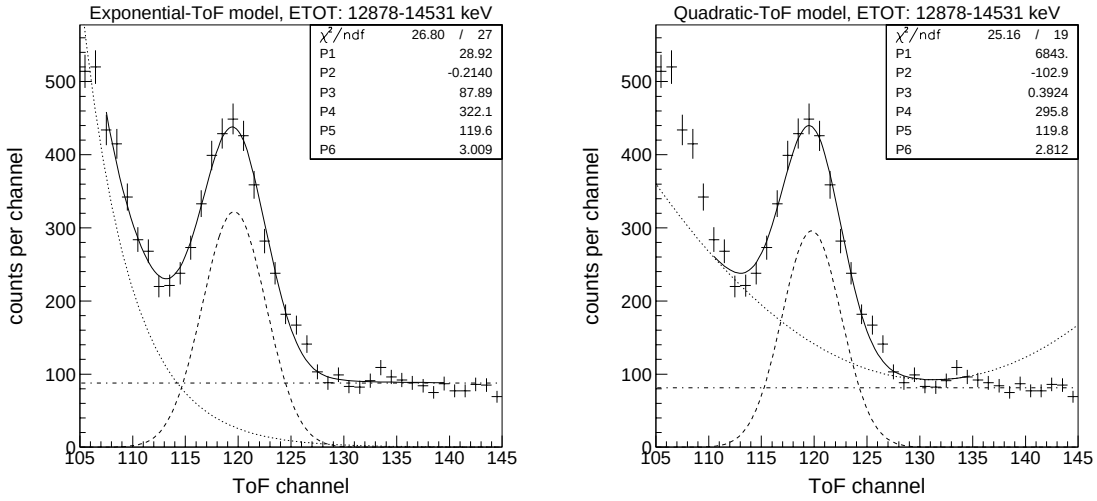

Figure V.A.5 The ToF fits for 12878–14531 keV in ETOT with the Exponential- and Quadratic-ToF model.

Both ToF fit models give acceptable ToF fits with reduced chi-square values (χ^2_ν) between 0.5 and 3 (figure V.A.6). Figures V.A.2–5 show that the fits adequately represent the data.

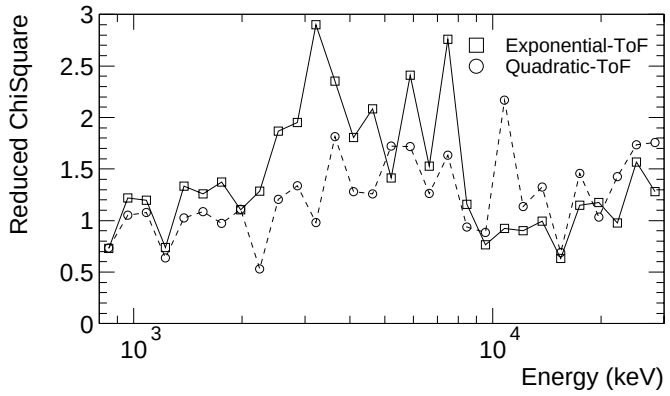

Figure V.A.6 The reduced chi-square values for the two different ToF models.

The forward-peak width (figure V.A.7) decreases monotonically with increasing energy up to about 9 MeV beyond which it is approximately constant. Some of this is due to the instrumental ToF resolution. The forward peak has a 1σ width that decreases from ~7 channels at 1 MeV to ~2.5 channels above 10 MeV. The widths for the Quadratic-ToF model are systematically smaller by ~0.5 channel. Below 1.5 MeV the difference increases to ~1–2 channels [see also Weidenspointner 1998].

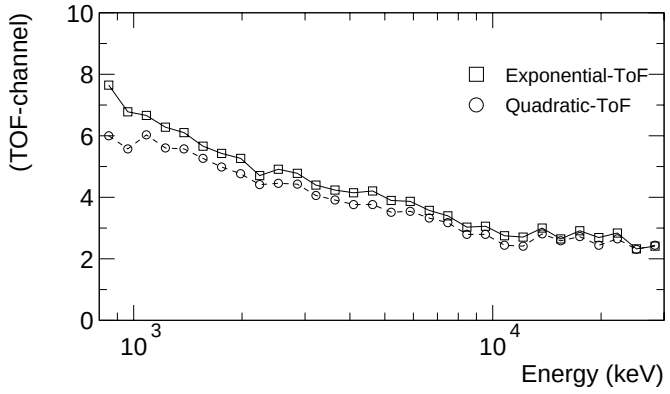

Figure V.A.7 The gaussian widths for the two different ToF models.

The peak position (figure V.A.8) exhibits a distinct walk in ToF space with total energy. The gaussian position has two regions where the position significantly deviates from the expected value of 120. Below 2 MeV the peak position shifts to channel 118.5 and then again

between 2.5 and 9 MeV where the peak position shifts to channel 118. Above 10 MeV and around 2.2 MeV the peak position is close to expected position of channel 120. Both ToF models show a similar walk with energy. The peak positions for the Quadratic-ToF model are systematically higher by 0.5 channel above 1.5 MeV. Below 1.5 MeV the difference increases to ~1–2 channels [see also Weidenspointner 1998].

Despite the ToF corrections, the peak position is shifted up to ~2 channels away from 120 at certain energies. The shift to lower channels in the forward-peak position at certain energies is associated with type C (multiple-photon) events dominating the counts at these energies, since type C events typically produce a ToF peak at a slightly lower channel number (section III.D). When the type A event mechanism dominates the counts, i.e., at 2.2 MeV, the peak position falls at channel 120. The position of the peak near channel 120 above 9 MeV suggest that at these energies type A events are once again the dominant event mechanism.

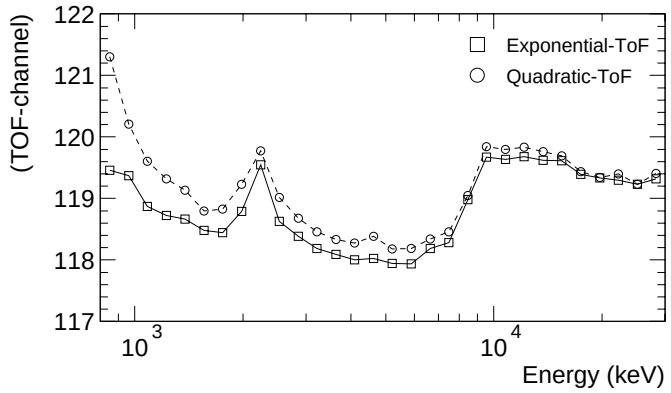

Figure V.A.8 The gaussian positions for the two different ToF models.

The peak amplitude is a measure of the counts in the forward peak. Both ToF models show similar trends for the peak amplitude (figure V.A.9) with total energy, however the Exponential model systematically predicts a ~25% higher amplitude. This effect is peculiar to the functions used in the two different fit models.

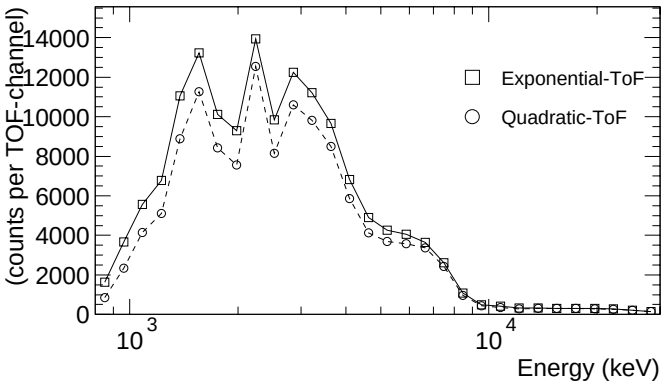

Figure V.A.9 The gaussian amplitudes for the two different ToF models.

The Exponential-ToF model systematically predicts a broader gaussian that has a lower peak position and a larger amplitude as compared to the Quadratic-ToF model. This behavior can be understood by examining the steepness of the two continuum functions, namely the exponential and the quadratic functions. The exponential is the steeper of the two, hence it tends to assign larger regions of ToF space to the gaussian making it broader with relatively higher counts; the quadratic being a flatter function is able to account for more of the ToF-continuum counts and leads to a narrower gaussian with relatively fewer counts.

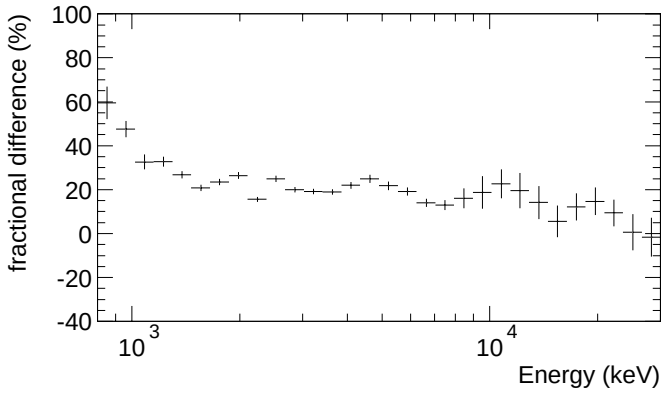

Figure V.A.10 The fractional difference in the ToF-peak rates between the two ToF-fit models.

The differences in the ToF fit functions leads the Exponential-ToF model to predict 20–30% larger area for the gaussian component as compared to the Quadratic-ToF model, see figure V.A.10. The differences are smaller above 9 MeV but increase to around 50% below 1.2 MeV. Since the total counts in the ToF spectrum is preserved by both ToF models, any differences in the gaussian counts is offset by the opposite difference in the ToF-continuum counts.

The counts assigned by the Exponential-ToF model to the exponential component is ~20% smaller (for all energies) than the counts assigned by the Quadratic-ToF model to the quadratic component, see figure V.A.11. The errors on the fitted parameters for the Exponential-ToF model are usually larger, especially above 9 MeV. The Quadratic-ToF model seems to be somewhat more robust with the fit parameters being better constrained. Above ~1.5 MeV, the ~20% decrease in the exponential component roughly cancels the ~20% increase in the gaussian counts in the Exponential-ToF model.

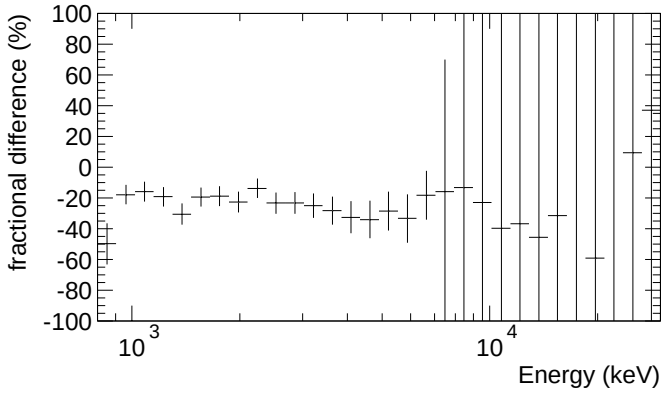

Figure V.A.11 The fractional difference in the quadratic and exponential rates between the two ToF-fit models.

The differences in the counts assigned to the constant component (accidentals) by the two models are small above 4 MeV. However, below 4 MeV the constant counts from the Exponential-model gets smaller with decreasing energy, see figure V.A.12. Below ~1.5 MeV, the ~50% decrease in the constant component in the Exponential-ToF model roughly cancels the ~50% increase in the gaussian counts.

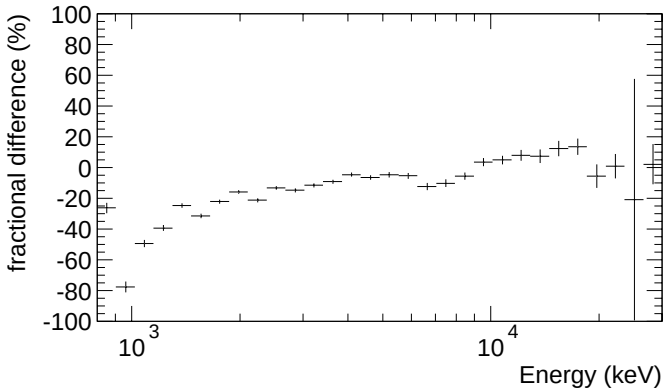

Figure V.A.12 The fractional difference in the constant component between the two ToF-fit models.

V.A.4 Exponential versus Quadratic ToF Model

The purpose of fitting the ToF spectra is to determine the ToF-peak count rates that include the cosmic photon event rate. A fundamental uncertainty in the ToF fits is that the true shape of the ToF-continuum is not known. The ToF spectra are fit over a narrower range (channels 108–140) rather than the full ToF coincidence window to optimize the fit to the gaussian. The exponential and quadratic functions are both approximations of the true shape of the ToF-continuum [see also Weidenspointner 1998]. For this work, the CDG spectrum is derived using both ToF models. The differences are used as a measure of the systematic uncertainties. For simplicity, only results from the Exponential-ToF model are discussed.

V.B. The Total Energy (ETOT) Spectrum

V.B.1 Prompt versus Long-Lived Background

The fitted ToF-peak rates consist of prompt and long-lived background components in addition to the contributions from the CDG signal. The COMPTEL event rate strongly depends on the orbital environment and has changed significantly over the first five years of the mission.

COMPTEL started the mission at an altitude of 450 km, decreasing slowly with each orbit. The orbit degraded to an altitude of 340 km by October 1993 at which point the first reboost raised the spacecraft back to 450 km. There was a second reboost in July 1997 (phase 6) that

moved COMPTEL from about 430 to 510 km, but data from phase 6 and 7 are not included in the analysis. The COMPTEL altitude history is plotted in figure V.B.1.

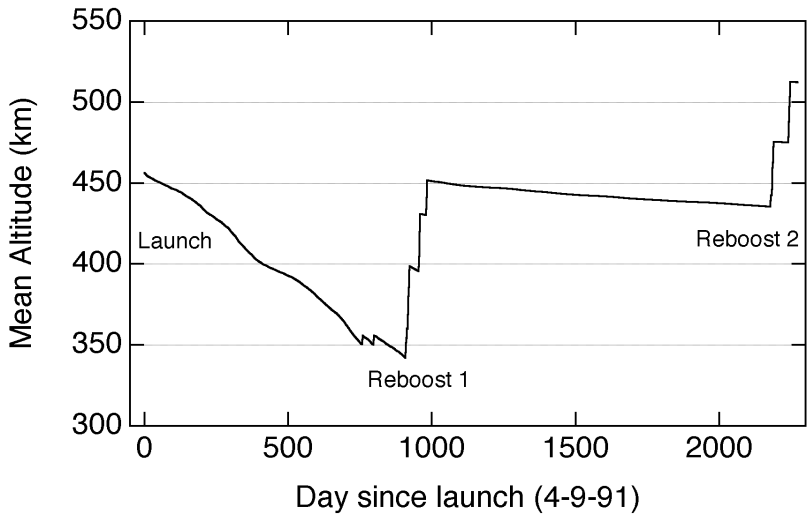

Figure V.B.1 The COMPTEL altitude history since launch.

The Phase 1 data represent the early mission with circular orbit of 450 km near Solar Maximum. Phase 2 data represent the pre-reboost period with lower circular orbits. The phase 3 data include the reboost period with a mixture of circular and elliptical orbits from 350–450 km. Phases 4 and 5 data are after the reboost with circular orbits of 450 km during Solar Minimum.

The total particle flux bombarding COMPTEL depends on the trapped radiation (SAA) and the cosmic-ray intensity. The primary cosmic-ray flux incident on the Earth, with rigidity less than ~1 GV, is modulated by solar activity. Heightened solar activity reduces the intensity of Galactic cosmic rays at Earth. For low-Earth orbits (350–500 km) the vertical cutoff-rigidity in orbit ranges from about 4 to 16 GV, above the solar modulation threshold. Therefore, the primary cosmic-ray intensity experienced by COMPTEL is relatively constant as should be the prompt background that depends only on the cosmic-ray intensity.

However, the SAA dose is influenced by both solar activity and the spacecraft altitude. The SAA dose increases with altitude but decreases with increased solar activity. An increase in solar activity heats the Earth's atmosphere, raising the atmospheric scale height that decreases the SAA dose compared to the same altitude at some lower solar activity level. Because the launch of CGRO occurred at solar maximum, the SAA dose decreases from the

beginning of the mission up to the first reboost (from phase 1 to phase 2) due to the decrease in altitude. Just after reboost in phase 3 the SAA dose increases significantly due to the sudden increase in altitude. From this level, the intensity again decreases from phase 4 to phase 5 due to the decrease in altitude. However, because of the differences in solar activity, the SAA dose is more intense in phase 4 as compared to that in phase 1, both of which are roughly the same altitude of 450 km.

Most of the radiation dose that produces the long-lived background occurs during the passage of the instrument through the SAA (Kurfess et al. 1989, Share et al. 1989, Varendorff et al. 1997). Although the trapped protons are of lower energy, their integrated intensity within the SAA is about 100 times the daily fluence of cosmic rays (Dyer et al. 1989). Therefore, depending on the individual isotope half-life, we expect the long-lived background components to vary. The different time dependencies of the prompt and long-lived components is used to identify energy ranges with and without long-lived background events.

V.B.2 The ToF-Peak Energy Spectrum: Phase-Separated Data

We can now use the ToF fit results to compute the average energy spectrum of the three ToF components, the peak, the continuum and the accidentals. To do this we must first integrate our fit functions over some ToF range and normalize them by the proper livetime of the telescope. I have used the total gaussian area and integrated the constant and exponential functions from ToF channels 110 to 130 to compute the counts assigned to each ToF component. The gaussian is mostly contained within the 110 to 130 ToF region, so integrating the constant and exponential functions in the 110–130 intervals makes the comparison between the components meaningful [see also Weidenspointner 1998].

Figure V.B.2 shows the ToF-peak spectra for the gaussian ToF components in the five individual phases. The two frames on the left are for 100 keV bins in ETOT from 800 keV to 4800 keV while the two on the right are for seven logarithmic bins in ETOT from 800 keV to 30 MeV (with 800–1200–1800–700–4200–7000–10000–30000 keV bin boundaries). The upper frames shows the absolute count spectrum for the individual phases whereas the lower

frames show the individual phase spectra normalized to the phase 2 spectrum. The normalization is made to the phase 2 data since it has the lowest SAA dose.

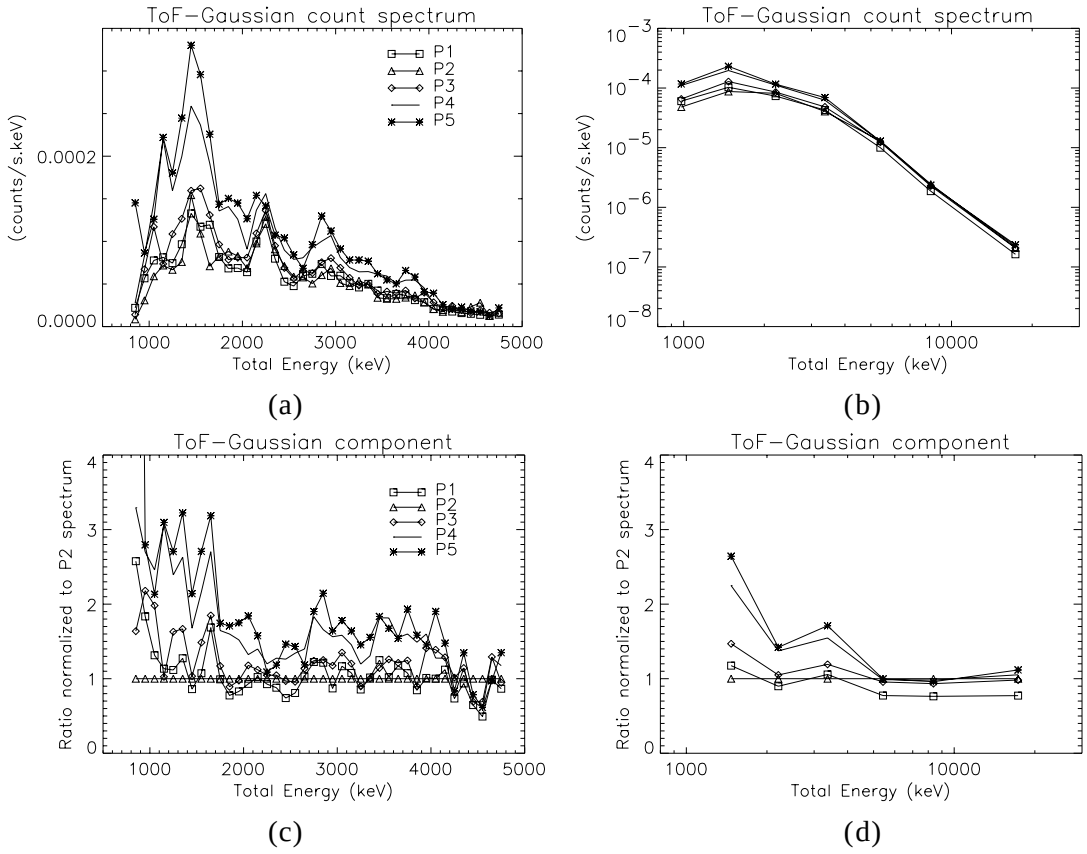

Figure V.B.2 The ToF-peak energy spectra for phase-separated data— (a) 800–4800 keV range in linear scale (b) 800–30000 keV range in logarithmic scale (c) 800–4800 keV range normalized to the Phase 2 spectrum (d) 800–30000 keV range normalized to the Phase 2 spectrum.

The instrument configuration appropriate to the phase 1 data (see chapter IV) results in a lower effective area and hence the phase 1 count spectrum is artificially lower compared to the others phases. The count rates above 4.2 MeV from all 5 phases are consistent with one another, the differences are less than 10–20% between the various phases. However below 4.2 MeV, there are large differences in the count rate between the phases. There is a dramatic change in the forward-peak spectrum for phases 4 and 5 after the reboost in phase 3. The time variability observed in forward-peak spectrum below 4.2 MeV suggests that it is influenced by the SAA. Therefore, there exists long-lived background events below 4.2 MeV in addition to the prompt component. This 4.2 MeV energy corresponds to the highest possible energy deposit of the ^{24}Na isotope, i.e., 1.368 and 2.765 MeV.

V.B.3 The ToF-Peak Energy Spectrum: Mission-Averaged Data

The P2345V total energy spectrum is averaged over long times periods with different activation rates. The energy spectrum is organized into three distinct energy regions (see figures V.B.3,4). These are the 0.8–4.2 MeV, 4.2–9 MeV and 9–30 MeV regions. The spectrum has a characteristic nuclear feature between 1 and 9 MeV. Since neutrons do not trigger the veto domes it suggests that the prompt-background is primarily produced by neutron-induced activation. However, the long-lived isotopes that produce the long-lived background can be due to neutrons or protons. The background above 9 MeV may contain electron- or photon-induced background events.

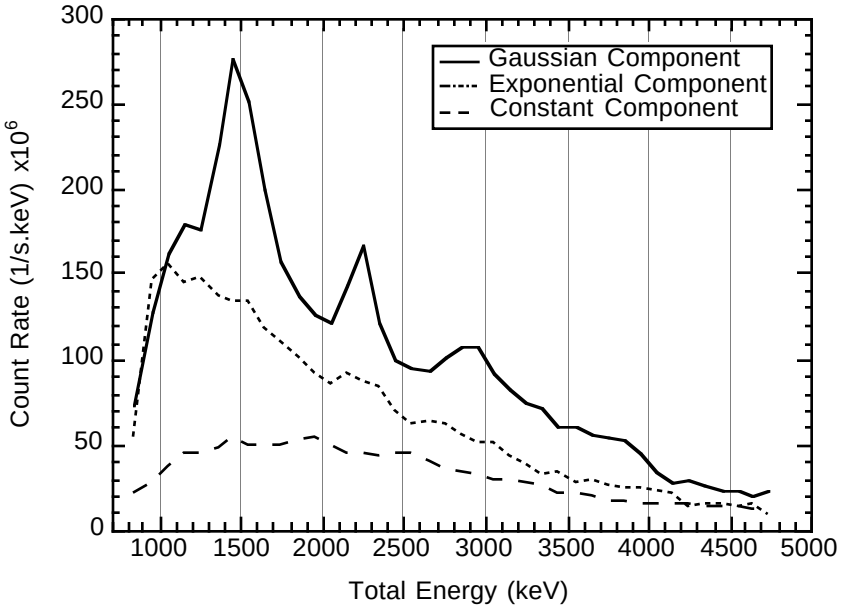

Figure V.B.3 The total energy spectrum for the P2345 Virgo data from 800–4800 keV.

Below 4.2 MeV, in the domain of long-lived events, the spectrum shows strong evidence for line (or structured) emission (figure V.B.3). There is also evidence for line-like emission near 1.4 and 2.2 MeV. The 1.4 MeV feature includes among other things events from ^{22}Na decay (type C event) and the ^{40}K decay (type A event). The 2.2 MeV is produced by thermal neutron capture by the hydrogen in the D1 scintillator and produces an intense prompt instrumental line (type A event). The ^{24}Na decay with two-photon decays produces the broad excess from 2.7 to 4.2 MeV (type C event). The energy spectrum below 4.2 MeV is discussed in section V.C. However, the important thing to note here is that the energy spectrum below 4.2 MeV shows line or structured emission from long-lived background components. Any

line emission from the Galaxy (e.g., 1.8 MeV) lies along the galactic plane whereas the data are from high-latitude pointings. Therefore, we assume that all line emission in the ToF-peak spectrum are from internal background photons [see also Weidenspointner 1998].

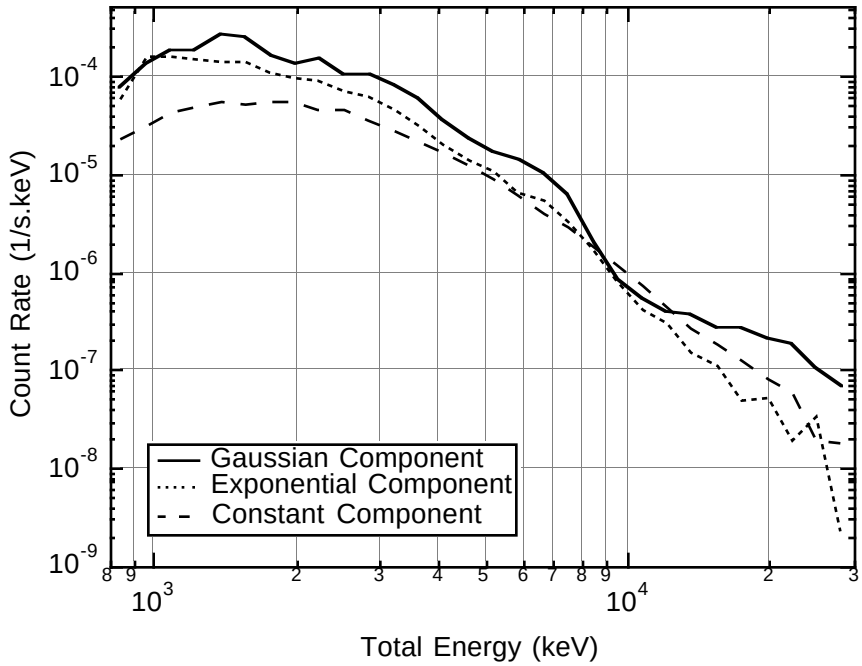

Figure V.B.4 The total energy spectrum for the P2345 Virgo data from 800–30000 keV.

Above 4.2 MeV, in the domain of the prompt background component, there is a broad and intense bump between 5 and 8 MeV (figure V.B.4). The spectrum is steep between 8–9 MeV. Above 9 MeV the spectrum hardens and becomes more intense (figure V.B.4). The sudden changes in the total energy spectrum at 4.2 and 9 MeV indicate changes in the physics/mechanisms of the instrumental photons being produced and registered (Ryan et al. 1997).

The change (hardening) of the spectrum above 9 MeV with a ToF-peak position at channel ~120 occurs beyond the nuclear energy regime, suggesting an electromagnetic component of prompt type A events. The events may arise from electron bremsstrahlung, electron-photon showers or pair-production in the veto covers or other material just outside the veto domes. The events span the entire energy range but are clearly observed above 9 MeV because the neutron-induced background is declining.

For energies between 4.2 and 9 MeV the ToF-peak position shifts to channel ~118 in ToF. As discussed in section III.D, type C events produce a ToF-peak at a slightly lower

channel number. The presence of the nuclear bump and the ToF shift suggests that events between 4.2–9 MeV are produced from cascading nuclear de-excitations where nuclei are excited to high quantum states by neutron collisions and then decay by multiple-photon emission on short time-scales ($\tau_{1/2}$ << 1ns). The prompt component contains two ToF peaks in the ToF spectrum: the first at channel 120 from photons the are produced outside the veto-domes by type A mechanism and the second at channel ~116 by multiple-photon emission originating from the mass surrounding D1 detector array by type C mechanism. The two-peaks when modeled with a single gaussian gives a ToF-peak position near channel 118. A two-gaussian ToF model is discussed in more detail in section V.D and is used in the CDG analysis between 4.2 and 9 MeV to extract the counts in the ToF-peak at channel 120.

V.B.4 The Energy Spectra for the Exponential and Constant Components

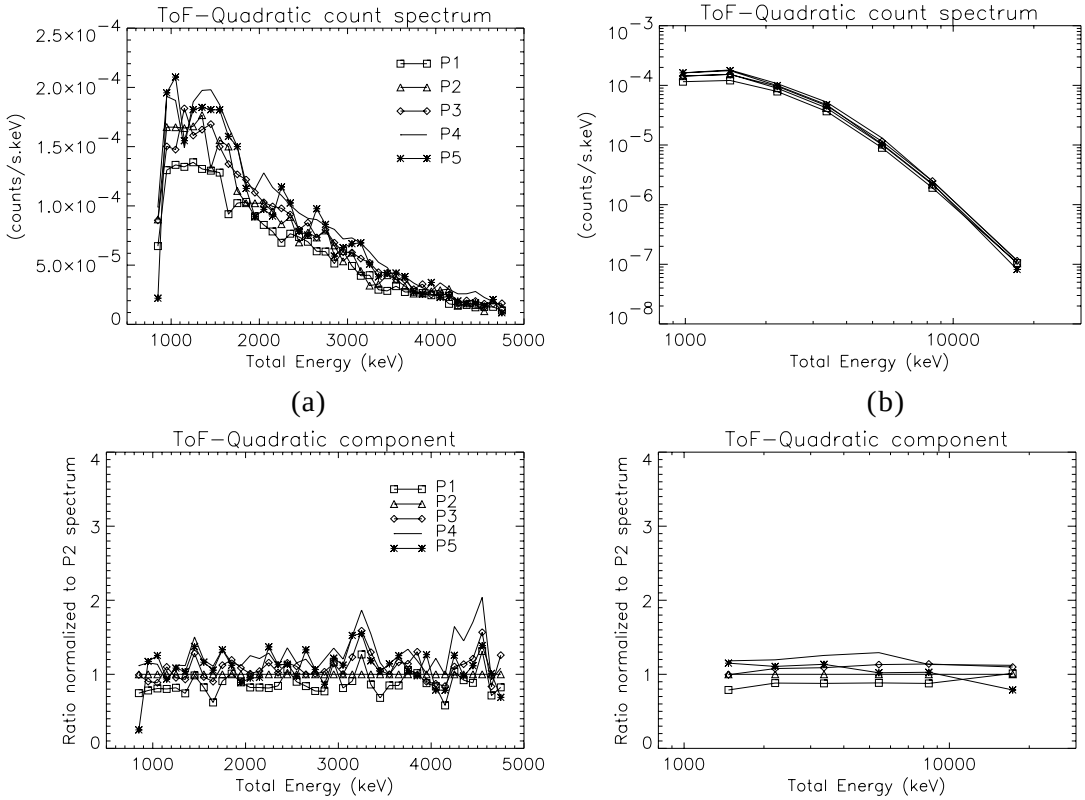

Figure V.B.5 The ToF-quadratic energy spectra for phase-separated data— (a) 800–4800 keV range in linear scale (b) 800–30000 keV range in logarithmic scale (c) 800–4800 keV range normalized to the Phase 2 spectrum (d) 800–30000 keV range normalized to the Phase 2 spectrum.

Figures V.B.5 and V.B.6 show the ETOT count spectra for the quadratic (similar to the exponential) and constant ToF components for the 5 individual phases, respectively. The description of the four frames in these figures are similar to those of figure V.B.2.

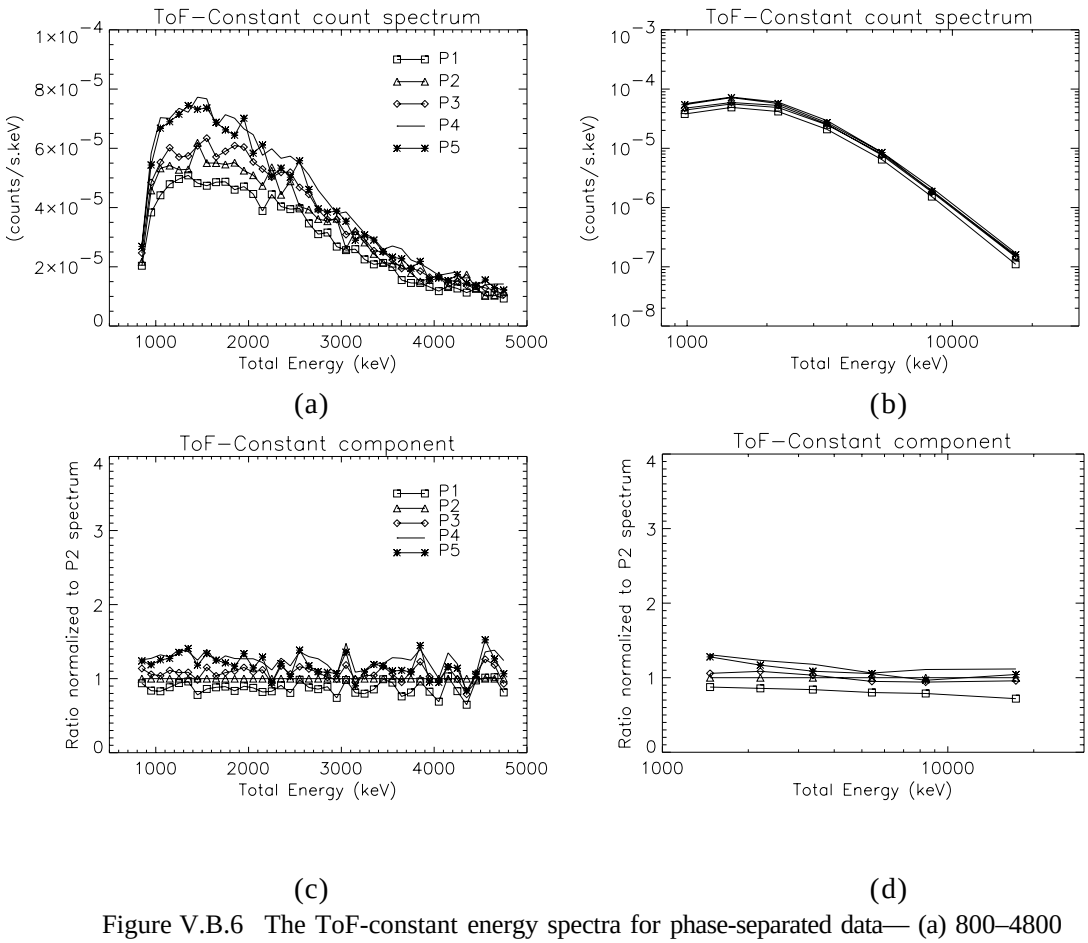

Figure V.B.6 The ToF-constant energy spectra for phase-separated data— (a) 800–4800 keV range in linear scale (b) 800–30000 keV range in logarithmic scale (c) 800–4800 keV range normalized to the Phase 2 spectrum (d) 800–30000 keV range normalized to the Phase 2 spectrum.

The energy spectra for the quadratic component are similar for the different phases and relatively featureless. Comparing the spectra with each other shows variations of ~20% between the different phases (figure V.B.5). Likewise the constant (accidentals) have a similar spectral shape and intensity in all of the phases (figure V.B.6). Again the phase 4 and 5 data are higher below 2 MeV. Unlike the ToF-peak component below 4.2 MeV (figure V.B.2a), the quadratic (figure V.B.5a) and accidental (figure V.B.6a) spectra lack variability on long timescales (at least above 2 MeV). This suggests that the quadratic and constant events are mostly prompt in nature.

The time-averaged spectra for the constant and quadratic components (figures V.B.3 and V.B.4), unlike the ToF-peak component, show no drastic change in their spectrum near 4.2 or 9 MeV nor any strong line emission features below 4.2 MeV. Since the ToF continuum (quadratic plus accidentals) lacks a clear nuclear signature, other background photon production processes also play an important role, e.g., pion decays or electron bremsstrahlung or photons from proton-induced showers in other parts of the spacecraft (any place outside the veto-domes). Therefore, in addition to geometry differences, there are also spectral (physics/mechanism) differences between the ToF components.

V.C. The Long-Lived Background Component

V.C.1 Overview

By definition the long-lived background events are from the decay of radioactive isotopes with long half-lives ($\tau_{1/2}$ > 1–10 min.). These radioactive isotopes with long half lives preferentially de-excite through beta decay and emit photons at discrete energies. Since registered telescope events require energy loss in both the upper and lower detectors, those radioactive decays that involve two or more decay photons that interact separately in the individual detectors (type C multiple-photon event), have a high efficiency of producing a valid telescope event.

In principle, photons from single-photon decays can also scatter off D1 into D2 (type A events) resulting in telescope events but with larger scatter angles. The standard CDG FoV selections accept only those events with small scatter angles (ϕ<38˚). This effectively eliminates most single scatter (type A) background events (with the exception of the 1.46 and 2.223 MeV photons). However single-photon decays occur where the beta particle has sufficient energy to produce a second photon through the bremsstrahlung process, leading to multiple-photon events (type C).

Since the long-lived background contributions from type A events are rare, the type C mechanism is the main channel for long-lived background event production with one of the decay lines being measured in the D2 detector. Therefore, the process of identifying the radioactive isotopes involves identifying photopeaks in the E2 (or ETOT) spectrum. The behavior of any characteristic decay lines or features in the data are investigated by applying

data selections that first enhance them. Since the activation is most intense as the spacecraft passes through the SAA, selecting appropriate times after SAA passage or comparing data with different activation histories also can aid in identifying the long-lived radioactive isotopes. Once we identify these isotopes, Monte Carlo simulations of the decay products (photons, $\beta^{\pm}$) can be used to determine their distribution in COMPTEL dataspace. The results from the simulations of the identified long-lived background components are shown in the following sections for standard energy threshold settings together with the CDG FoV selections to illustrate the specific structure of these events with the CDG data selections. The CDG FoV selections are effective in eliminating much of the background.

The variety of isotopes that produce the long-lived background components depends on the material in which the activation occurs. Aluminum is by far the most common element in COMPTEL (and the spacecraft) and is a major site for activation. Of particular importance is the activation in the D1 platform and the D1 housing since these photons have a favorable geometry for producing type C events. The other common elements in COMPTEL include Cu (from the wiring harness), Si and O (from the D1 PMTs and the D1 quartz windows). A partial list of the identified long-lived background isotopes is shown in table V.C.1.

Table V.C.1 A list of the identified long-lived parent isotopes.

Parent Isotope	half-life ($\tau_{1/2}$)	decay-mode and photon energies (MeV)	Production channel
^{24}Na	15.02 h	β^- (1.39) E_γ=1.368, 2.754	^{27}Al(n,α) ^{27}Al(p,3pn)
^{22}Na	2.60 y	90.5% β^+ (0.55) 9.5% EC E_γ=1.274	^{27}Al(p,3p3n) + others
^{28}Al	2.24 m	β^- (2.87) E_γ=1.779	^{27}Al(n,γ) ^{28}Si(n,p)
^{27}Mg	9.46 m	β^- (1.6–1.75) 28% E_γ=1.014 72% E_γ=0.844	^{27}Al(n,p)
^{40}K	1.28×10^9 y	10.5% EC E_γ=1.461	Natural

V.C.2 The ^{24}Na Isotope

The ^{24}Na decay is one the most intense sources of activation events. The methods developed to identify and correct for its contribution are similar to that used for other isotopes.

Production: The ^{24}Na isotope is primarily produced by fast n interactions with Al. The reaction threshold energy is E_n >3.13 MeV. The cross-section is greatest for 8–30 MeV neutrons with a maximum of ~100 mb for $E_n \approx 14$ MeV. The ^{24}Na nucleus undergoes beta decay with a $\tau_{1/2}$ = 15.02 hours to an excited state of ^{24}Mg*. ^{24}Mg* promptly decays to the ground state ($\tau_{1/2}$ ~25 fs, 1.4 ps) by emission of two cascade photons with energies at 1.368 and 2.754 MeV. The emitted beta has an end-point energy of 1.39 MeV.

$^{27}Al + n \rightarrow {}^{24}Na^* + \alpha$

$^{24}Na^* \rightarrow {}^{24}Mg^* + \beta^- \rightarrow {}^{24}Mg + 1.368 \text{ MeV } \gamma + 2.754 \text{ MeV } \gamma$

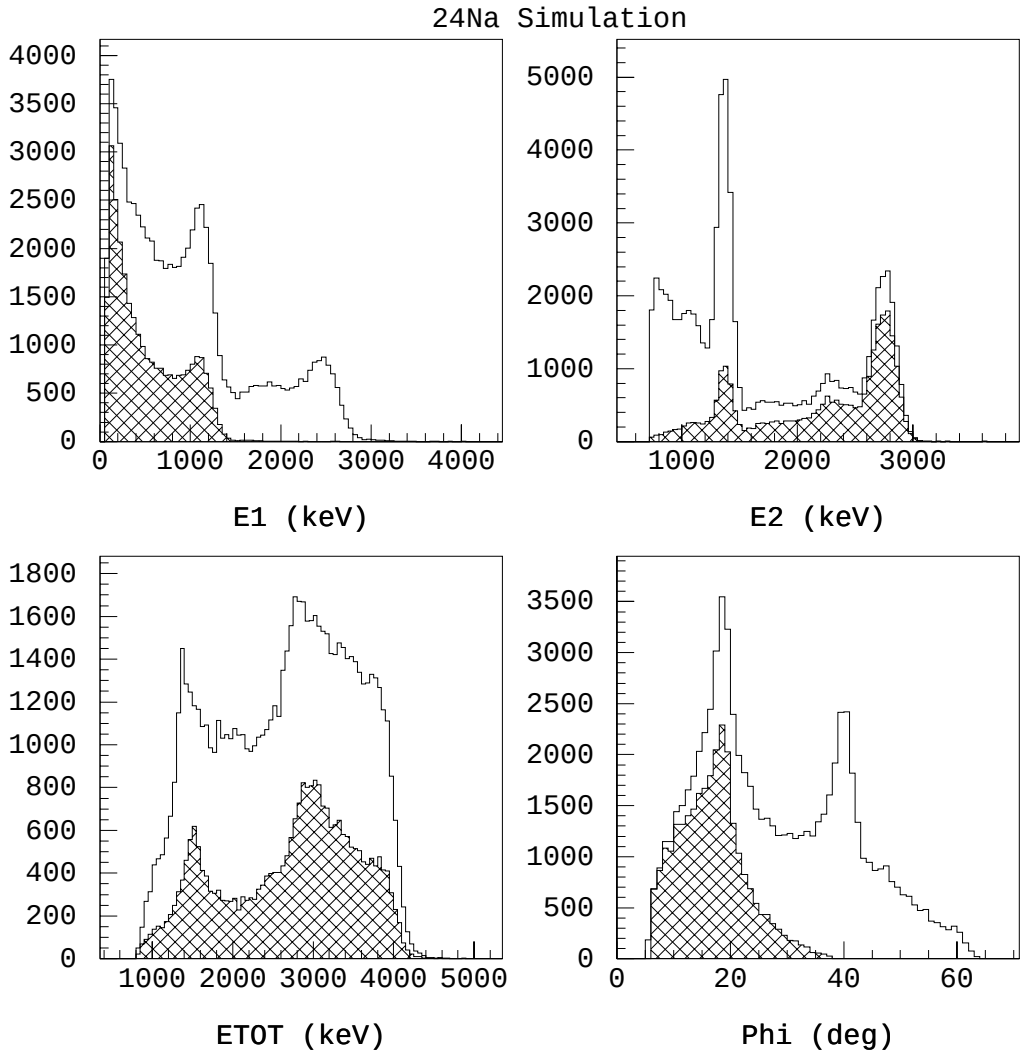

Figure V.C.1 The COMPTEL response to the ^{24}Na decay. The line histograms are for standard CDG threshold selections while the solid histogram includes the CDG FoV section.

Dataspace signature: The COMPTEL response to ^{24}Na decay is shown in figure V.C.1. When one photon interacts in D2 and the other triggers D1, a telescope event is registered. The photopeaks associated with each of the photons interacting in D2 and the Compton edge energy for the photons in D1 are clearly seen in the ^{24}Na simulation spectra. When the 2.754 MeV photon produces a photopeak events in D2 and the 1.368 MeV photon produces a Compton-edge D1, a nominal ϕ of 18˚ is measured, juxtaposing the photon energies gives a ϕ of 40˚ (see ϕ spectrum in figure V.C.1). The key signatures used to identify the ^{24}Na component are the photopeaks in E2 and two peaks at 18˚ and 40˚ in the ϕ spectra.

The FoV and ϕ restrictions in the standard-CDG selections severely suppress the latter channel (1.368 in D2 and 2.754 in D1). The channel where the 2.754 MeV photon interacts in E2 results in a broad feature from 2.8 to 4.2 in ETOT after the CDG selections. The 2.754 MeV photopeak in E2 is used to estimate the ^{24}Na activity. The 1.3 MeV line feature in E2 data also contains photons from other isotope decays and is therefore more intense than expected from simulations. The beta has a moderately high end-point energy and can produce a third photon by bremsstrahlung albeit with lower efficiency. All these processes are computed in the simulations [see also Weidenspointner 1998].

Although fast neutrons from the Earth are present during the entire orbit, their intensity is much higher in the SAA. Hence the ^{24}Na isotope is activated predominantly in the SAA passages. The ^{24}Na activation dependence on SAA dose can be accurately modeled as shown in figure V.C.2 (Varendorff et al. 1997). The ^{24}Na activation dependence on SAA dose is also seen in the SMM data (Kurfess et al. 1989). The activity of ^{24}Na is shown in figure V.C.9.

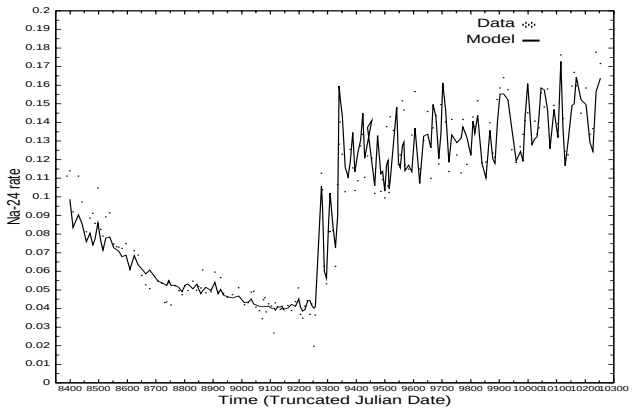

Figure V.C.2 The measured ^{24}Na rates with the ^{24}Na activation model. Figure reproduced with permission of Varendorff et al. (1997).

V.C.3 The ^{22}Na Isotope

The ^{22}Na isotope was identified (Oberlack 1998; Weidenspointner 1998) during the analysis of the Galactic 1.8 MeV line (^{26}Al). The ^{22}Na simulations show clear line-like emission at 1.275 MeV in E2. However contamination from other isotopes (^{40}K and ^{24}Na) is also present at these energies.

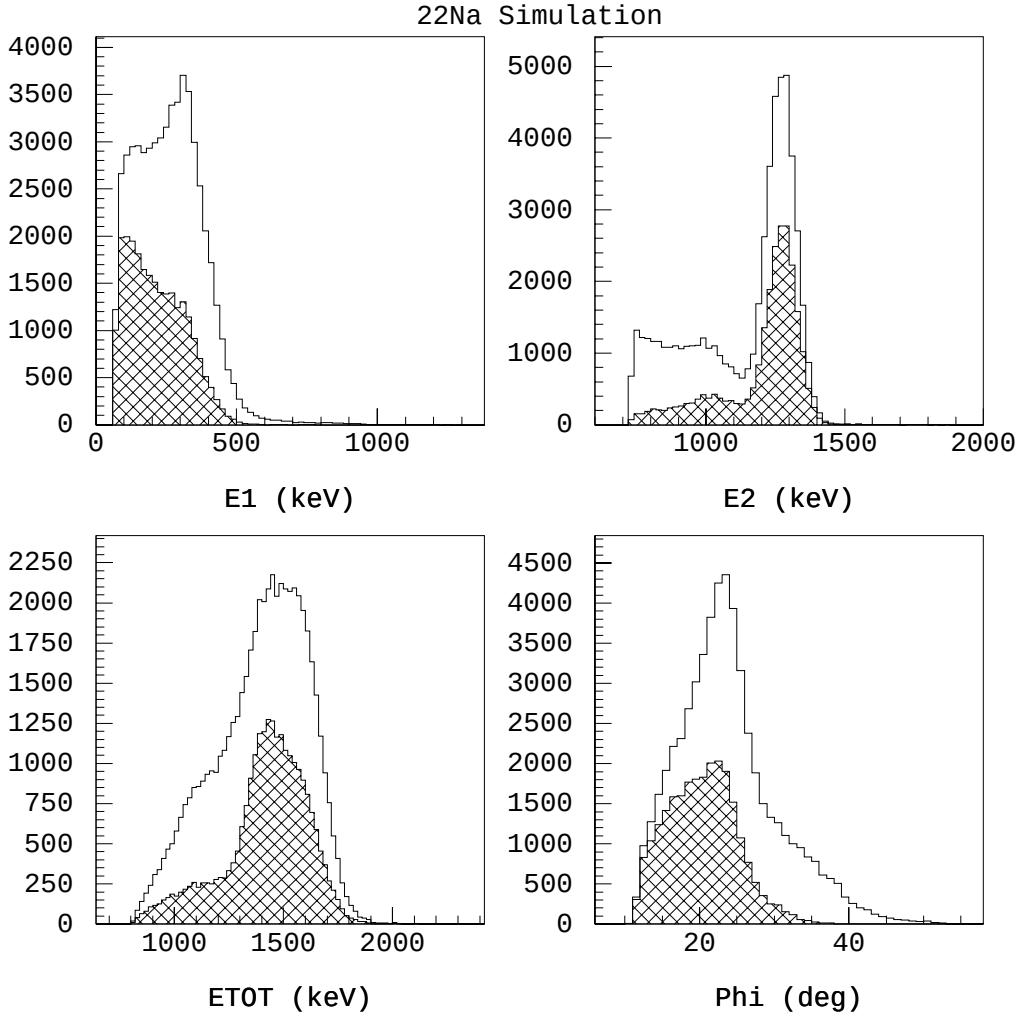

Figure V.C.3 The COMPTEL response to the ^{22}Na decay. The line histograms are for standard CDG threshold selections while the solid histogram includes the CDG FoV section.

Production: ^{22}Na is produced primarily by the ^{27}Al(p,3p3n)^{22}Na channel. ^{22}Na decays with a $\tau_{1/2}$ = 2.6 years to an excited state of ^{22}Ne* by two decay modes: β^+ (90.5%) and EC (9.5%). ^{22}Ne* promptly decays ($\tau_{1/2}$ = 3.7 ps) to the ground state by the emission of a 1.274 MeV photon.

^{27}Al (p, 3p 3n) ^{22}Na*

^{22}Na* $\rightarrow$ ^{22}Ne* + β^+ $\rightarrow$ ^{22}Ne + 1.275 MeV γ

The ^{22}Na isotope that give telescope events in the forward peak is believed to arise from proton interactions ($E_p \geq 35$ MeV) with the Al structure of the instrument. Most of the ^{22}Na activation occurs within the SAA where there is a large flux of trapped protons below ~100 MeV. The ^{22}Na activation dependence on SAA dose can be accurately modeled (Varendorff et al. 1997). The activity of ^{22}Na events is shown in figure V.C.9. The usual channel of ^{22}Na production from stable ^{23}Na is not a problem since all the ^{23}Na lies in the D2 detector. Such events are readily excluded by ToF selections.

Dataspace signature: The COMPTEL response to ^{22}Na decay is shown in figure V.C.3. The β^+ annihilates to produce two 0.511 MeV photons, one of which together with the 1.274 MeV photon produces type C background events. Since the annihilation photon does not exceed the E2 threshold, all ^{22}Na events will have the 1.275 MeV photon photopeak in E2. Due to the low end-point energy for the beta particle (0.545 MeV), the probability of it producing significant bremsstrahlung photons is low. The lack of the 1.275 photopeak in ETOT indicates that type A events from the 1.274 MeV photons are rare.

V.C.4 The ^{2}H Neutron-Capture Line

Production: Thermal neutron-capture by hydrogen in the D1 scintillators produces a prompt 2.223 MeV photon. The capture time has a mean value of ~100 μs (White and Schönfelder 1975). These 2.2 MeV photons can Compton-scatter in D1 and interact in D2 to produce type A events.

Dataspace signature: The COMPTEL response to 2.223 MeV neutron-capture line is shown in figure V.C.4. The 2.2 MeV events are detected with high efficiency and result in a strong prompt instrumental line in ETOT. Its prompt nature (see section V.E) and dependence on orbital parameters has been examined (Weidenspointner et al. 1996). The COMPTEL response to 2.2 MeV photon is characteristic of its response to all type A events; the 2.2 MeV photopeak is seen only in ETOT with continuum spectra for the individual E1 and E2 detectors. The daily 2.2 MeV rate is stable with time (see section V.E, figure V.C.9), indicative of a constant cosmic-ray intensity and stable prompt background behavior.

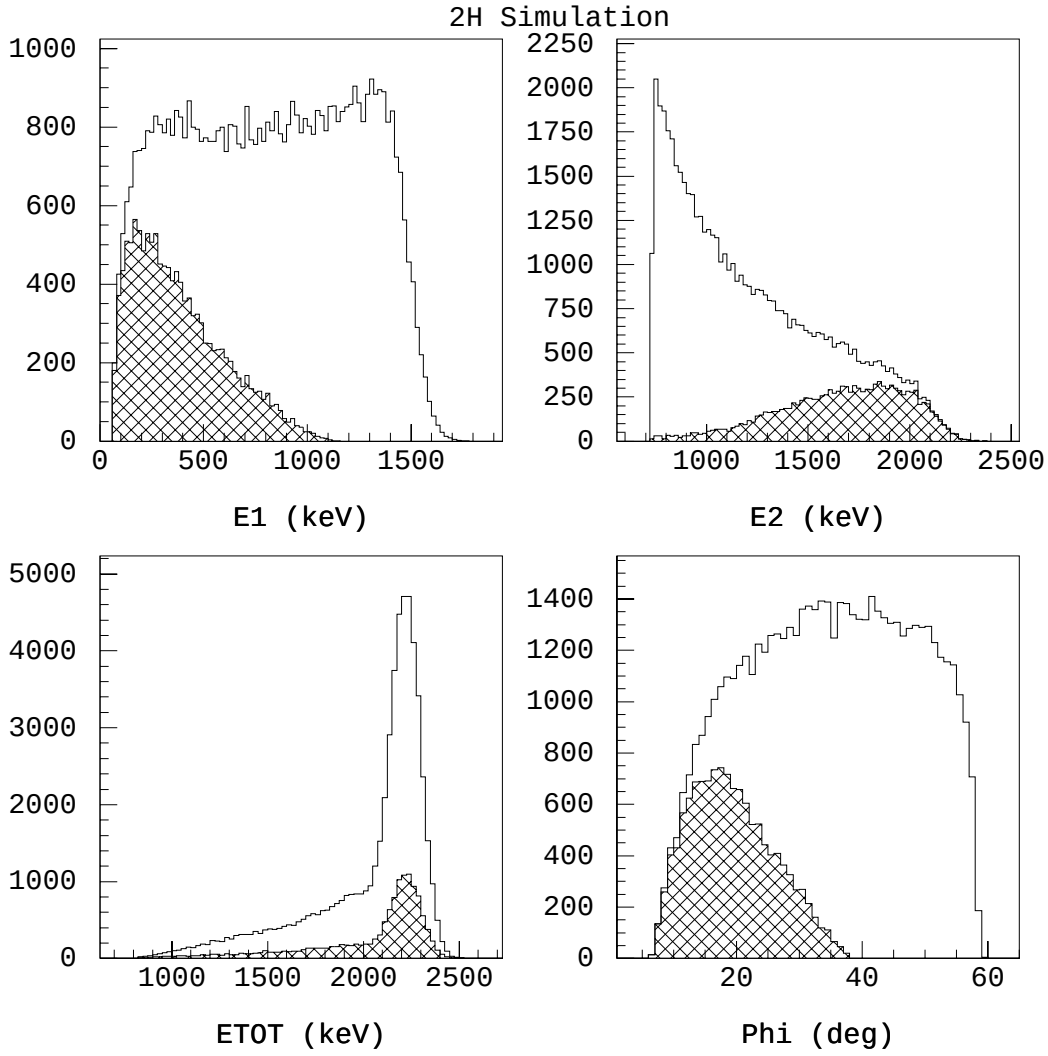

Figure V.C.4 The COMPTEL response to the hydrogen neutron-capture line (2.223 MeV). The line histograms are for standard CDG threshold selections while the solid histogram includes the CDG FoV section.

V.C.5 The ^{40}K Isotope

Production: ^{40}K is a naturally occurring radioactive isotope with an abundance of 0.0117%. The ^{40}K events in COMPTEL dataspace originate from the ^{40}K nuclei present in the glass of the PMTs in D1. ^{40}K nuclei are also present in the PMTs viewing D2, but its contributions are readily excluded by ToF selections. ^{40}K has three decay modes: β^+ (89.3%), EC (10.7%) and β^- (0.001%). The decay through EC has a $\tau_{1/2} = 1.28 \times 10^9$ years and leads to an unstable ^{40}Ar* nucleus with a 98.1% branching ratio. ^{40}Ar* promptly decays (1.1 ps) to

stable ^{40}Ar with the emission of a 1.461 MeV photon. All other decay modes lead to stable nuclei without any photon emission.

$^{40}K^* \rightarrow {}^{40}Ar^* + \beta^- \rightarrow {}^{40}Ar + 1.461\ MeV\ \gamma$

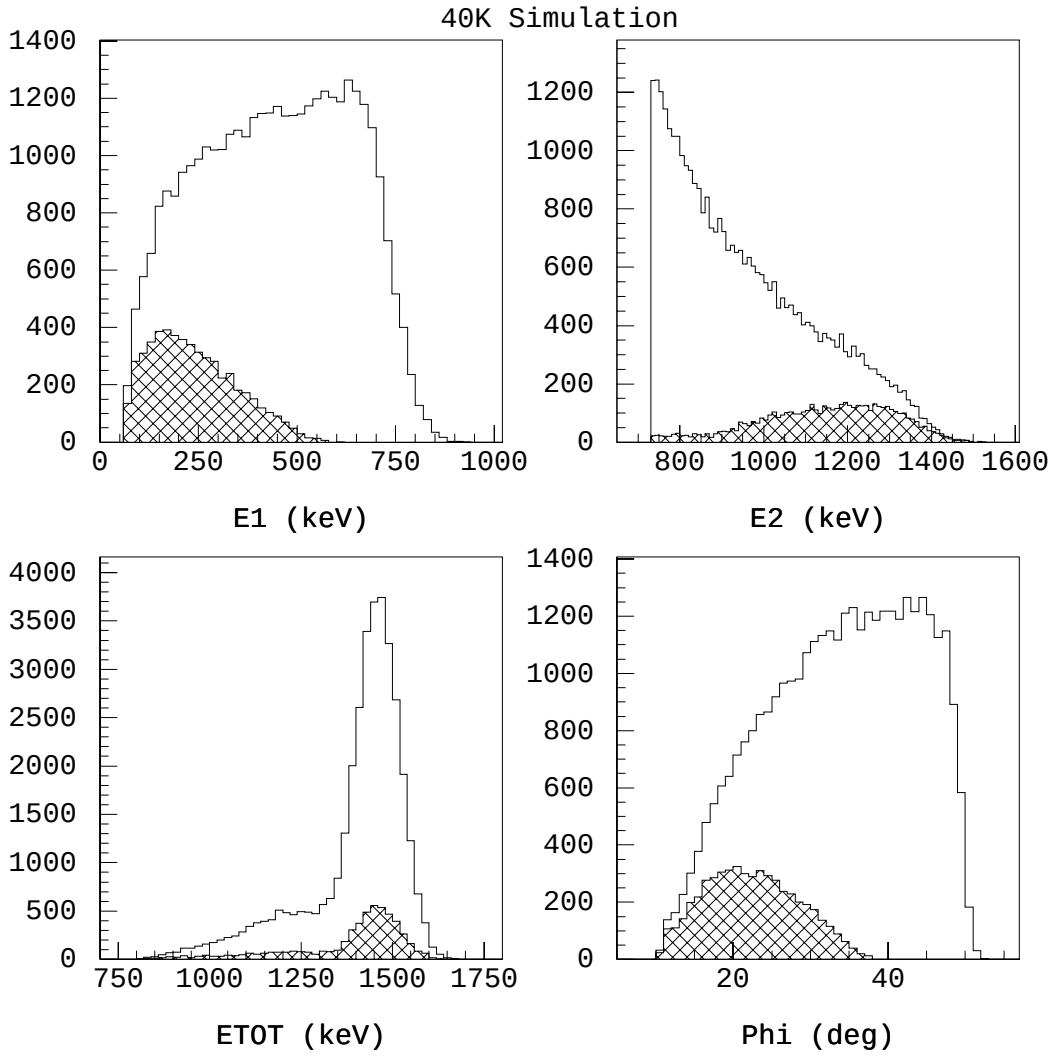

Figure V.C.5 The COMPTEL response to the ^{40}K decay line. The line histograms are for standard CDG threshold selections while the solid histogram includes the CDG FoV section.

Dataspace signature: The COMPTEL response to ^{40}K decay is shown in figure V.C.5. The ^{40}K decay produces a strong long-lived instrumental line at 1.46 MeV in ETOT. Contamination from other isotopes (^{22}Na and ^{24}Na) is nearby. Due to its long half-life the ^{40}K rate is constant (see figure V.C.9) [see also van Dijk 1996; Weidenspointner 1998].

Another possible source of 1.46 MeV photons is the ^{40}K nuclei in the spark chamber of the EGRET instrument. However the position of the spark chamber requires that these photons undergo large angle scatters (ϕ>60˚) to produce type A events. The standard CDG selections on scatter-angle (ϕ<38˚) and D2 energy threshold (>730 keV) eliminates most of these 1.46 MeV events. We attribute all the ^{40}K line to the D1 PMT source.

V.C.6 The ^{28}Al Isotope

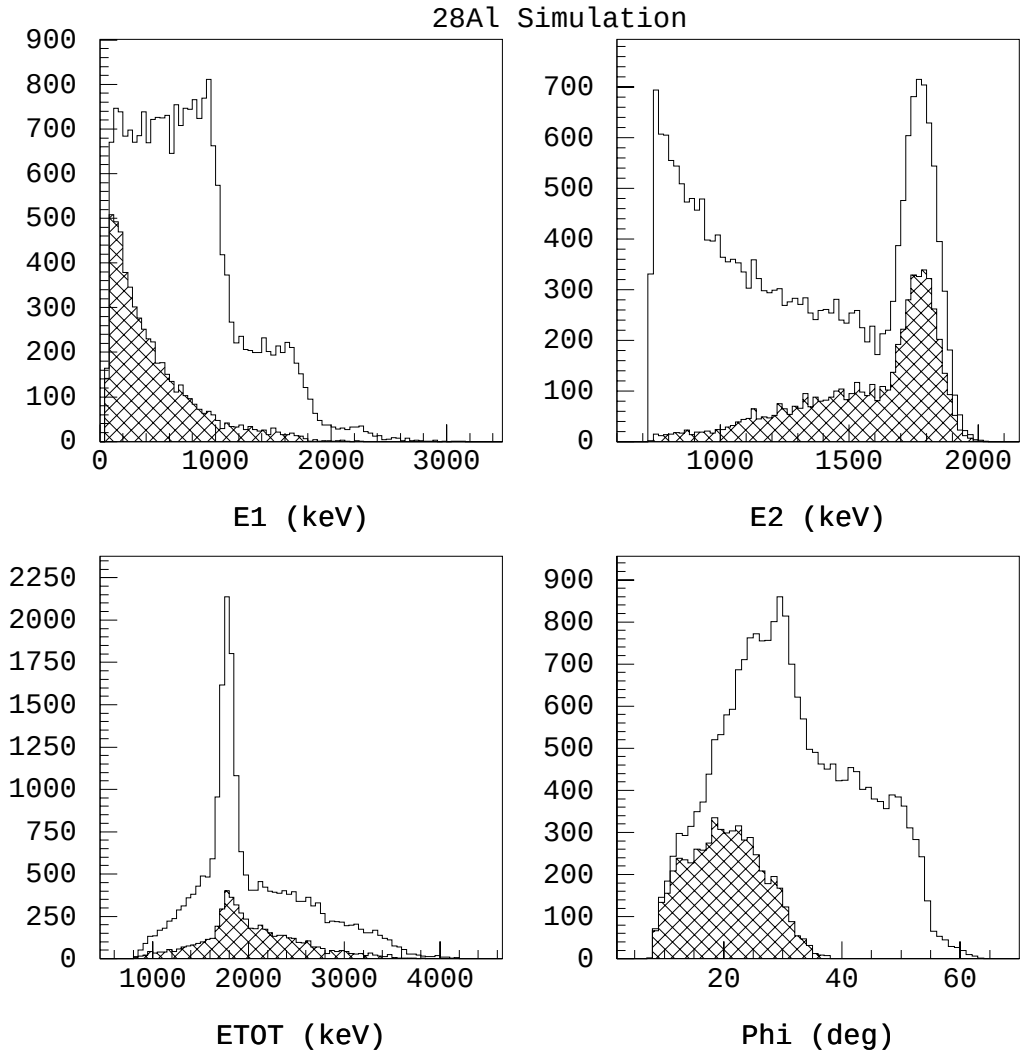

Figure V.C.6 The COMPTEL response to the ^{28}Al decay. The line histograms are for standard CDG threshold selections while the solid histogram includes the CDG FoV section.

The presence of ^{28}Al has not yet been rigorously demonstrated, however, we expect it to exist. Since the ^{28}Al produces a 1.8 MeV photon with $\tau_{1/2}$ ~ 2.24 m, it is a viable candidate to

explain the ~1.8 MeV excess in E2 spectrum. The cross-section for producing ^{28}Al through ^{27}Al(n,γ)^{28}Al is large, σ = 230 mb. The ^{28}Si(n,p)^{28}Al channel can also produce ^{28}Al. ^{28}Si* promptly decays ($\tau_{1/2}$ ~0.5 ps) to the ground state by the emission of a 1.779 MeV photon. The beta particle has a sufficiently high endpoint energy (2.8 MeV) to produce a second photon through the bremsstrahlung process producing type C background events. The required Al and Si nuclei are present in large quantities in the D1 assembly. In addition there are suggestions that the 1.8 MeV line in D2 is of a prompt nature. The COMPTEL response to ^{28}Al decay is shown in figure V.C.6.

$^{27}Al + n \rightarrow {}^{28}Al^*$

$^{28}Al^* \rightarrow {}^{28}Si^* + \beta^- \rightarrow {}^{28}Si + 1.779\ \gamma$

V.C.7 The ^{27}Mg Isotope

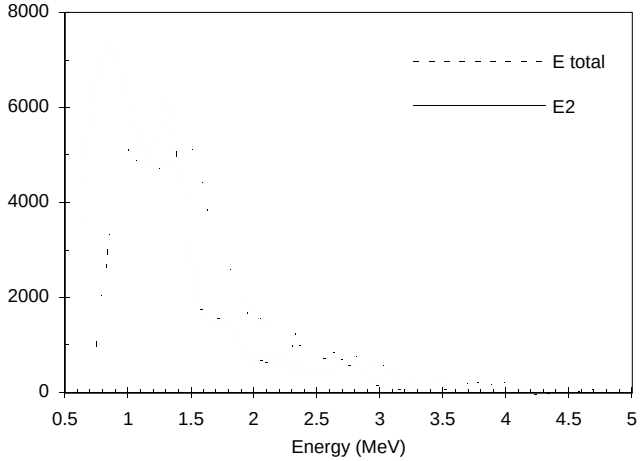

Figure V.C.7 Residual counts in the 30 minutes after SAA passages. Figure reproduced with permission of Morris et al. (1997).

$^{27}Al + n \rightarrow {}^{28}Mg^* + p$

$^{28}Mg^* \rightarrow (72\%)\ {}^{27}Al + 0.844\ \text{MeV}\ \gamma$

$\rightarrow (27.2\%)\ {}^{27}Al + 1.014\ \text{MeV}\ \gamma$

$\rightarrow (0.8\%)\ {}^{27}Al + 1.014\ \text{MeV}\ \gamma + 0.171\ \text{MeV}\ \gamma$

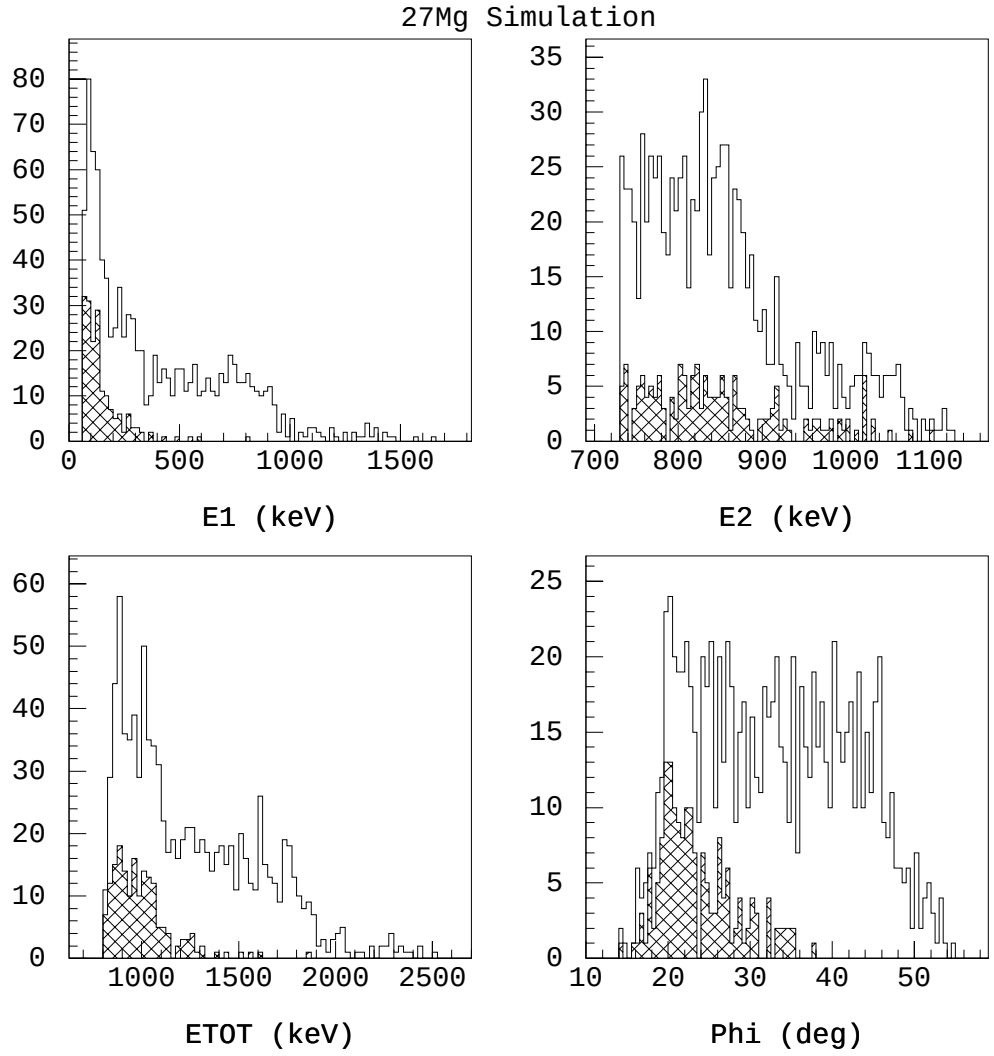

Figure V.C.8 The COMPTEL response to the ^{27}Mg decay. The line histograms are for standard CDG threshold selections while the solid histogram includes the CDG FoV section.

Although the cross-section for the production of ^{27}Mg via ^{27}Al(n,p)^{27}Mg is comparable to the ^{27}Al(n,α)^{24}Na channel its presence in the data is not clear (see figures V.C.7, 10 and 11). The first indications of ^{27}Mg appeared during a search for the ^{56}Co lines (847 and 1014 keV) from supernovae (Morris et al. 1997). The relative short half-life of ^{27}Mg (9.5 m) suggests that its contribution should be pronounced immediately after an SAA passage. The E2 spectra taken 30 minutes after an SAA passage shows a peak near the 844 keV line expected from ^{27}Mg (figure V.C.7) with a high energy shoulder extending up to ~1.5 MeV. The corresponding ETOT spectrum also shows an excess below 2 MeV. These excesses are

consistent with ^{27}Mg decay. The ^{27}Mg isotope is a single-photon beta emitter with a end-point energy at 1.6 MeV (41%) or 1.75 MeV (58%). The COMPTEL response to ^{27}Mg decay is shown in figure V.C.8.

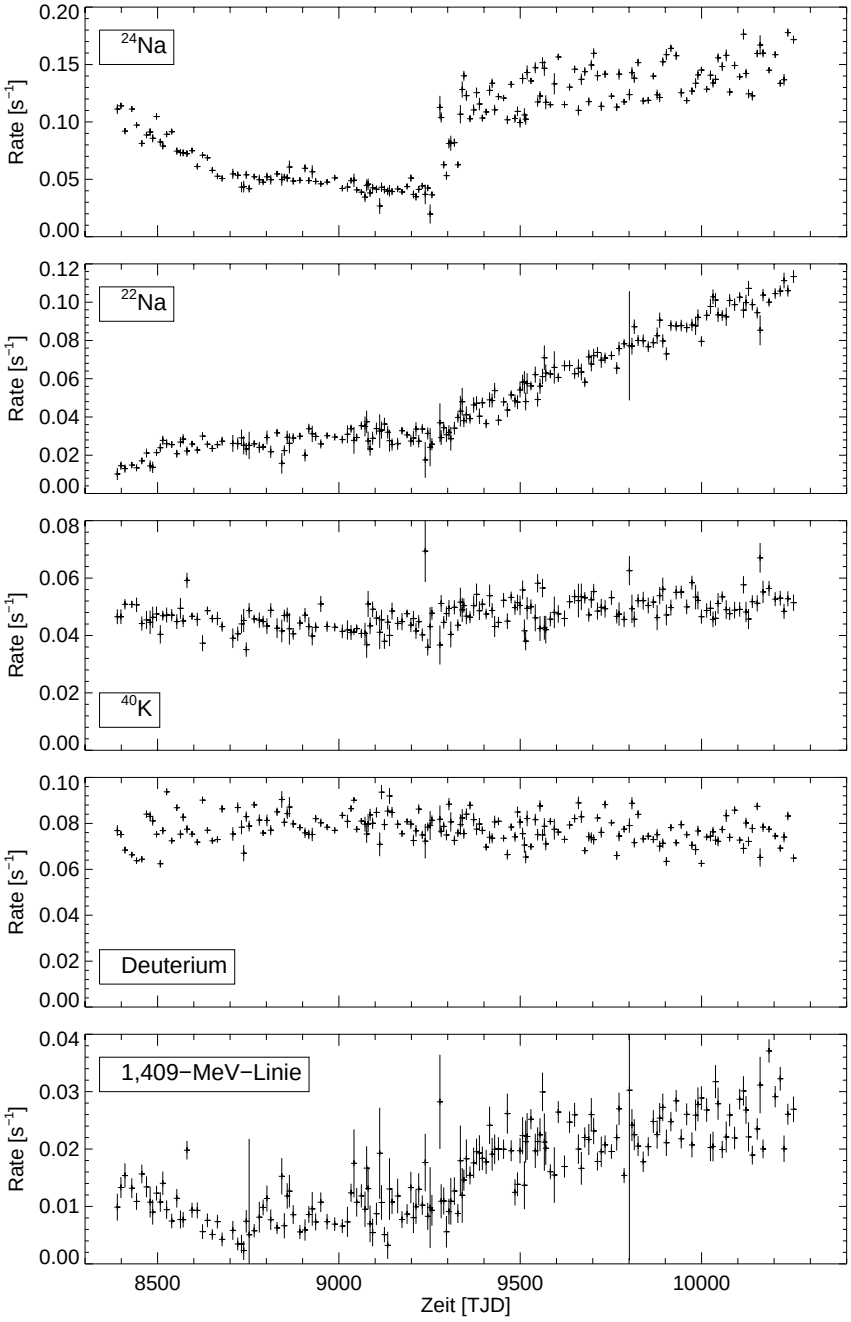

Figure V.C.9 The average rate for the ^{24}Na, ^{22}Na, ^{40}K isotopes, the 2.2 MeV line in ETOT and the 1.41 MeV in E2 spanning the first five years of COMPTEL operation. Figure reproduced with permission of U. Oberlack (1998).

V.C.8 Dataspace and CDG Simulation Characteristics

The average rate for the ^{24}Na, ^{22}Na, ^{40}K isotopes, the 2.2 MeV line in ETOT and the 1.41 MeV in E2 spanning the first five years of COMPTEL operation is shown in figure V.C.9. To better understand the complicated energy spectrum, the E2 and ETOT spectra are plotted for a high rigidity (R>10 GV) selection, figures V.C.10 and V.C.11 respectively. The high rigidity selection minimizes the prompt background contributions to more clearly see the line/emission structure. The spectra are also plotted for different ϕ selections. The ϕ selections have a significant impact on the resulting energy spectrum thereby demonstrating its power to enhance or suppress background components. This ability of ϕ selections are fully exploited in the CDG analysis. The specific ϕ selections used in the CDG analysis are described later. We note these features:

(1) The ^{24}Na component decreases with increasing ϕ selection. This seen as the decrease in the 2.754 MeV line in E2 (and the 2.7–4.2 structure in ETOT) with increasing ϕ value. Such a behavior is expected from simulations.

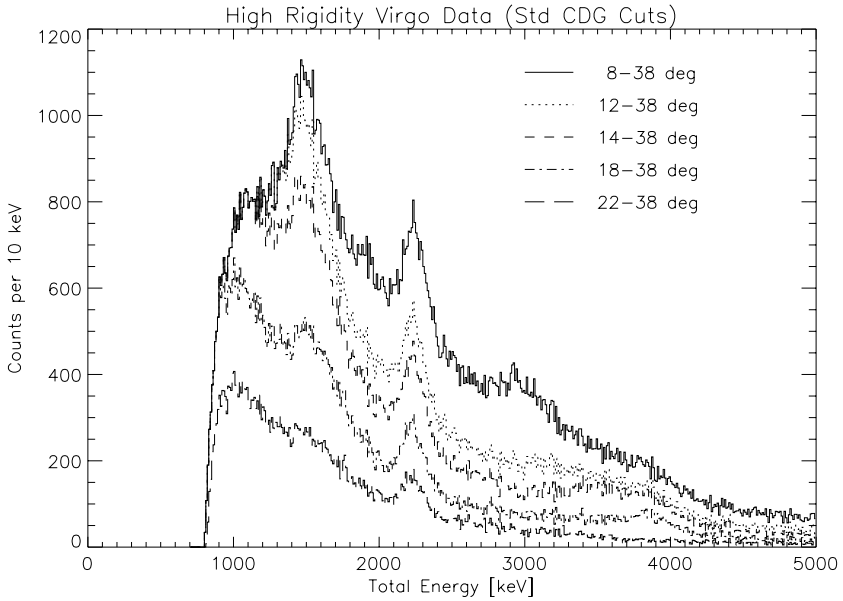

Figure V.C.10 The ETOT spectra for high rigidity (>10 GV) P3V data showing the line/emission structure below ~4.2 MeV. The contributions from different ϕ ranges are also shown.

(2) The 2.2 MeV line, although decreasing is present at all ϕ values. Similarly the ^{28}Al line is decreasing with high ϕ. However the ^{28}Al decreases faster than the 2.2 decreases in the

data (the Al 1.8 MeV line in E2 has almost vanished for ϕ 22–38˚ but the 2.2 MeV gaussian can still be identified in ETOT). Such a behavior is expected from simulations.

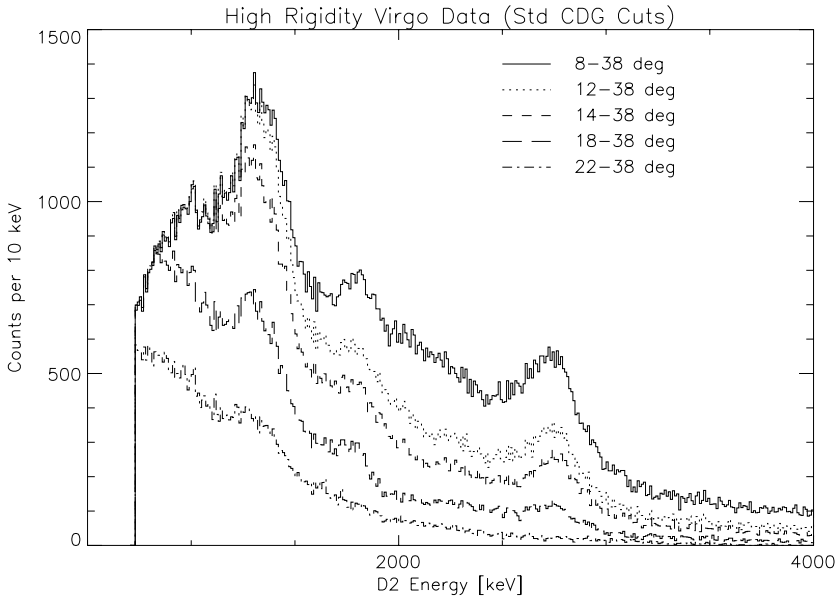

Figure V.C.11 The E2 spectra for high rigidity (>10 GV) P3V data showing the line/emission structure below ~4.2 MeV. The contributions from different ϕ ranges are also shown.

(3) The line near 1.3 MeV in E2 is a blend of different lines since different parts in the 1.3 MeV peak are affected differently by the decrease in ϕ. This asymmetry is also seen in the ETOT line around 1.5 MeV. This behavior is not unexpected since these two peaks include ^{40}K, ^{22}Na and the ^{24}Na components.

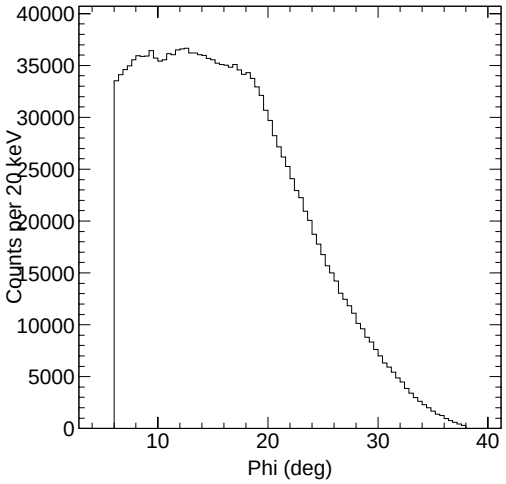

Figure V.C.12 The measured ϕ spectrum using P2345V data.

(4) The measured ϕ spectrum (figure V.C.12) is quite different from that of CDG simulations (figure V.C.13), especially below 20˚ where the data show excess counts compared to simulations. This suggests that most of the events at low ϕ values are background events.

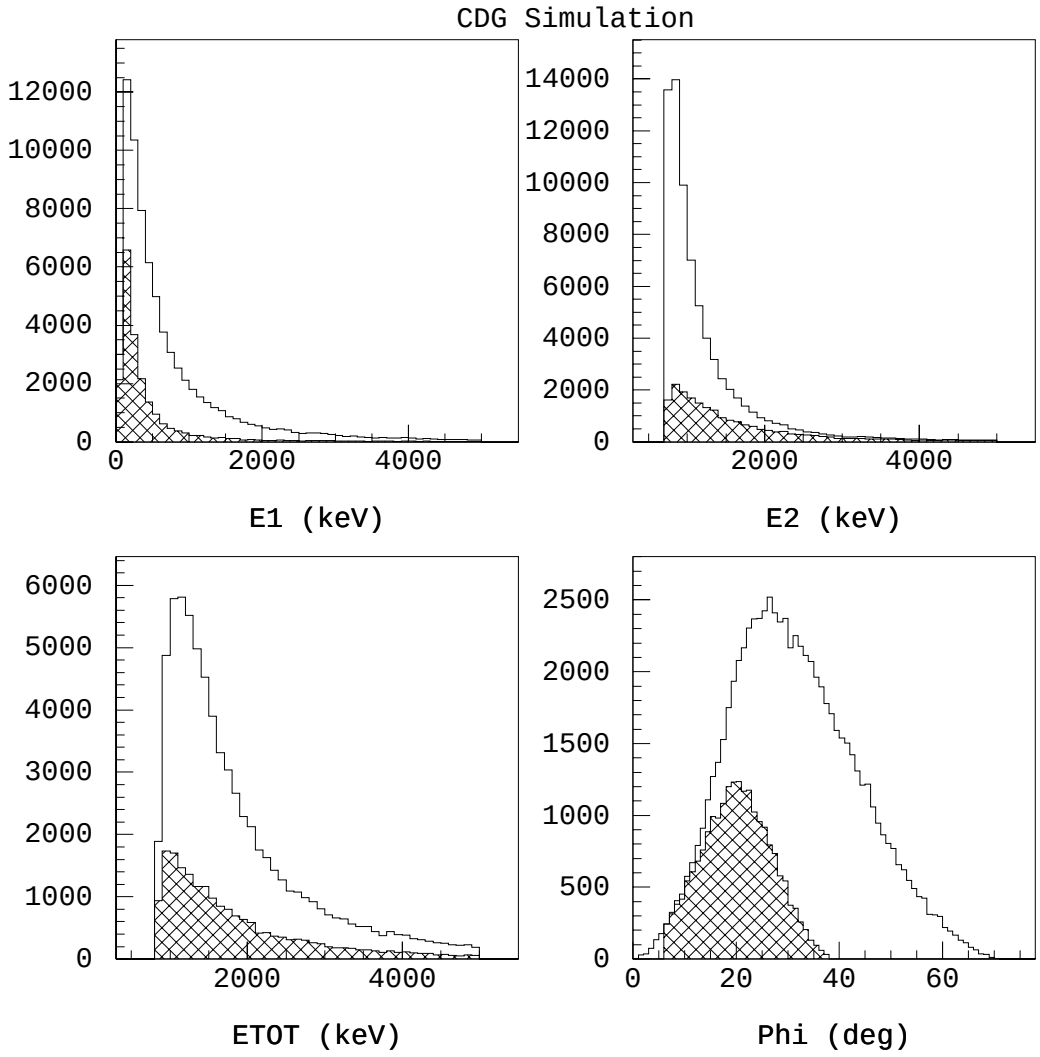

Figure V.C.13 The COMPTEL response to CDG simulations. The line histograms are for standard CDG threshold selections while the solid histogram includes the CDG FoV section.

V.C.9 The E2 Spectrum

The E2 spectrum below 4.2 MeV consists of line emission superimposed over a smooth continuum. The data used here are the veto-integrated P2345 data with standard-CDG data selections. The E2 spectrum is plotted in figure V.C.14 for a 110–130 ToF cut that selects on

the ToF peak region. The exponential function used to describe the continuum is also plotted. It has the form: $A \times (1 - B \times \exp(x-C)) \times \exp(D \times x)$, where x is the E2 energy and A, B, C and D are constant determined from the fit.

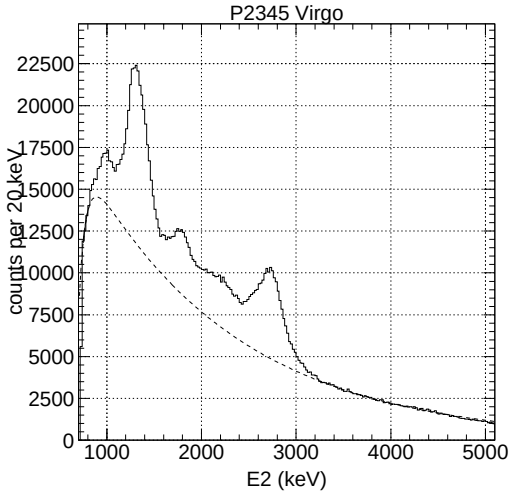

Figure V.C.14 The P2345V E2 spectrum together with exponential-continuum function.

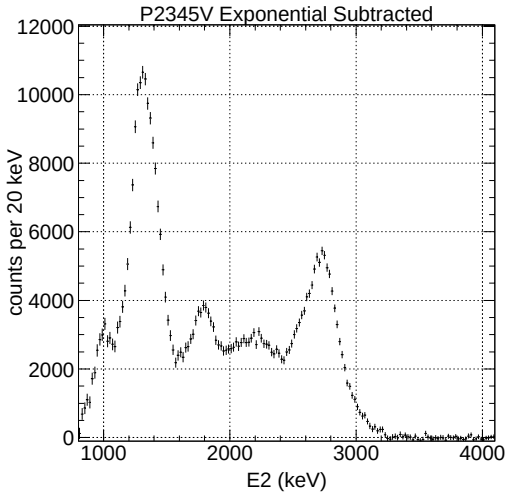

Figure V.C.15 The line emission in the P2345V E2 spectrum.

A similar function has been successfully used in other COMPTEL line analysis and has adequately modeled the continuum background. The spectrum is fit in two regions: 3220–4280 keV to determine the decreasing exponential parameters (A and D) and 740–800 keV to determine the threshold roll-over parameters (B and C). The residual after subtracting the

exponential is assumed to be entirely due to line emission originating within the instrument (figure V.C.15).

We determine the ^{24}Na intensity by fitting the 2.754 MeV line region (2500–3400 keV) using a simulated ^{24}Na decay template. Detailed examination of the spectrum near the 2.754 MeV peak reveals the existence of two additional lines located at 2.93 and 2.58 MeV. Many checks have been performed to ensure that these lines are not a result of an incorrect (e.g. a narrow) ^{24}Na response. These lines differ from the ^{24}Na events in two ways: they have different dependencies on E1 selections (see discussion on the residuals below) and their intensities vary differently with the veto rate (see section V.E). We will see that a judicious data selection minimizes their impact in the CDG analysis (see section VI.D). Both lines are modeled as gaussians in the E2 spectrum. The resulting fits for these components are plotted in figure V.C.16.

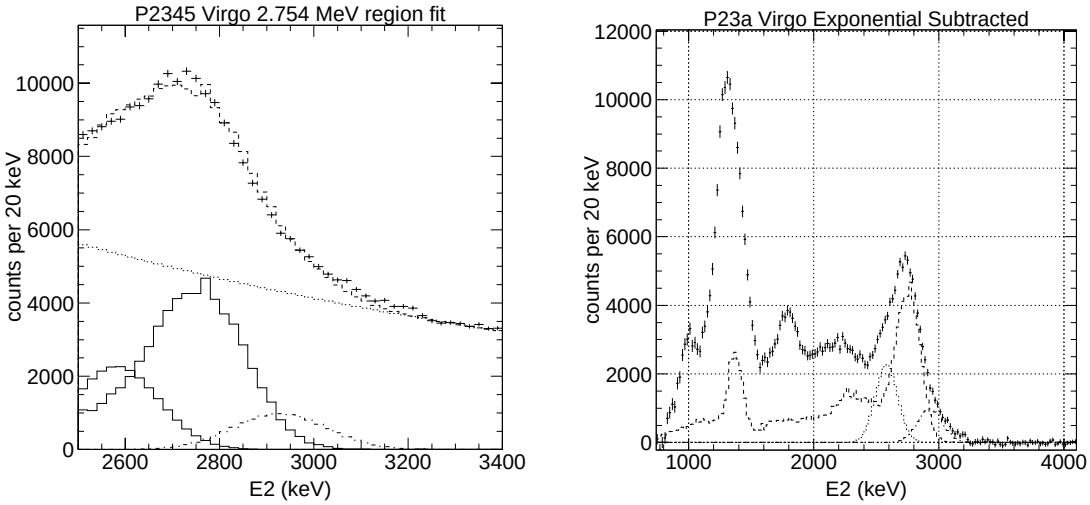

Figure V.C.16 Fit of the 2.754 MeV line region in the E2 spectrum.

The deuterium contribution is computed independently by fitting the 2.2 MeV line photopeak with the appropriate 2.2 MeV template in the ETOT spectrum (figure V.C.17) and through simulations computing the contribution to the E2 spectrum. The fit to the 1.78 MeV line from ^{28}Al is performed over a narrow energy region (1600–1900 keV) with the ^{28}Al template superimposed on a flat continuum. The 2.2 MeV response is flat in this range and is used for a baseline. The flat continuum, in part, accounts for possible Compton tail contributions from the unidentified lines at 2.58 and 2.93 MeV. We expect the Compton tails

of the 2.58 and 2.93 MeV lines to be flat because the Compton tail for the 2.754 MeV line is flat in this region.

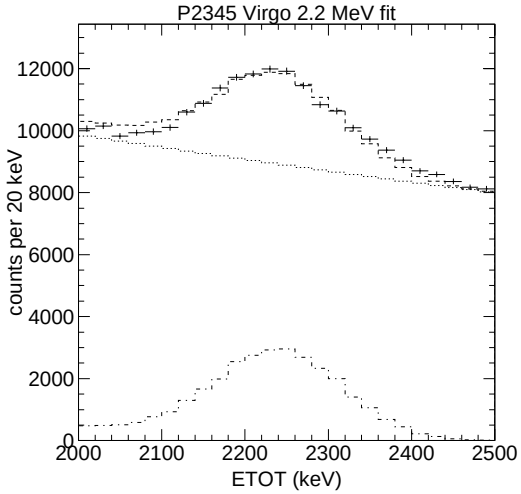

Figure V.C.17 Fit of the 2.2 MeV line photopeak in the ETOT spectrum.

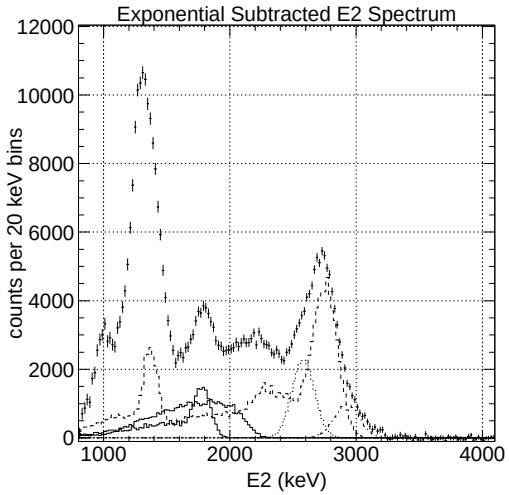

Figure V.C.18 Fit of the 1.8 MeV line region in E2 spectrum.

The next step is to fit the 1.2–1.4 MeV region that contains contributions from ^{40}K and ^{22}Na and a 1.4 MeV photopeak (another unidentified line). Note that the 1.368 MeV line from ^{24}Na has already been subtracted using the complete ^{24}Na template. A detailed examination of the 1.3 MeV region reveals the existence of a 1.41 MeV line feature. As with the 2.6 and 3.0 MeV lines we have checked to ensure it is not a result of an incorrect ^{22}Na response. The photopeaks of the 1.41 and 1.275 MeV of ^{22}Na are separated by 135 keV or

~3 resolution widths. The presence of the 1.4 MeV feature has also been noted in the context of ^{40}K (van Dijk 1996) and ^{22}Na (Oberlack 1998) investigations. The existence of the 1.4 MeV line is well established, however its origin is still unknown. This 1.4 MeV line appears to be long-lived in nature and is discussed in more detail in the following section on residuals. I have modeled this 1.4 MeV feature as a simple gaussian with no tail.

We know the ^{40}K mass in the PMTs and its response is determined from independent measurements and simulations. Therefore, the ^{40}K intensity is determined with no free parameters. If ε is the efficiency of detecting ^{40}K photons in some energy range in E2 for a set of data selections, then the number of ^{40}K counts is

$$^{40}\text{K counts in data} = \varepsilon \times f \times (M_k/m_k) \times N_A \times (\Delta t/\tau_{1/2})$$

where, f is the ^{40}K abundance ratio (0.0117%), M_k is the total K mass (87.36 gm), m_k is the atomic weight, N_A is Avogardo's number, Δt is the total time integration and $\tau_{1/2}$ is the ^{40}K half-life (1.3×10^9 years). The expected counts depends on only the total exposure Δt. Figure V.C.19 shows the result of fitting all the identified components. Any ^{27}Mg component has not been subtracted because there is no clear signature of it in the E2 spectrum.

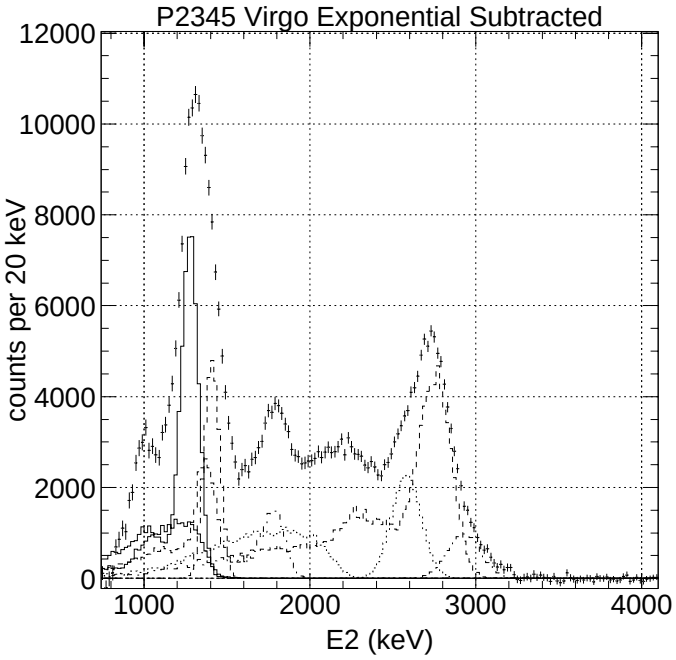

Figure V.C.19 Fit of the E2 spectrum with all identified line components.

V.C.10 The Unidentified Spectral Features

The three unidentified lines at 1.41, 2.58 and 2.93 MeV together with the remaining residuals (the broad excess in the 2000-2400 keV region) are plotted in figure V.C.20. This represents the fraction of the E2 spectrum that is not accounted for by the presently identified isotopes. The Compton tail from higher energy lines is not likely to explain all of the unexplained emission between 1600 to 2500 keV. There is most likely an addition component in the 2000–2400 keV region, it lacks a clear gaussian structure but may well be composed of a blend of lines.

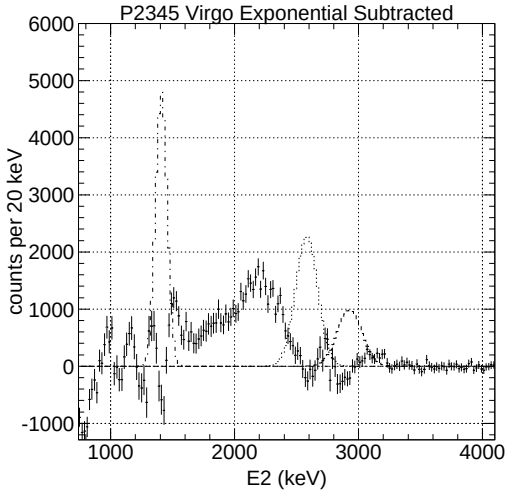

Figure V.C.20 The four residual features in the E2 spectrum of unidentified origin.

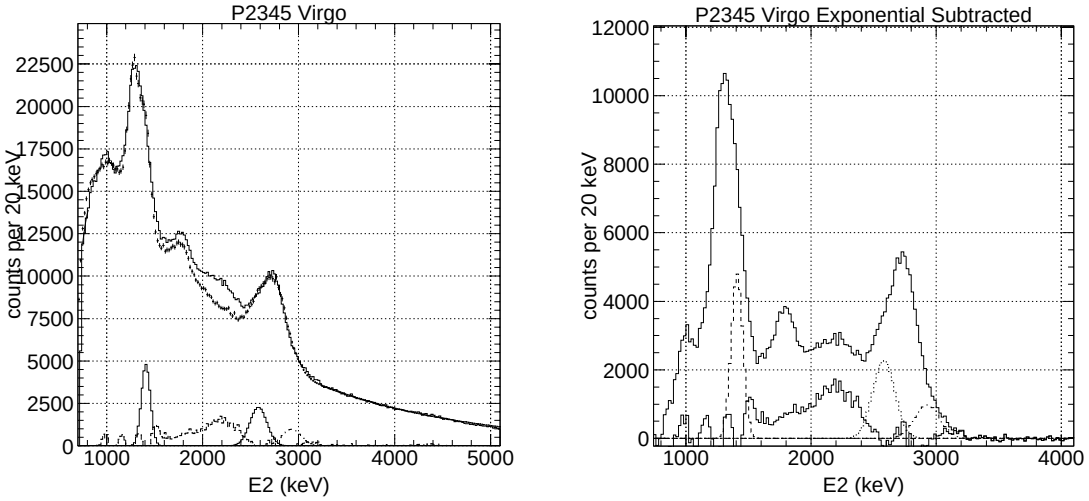

Figure V.C.21 The residual features in the E2 spectrum compared to the total counts.

Nevertheless, we are able to account for a large fraction of the line emission with the identified isotope templates. The residuals underneath the line fits are 10–20% of the peak counts. Considering the entire E2 spectrum (figure V.C.21), the fit is reasonably successful in accounting for most of the events in the E2 spectrum.

The 2.58 and 2.94 MeV lines:

By comparing the ETOT and E2 spectra for step-wise ϕ selections (figures V.C.10–11), we see that a ϕ 22–38˚ selection is effective in suppressing the line contributions. The disappearance of the 2.754 MeV photopeak region including the 2.6 and 2.9 MeV peaks in E2 by the ϕ 22–38˚ selection is clearly seen in figure V.C.22 where the E2 spectrum is shown for ϕ>22˚ and ϕ<22˚ together with the total E2 spectrum. Figure V.C.23 shows the corresponding spectra in ETOT space.

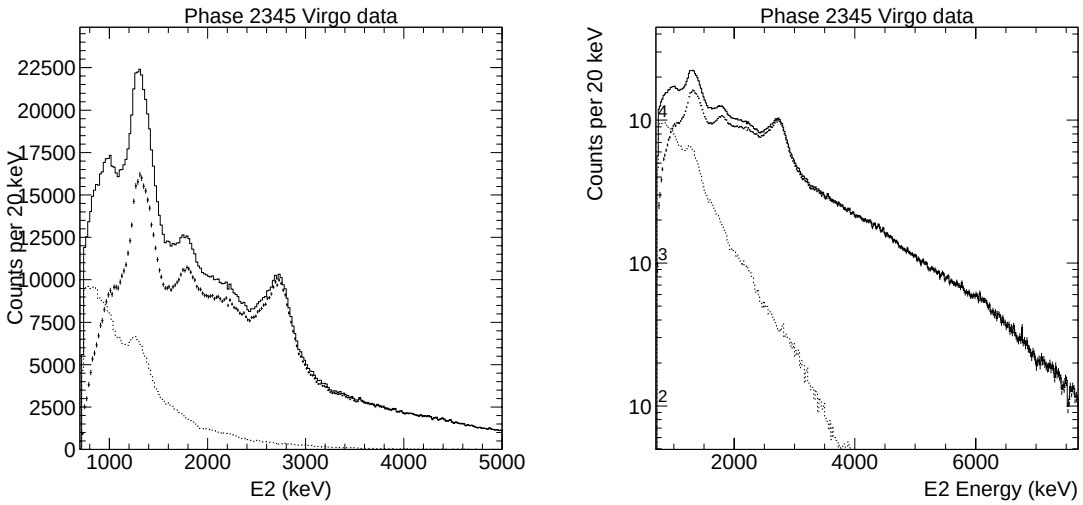

(a) (b)

Figure V.C.22 The P2345V data E2 spectrum (solid line) showing the contributions from ϕ>22˚ (+) and ϕ<22˚ events (dotted line) in (a) linear y-scale (b) logarithmic y-scale.

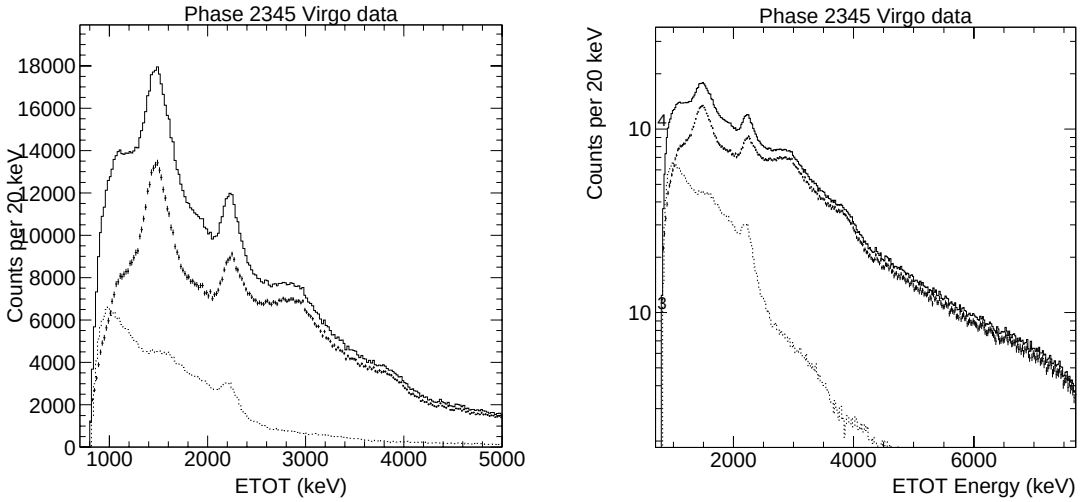

Figure V.C.23 The P2345V data ETOT spectrum (solid line) showing the contributions from ϕ>22˚ (+) and ϕ<22˚ events (dotted line) in (a) linear y-scale (b) logarithmic y-scale.

Figure V.C.24 shows the distribution of ETOT 2.7–4.2 MeV events to the E2 spectrum. The shaded region are those ETOT events with ϕ>22˚. Clearly, the 2.94 and 2.58 MeV lines in E2 are present in the ETOT 2.7–4.2 MeV bin for the open ϕ selections. But the ^{24}Na component together with the 2.6 and 2.9 MeV lines are substantially suppressed with the ϕ>22˚ selection. The impact of the ϕ>22˚ on the ^{24}Na isotope is discussed in more detail in section VI.D.

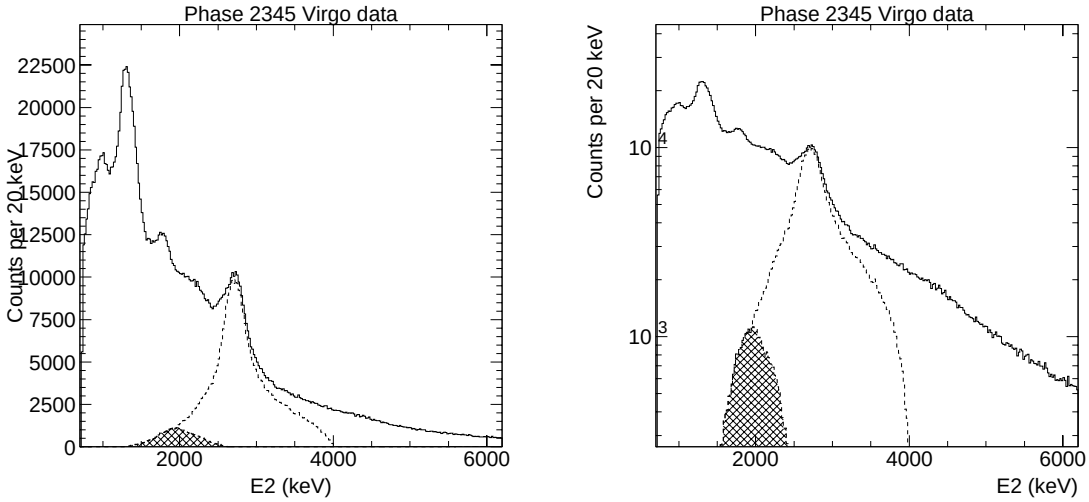

Figure V.C.24 The contribution of the ETOT 2.7–4.2 MeV events (dashed line) to the total E2 spectrum (solid line). The shaded region are those ETOT events with ϕ>22˚.

The 1.41 MeV line:

The E2 spectrum resulting from a narrow cut of 270–350 keV in E1, to select on the Compton edge of a 511 keV photon in E1, is plotted in figure V.C.25. Such a selection enhances those structures associated with a β^+ decays. As expected, the ^{22}Na peak is enhanced relative to the underlying continuum but the 1.4 MeV peak is also present. Both ^{22}Na and the 1.4 MeV counts reduce by the same factor (~3) for the E1: 270–350 keV cut. This indicates that the 1.4 MeV feature is also associated with a β^+ decay. The association with a 511 keV line in E1 means that all the 1.4 MeV related counts will be present from 1300–1700 keV in ETOT. This is shown graphically in figure V.C.26 where the contribution of the ETOT 1.2–1.8 MeV events to the E2 spectrum are plotted. The shaded region are those ETOT 1.2–1.8 MeV events with ϕ>22˚.

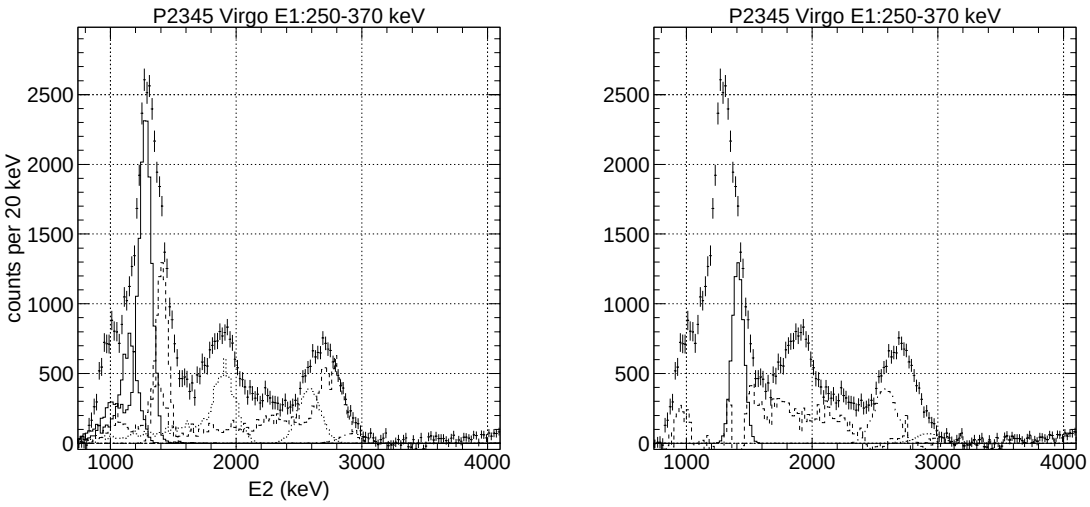

Figure V.C.25 The fit for the E2 spectrum with E1:270–350 keV and the residuals.

The ^{22}Na events are not suppressed by the ϕ>22˚ selection, as seen from the ϕ spectrum of ^{22}Na response simulations (see figures V.C.3 and 26). Similarly, we do not expect the 1.4 MeV events to be suppressed by the ϕ>22˚ selection. But we expect the relative strengths of the ^{22}Na and the 1.4 MeV line to be similar for the same data selections since they have similar D1 and D2 energy deposits. We use this to estimate the contribution of the 1.4 MeV line to the 0.8-1.2 MeV bin in ETOT.

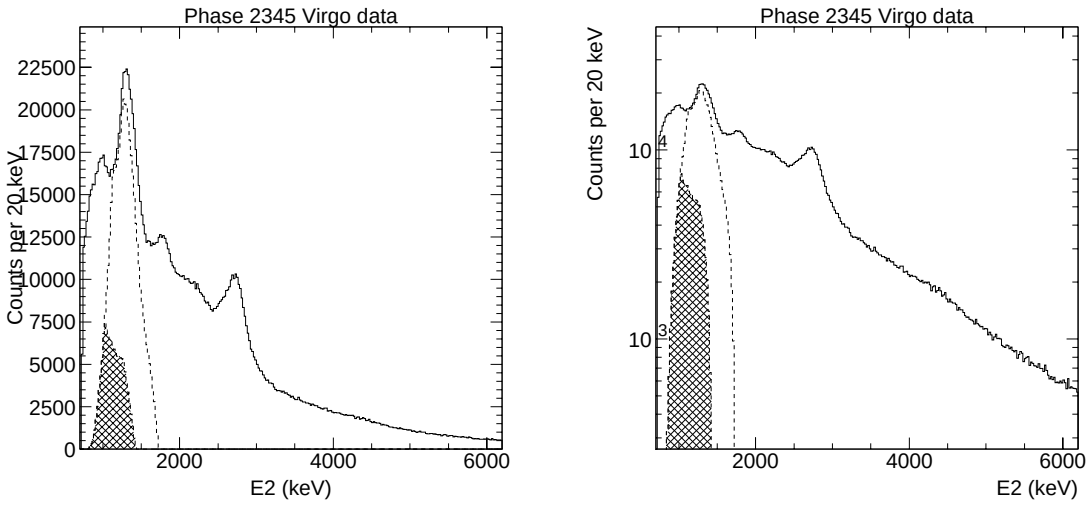

Figure V.C.26 The contribution of the ETOT 1.2–1.8 MeV events (dashed line) to the E2 spectrum (solid line). The shaded region are those ETOT events with ϕ>22˚.

As discussed below (section V.E) the 1.4 MeV and ^{22}Na feature have similar VGCs supporting the conclusion that the 1.4 MeV feature is a long-lived component. Although the 1.4 MeV rate is noisier with larger uncertainties, its evolution with time is similar to that of the ^{22}Na line (see figure V.C.9).

The 2000–2400 keV excess:

The other point to note is the suppression of the 2000–2400 keV excess with the E1 270–350 keV cut. If the associated second photon with the excess is of lower energy then the entire 2000–2400 keV feature must be contained within the 1.8 to 2.7 MeV bin in ETOT. The distribution of ETOT 1.8-2.7 events in the E2 spectrum (figure V.C.27) shows that it contains most E2 events below ~2500 keV, making the case for the 2000–2400 keV excess to contribute to the 1.8–2.7 MeV bin. However the picture changes with a ϕ>22˚ selection.

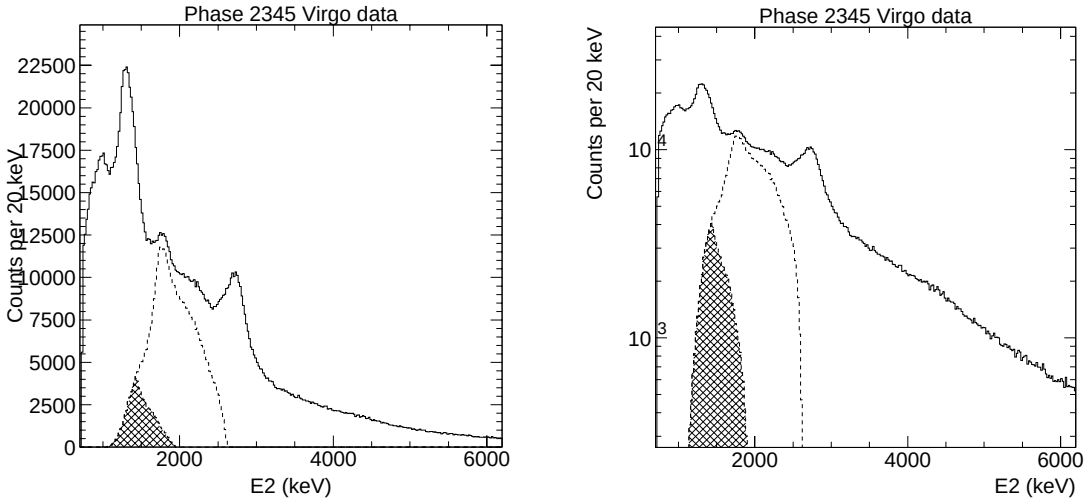

Figure V.C.27 The contribution of the ETOT 1.8–2.7 MeV events (dashed line) to the E2 spectrum (solid line). The shaded region are those ETOT events with ϕ>22˚.

Figure V.C.27 shows the contribution of the ETOT 1.2–1.8 MeV events to the E2 spectrum. The shaded region are those ETOT 1.2–1.8 MeV events with ϕ>22˚. The ϕ>22˚ selection does not include events from the 2000–2400 keV region. Hence the ϕ>22˚ selection is effective at minimizing (even eliminating) the contribution from the 2000–2400 keV excess in the E2 spectrum. This fact is used in the 1.8–2.7 MeV CDG analysis. In addition the 2000-2400 keV excess appears to be prompt in nature (see section V.E), and will be subtracted in the VGC extrapolation. To summarize, the 2000–2400 keV excess does not contribute to the ETOT 1.8–2.7 MeV bin in the CDG analysis.

Aluminum is by far the most abundant element in COMPTEL (and the spacecraft) and all presently identified isotopes are produced from activation in Al. The other elements which have significant mass that may also lead to radioactive isotopes in COMPTEL include Cu, Si and O. Although it is tempting to associate the residuals to isotopes of these elements, a preliminary search for cascade lines in the range of these atomic masses has provided no obvious clues. This is an area of further study. As the atomic number (or mass) gets higher, as with Cu, there are many more potential decay chains that must be searched.

V.D. The Veto Rate Measurement

The vertical cutoff rigidity is a physical parameter that describes the local cosmic-ray intensity and shows a strong anti-correlation (figure V.D.1) with the instantaneous veto-rate. The modulation of the four veto-rates is shown for a typical day (TJD 9725) in figure V.D.2. The 4 veto-domes exhibit similar behavior. The veto2 and veto4 domes are the same size and have similar range of rates, likewise veto2 and veto4 domes are about the same size and have a similar range of rates.

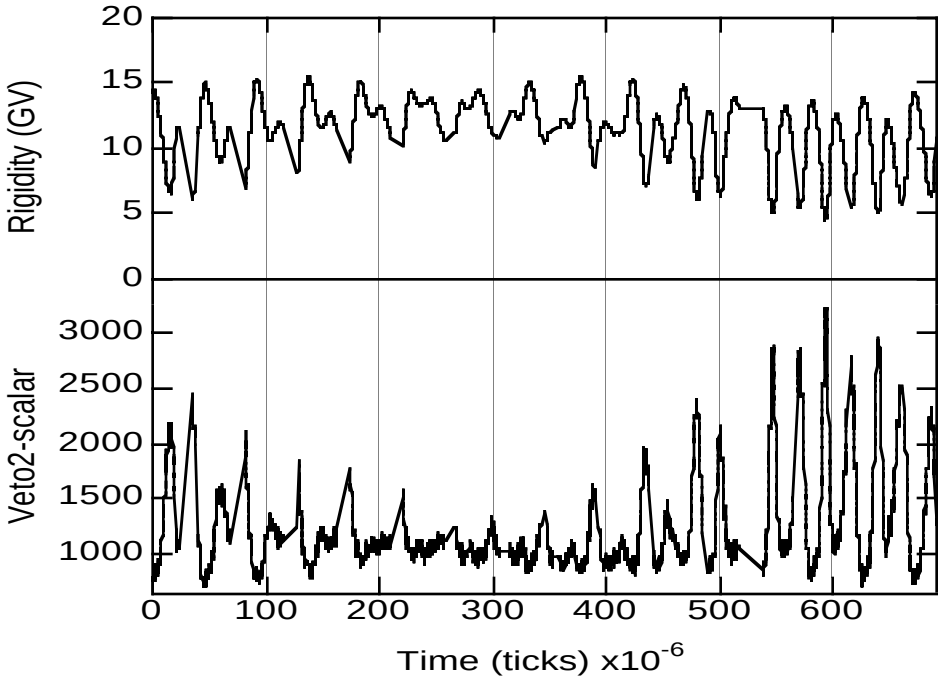

Figure V.D.1 The vertical cutoff-rigidity and the instantaneous veto-rate showing a strong anti-correlation (for TJD 9725).

The veto-rate frequency distribution for each of the domes are shown in figure V.D.4. Note that the general shape of the frequency distributions are similar. However the exposure is not uniform and conforms to the distribution of cutoff rigidities. COMPTEL traverses a cutoff rigidity range of 4.5 to 15.5 GV but spends most of its time between 11–13 GV (figure V.D.3b).

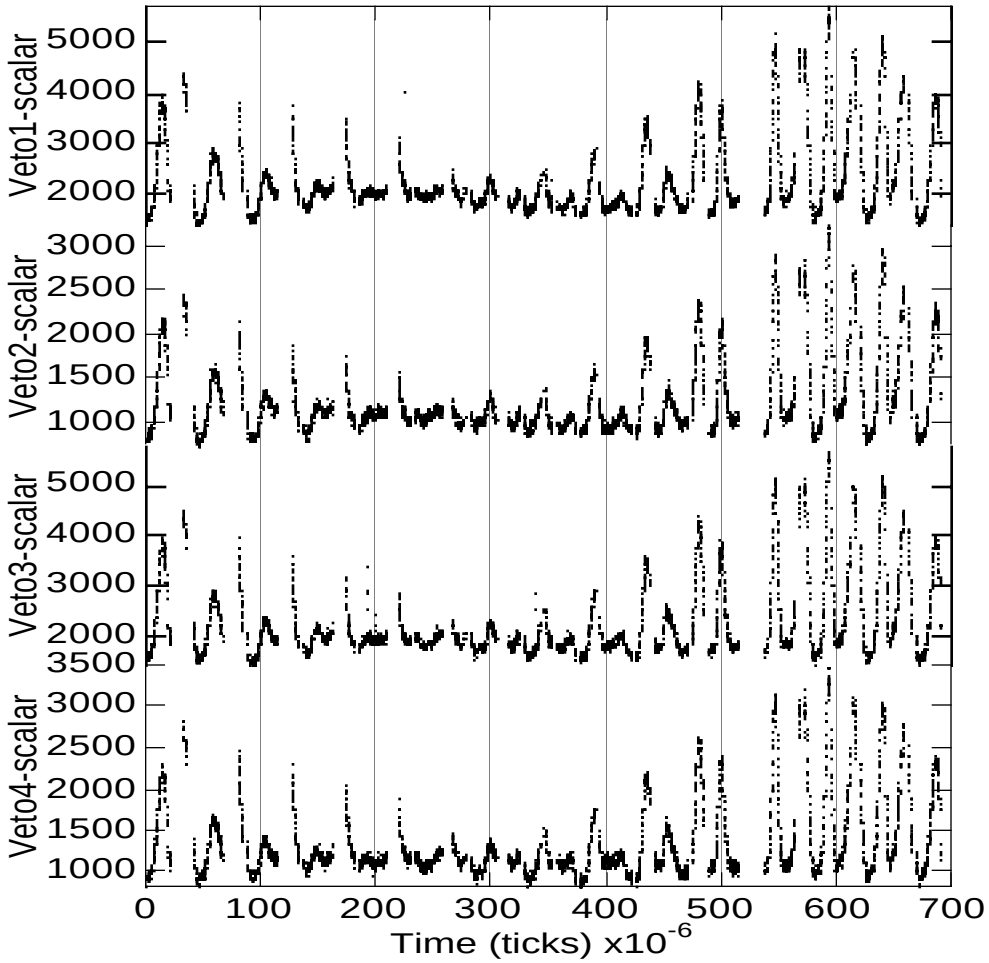

Figure V.D.2 The typical behavior of the four veto scalers showing a similar modulation with time for a typical day (TJD 9725).

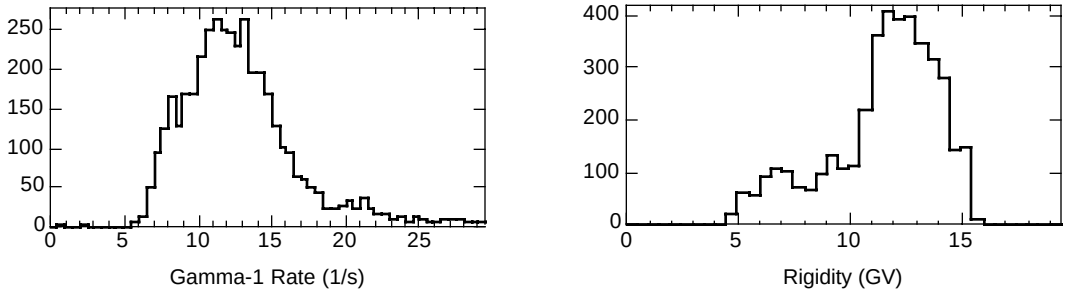

(a) (b)

Figure V.D.3 The frequency distribution of the (a) Gamma-1 rates and (b) the cutoff-rigidity (for TJD 9725).

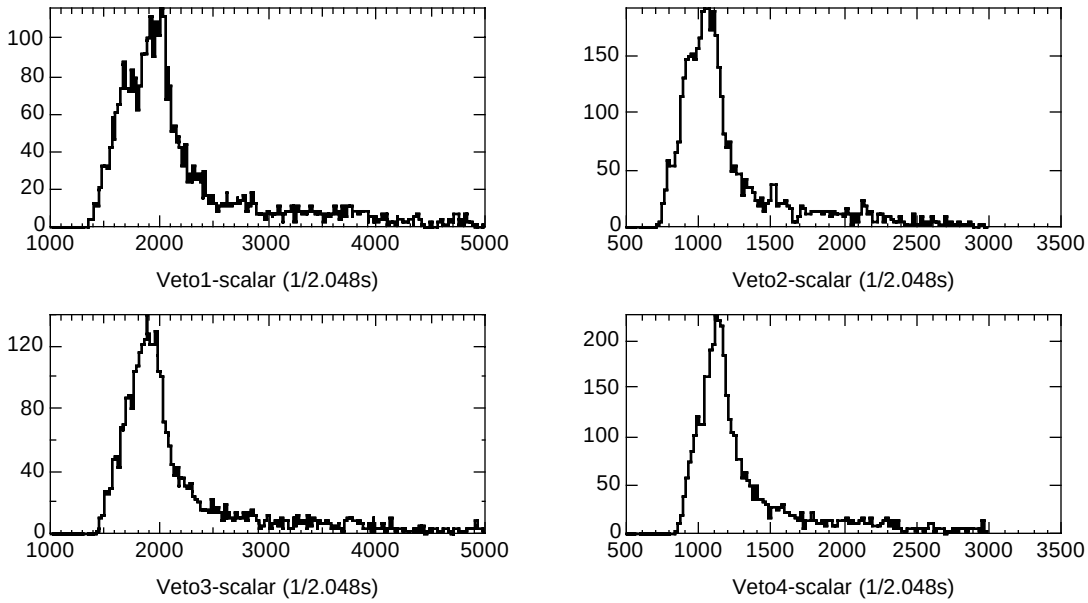

Figure V.D.4 The frequency distribution of the four veto rates (for TJD 9725).

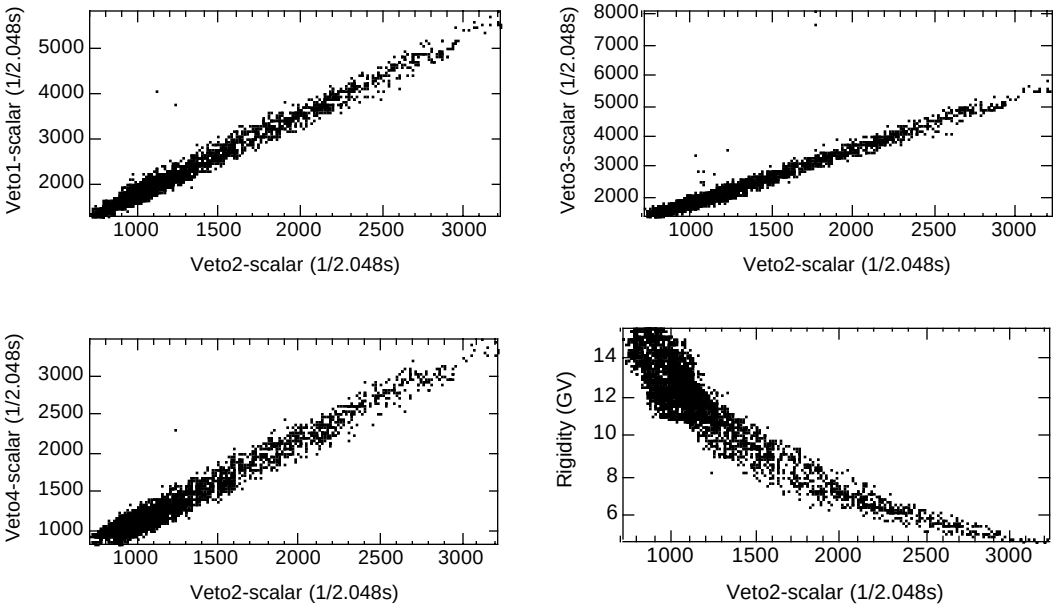

Figure V.D.5 The scatter-plot of veto2-rate with the other veto domes rates and the cutoff-rigidity (for TJD 9725). The strong correlation between the four independent veto-rate measurements is clearly seen.

A scatter-plot between any two of the veto domes (figure V.D.5) shows that the four independent veto-rate measurements are strongly correlated. The linear correlation coefficients between the veto1, veto3 and veto4 rates with the veto2-rate are 0.99, 0.98 and 0.99, respectively. A least-squares analysis on the veto-rate scatter plots gives a 1σ error on

the fractional residuals of ~5% of the measured rates. The 5% error on the rates is greater than the square-root Poisson error. For example, at ~1000 (triggers/2.048s), the predicted Poisson error is 33 while the 5% fractional error is 50. The larger scatter of the veto rates can be explained by the position dependence of the veto dome triggers. For example, a low energy deposit in the center of the dome may not trigger the dome while the same energy deposit near the sides may. The ~5% fractional error is a measure of the total variance between the different veto domes.

V.D.1 Gamma-1 Rate Dependence on the Veto2 Rate

The modulation of the raw Gamma-1 rate (integrated Gamma-1 counts for the entire super-packet with only hardware selections recorded in the HKD dataset) with the instantaneous veto rate is shown (figure V.D.6) for TJD 9725. Two separate populations are present in the scatter plot.

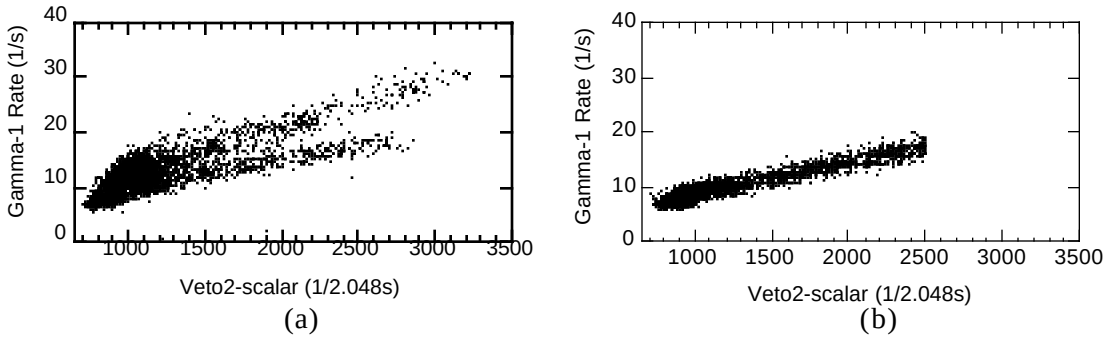

Figure V.D.6 (a) The raw Gamma-1 rate as a function of the veto2-rate for TJD 9725 and (b) the same with EHORA ≥ 45˚ and times >30 minutes after SAA passages for TJD 9720–9727.

The atmospheric flux of gamma rays is intense and results in higher Gamma-1 rates for Earth viewing. The rates are also high for times after SAA exit due the activation within the instrument. These two effects are removed by looking at the raw Gamma-1 rates for sky-viewing (EHORA ≥ 45˚) and times >30 minutes after SAA passages. The raw-event rates now show a linear dependence with the instantaneous veto rates. The modulation of the event rates with the veto rates is indicative of the presence of a prompt instrumental background component.

V.D.2 ToF Components versus Veto2 Rate

In our discussion of the background in ToF space (section V.A), we examined the modulation of the ToF peak to gain insight into the background events. For example, we attributed the walk of the ToF peak (gaussian) position to type C background events that have lower ToF values and dominate the count spectrum at certain energies.

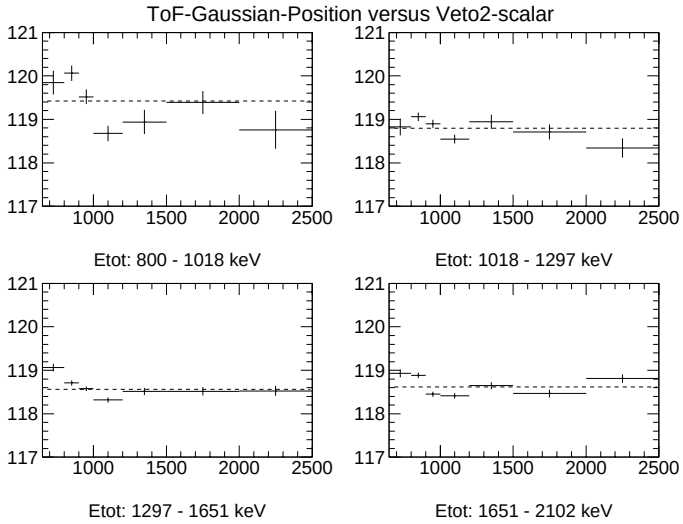

Figure V.D.7 The fitted ToF-peak position as a function of their veto2-rate bin from 800–2102 keV in ETOT. The trend for a decreasing ToF-peak position with increasing veto2-rate is seen above ~1 MeV.

We now investigate the behavior of the ToF spectra as a function of the veto2 rate. As all of the 4 veto-domes operate similarly and are linearly related to one another, in principle any of the veto-dome scaler are adequate. The veto2-dome scaler was originally chosen since it has a relatively high energy-deposit threshold (~1 MeV) and is well shielded being deep within the instrument thus minimizing any contamination from high-energy photons. It will be shown in section VI.G that this effect is negligible. To investigate the veto2-rate dependence of the ToF spectrum and its components, we study the combined Virgo and SGP data in 15 logarithmic bins of total energy. Each ToF spectrum was fit using the Exponential-ToF model with 6 free parameters.

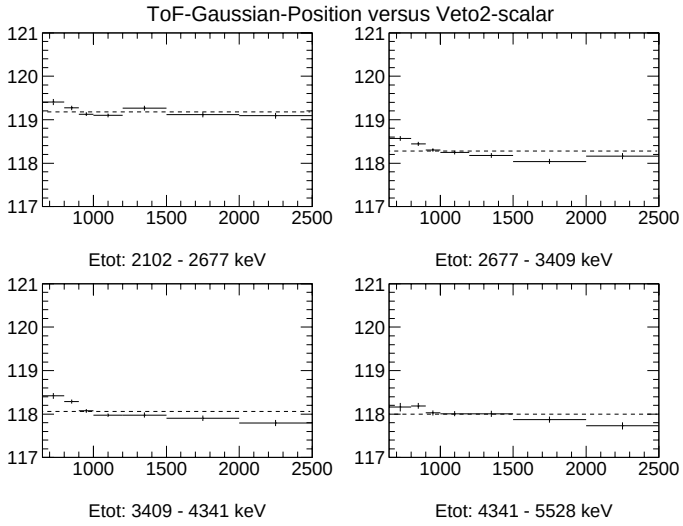

Figure V.D.8 The fitted ToF-peak position as a function of their veto2-rate bin from 2102–5528 keV in ETOT. The trend for a decreasing ToF-peak position with increasing veto2-rate is seen in all cases.

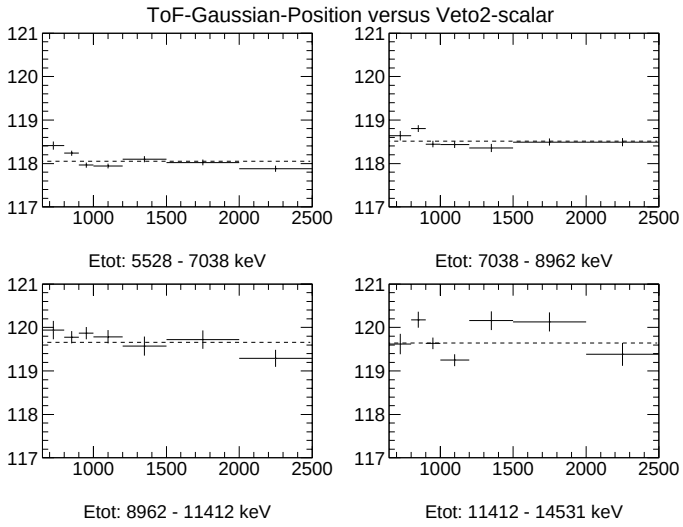

Figure V.D.9 The fitted ToF-peak position as a function of their veto2-rate bin from 5528–14531 keV in ETOT. The trend for a decreasing ToF-peak position with increasing veto2-rate is seen below 9 MeV.

Figures V.D.7–10 shows the fitted gaussian-positions as a function of the veto2 rate for the 15 ETOT bins. Between about 1 and 8 MeV, there is a small (0.4–0.6 channel) but definite trend for a decreasing ToF-peak position (from 117.8 to 118.4) with increasing veto2 rate. Since, the instrumental background above 4.2 MeV is prompt in nature, the shift

of the ToF-peak position with veto rate is due to the modulation of the prompt background contained in the ToF-peak rates. The shift to lower ToF values with higher veto rates is consistent with the presence of an intense prompt component peak at lower (<120) ToF channel of type C events. Since the background rate decreases with lower veto2 rates, the signal at channel 120 becomes more important and shifts the fitted ToF-peak positions to a higher value. Below ~1 MeV and above ~10 MeV, there is no strong evidence for any variations in the peak position with veto rate. (figures V.D.10). Above 10 MeV, the ToF-peak positions between 119–120 ToF channel suggest that the background events here are of type A and hence no shifts would be expected.

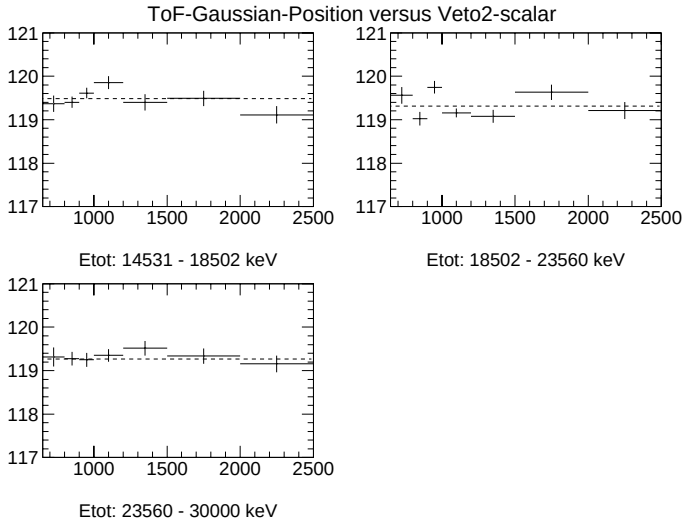

Figure V.D.10 The fitted ToF-peak position as a function of their veto2-rate bin from 14531–30000 keV in ETOT. No trend for a decreasing ToF-peak position with increasing veto2-rate is observed.

The gaussian widths do not show any variations with the veto2 rate. The gaussian width versus veto rate is shown in figures V.D.11 for a small sample of energy bins. The fit results indicate a constant value for the gaussian widths for all veto2 rate bins.

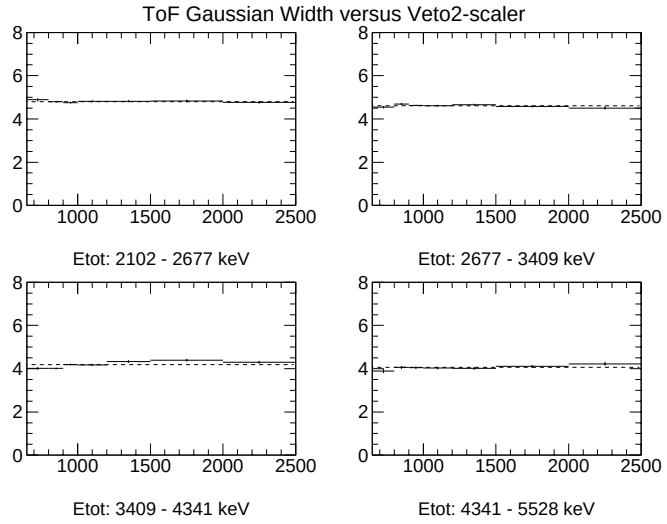

Figure V.D.11 The fitted ToF-peak widths as a function of their veto2-rate bin for a sample of ETOT (from 2102–5528 keV) showing no variations with veto2-rate.

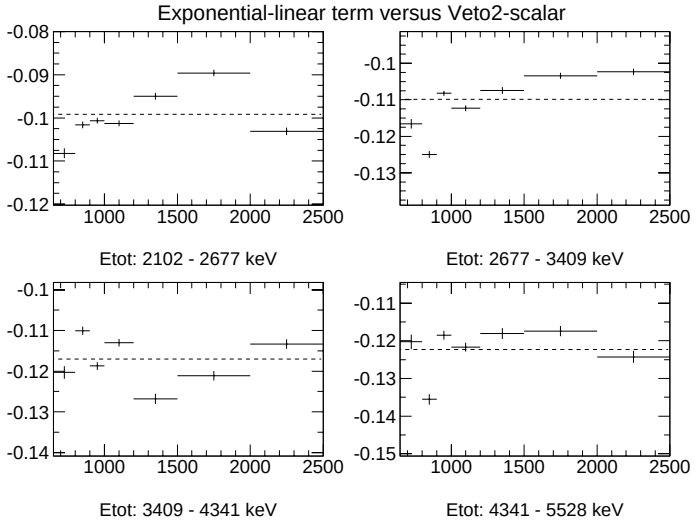

Figure V.D.12 The fitted ToF-peak exponential-linear terms as a function of their veto2-rate bin for a sample of ETOT (from 2102–5528 keV) showing no clear modulation with veto2-rate.

The other functional form of relevance is the exponential-linear term from the exponential-ToF function, defined as P2 in equation 5.1. The exponential-linear term is inversely related to the *e*-folding parameter of the exponential function. The exponential-linear term versus veto rate is shown in figures V.D.12 for a small sample of energy bins. The exponential-linear term shows no obvious trend with veto2 rate.

V.D.3 An Improved ToF Fit between 4.2 and 9 MeV

Between 4.2 and 9 MeV, the single gaussian Exponential-ToF fit (described in section V.B, henceforth called 1gToF) yields a gaussian position around 118 ToF channels, where the single gaussian represents the entire forward ToF-peak. Example fits for the 4.2–6 and 6–9 MeV bins using the P15VSGP data are shown in figure VI.D.13.

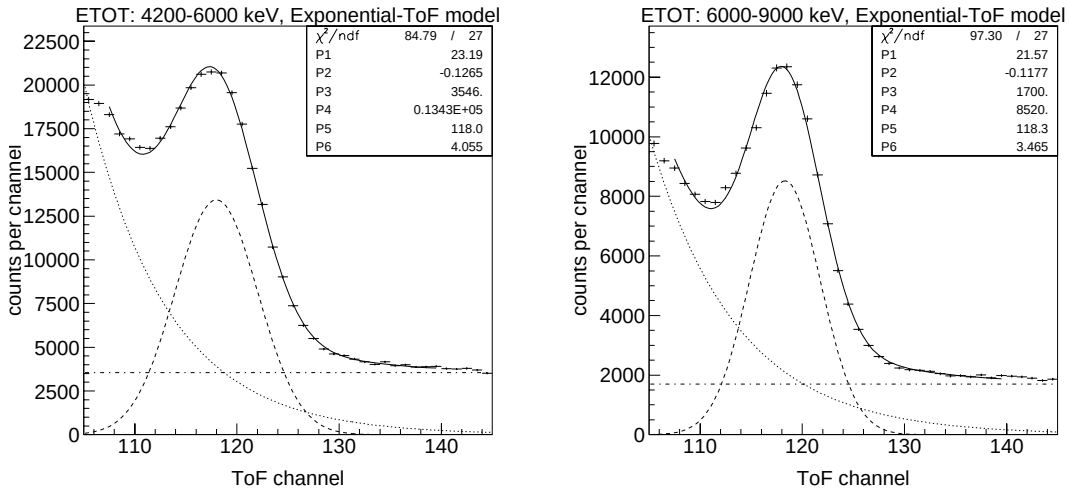

(a) (b)

Figure V.D.13 The (a) 4.2–6 and (b) 6–9 MeV ToF spectrum using a 1gToF fit for P15VSGP data with standard-CDG selections.

We now improve the description of the 4.2-9 MeV ToF spectrum by using a two gaussian Exponential-ToF model (henceforth termed 2gToF). The motivation for a two gaussian model comes from the fact that (1) the background events between 4.2 and 9 MeV are prompt type C events involving multiple-gamma events originating from the mass around D1; (2) the forward peak position of the type C events lie around channel 116; and (3) the single gaussian peak position is ~118 between the type C event peak (~116) and the type A event peak (~120).

The type C event peak around channel 116 is clearly seen in the simulated ToF spectrum of the ^{24}Na decays (figure V.D.14). A shift of ~4 ToF channels correspond to 1 ns delay. A photon travels about 30 cm (1 foot) in 1 ns, hence a shift of 4 ToF channels suggests that the photons traverse ~30 cm on average before interacting in a D1 module. With the diameter of a D1 module being 28 cm and the detector edges being ~15–20 cm apart, a mean path-length of ~30 cm before interaction is reasonable.

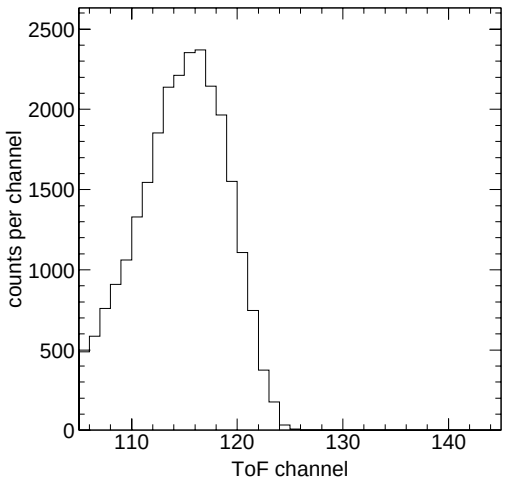

Figure V.D.14 The ^{24}Na ToF spectrum computed from simulations showing the ToF-peak around channel 116.

A two-gaussian model for the ToF spectrum is better suited to extract the signal (type A) at channel 120. As the name suggests the 2gToF model consists of two gaussians in addition to the exponential and the constant. One of the gaussian positions is fixed at channel 120 to represent type A events while the other gaussian position is allowed to vary. Although the peak widths are determined in the fit, they are required to be the same. The ToF resolution is sensitive to the D1 and D2 energy deposits and is not expected to vary greatly between channels 120 and 116. Some important parameters to compare between the two ToF models (i.e., 1gToF and 2gToF) are the position of the second gaussian and the amplitude of both peaks listed in table V.D.1. For comparison, the results from the 1gToF fit are also shown. The results from fitting the P15VSGP data in the 4.2–6 and 6–9 MeV bins with the 2gToF model are shown in figures V.D.15 and V.D.16 (compare with figure V.D.13).

In all case the peak widths are narrower for the case of the two-gaussian ToF fit. The ToF-peak width decreases from 4.05 to 3.27 channels for 4.2–6 MeV and from 3.46 to 2.81 for channels for 6–9 MeV bins. For both energy bins the position of the lower gaussian is 116 ± 0.5 channels. This is the region in ToF space where we expect the type C events to occur. This consistency between the position of lower peak in the data with the expected position of type C events supports the assumptions underpinning the 2gToF model [see also Weidenspointner 1998].

Table V.D.1 Results of the 1gToF and 2gToF fits to the 4.2–6 and 6–9 MeV bins.

Data	Energy	1gToF	1gToF	2gToF	2gToF	G@120	G@116
	MeV	position	width	position	width	fraction of G@118	
V+S	4.2–6	118.0 ± 0.023	4.055 ± 0.022	115.7 ± 0.069	3.274 ± 0.029	51.08	44.78
	6–9	118.3 ± 0.023	3.465 ± 0.022	116.3 ± 0.055	2.807 ± 0.024	53.00	44.14
Virgo	4.2–6	118.0 ± 0.029	4.038 ± 0.028	115.8 ± 0.078	3.275 ± 0.033	50.34	45.13
	6–9	118.3 ± 0.029	3.446 ± 0.028	116.4 ± 0.098	2.842 ± 0.039	52.41	44.93
SGP	4.2–6	118.0 ± 0.040	4.087 ± 0.038	115.6 ± 0.104	3.253 ± 0.044	51.85	43.62
	6–9	118.2 ± 0.039	3.505 ± 0.038	116.1 ± 0.110	2.781 ± 0.047	53.27	43.73

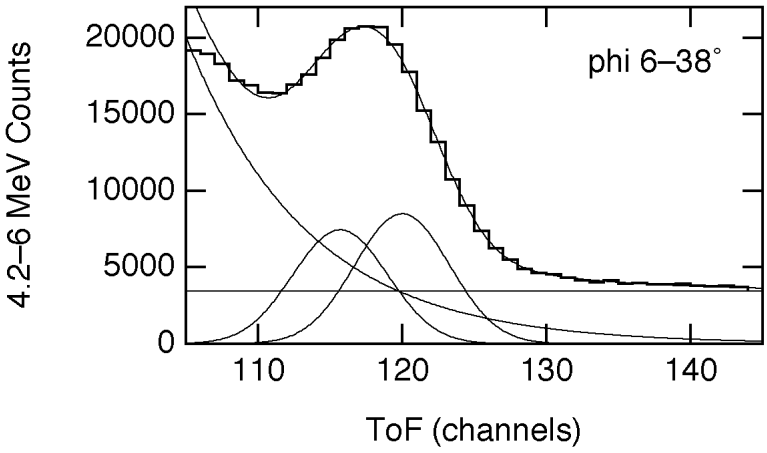

Figure V.D.15 The 4.2–6 MeV all-veto P15VSGP ToF spectrum fit using the 2gToF model.

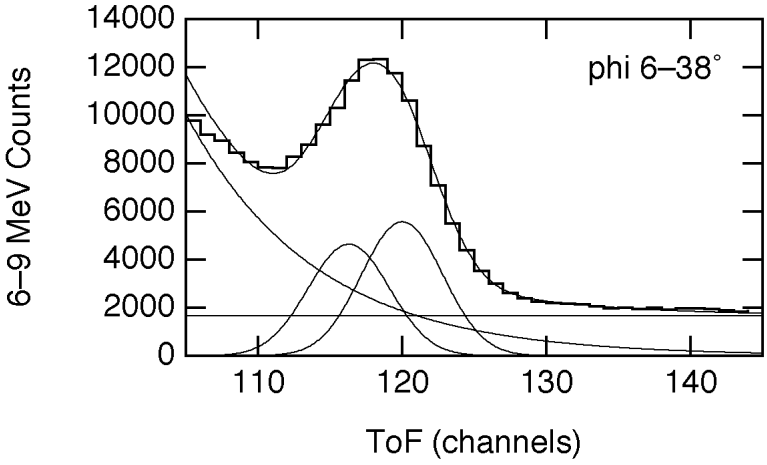

Figure V.D.16 The 6–9 MeV all-veto P15VSGP ToF spectrum fit using the 2gToF model.

Overall, we recover over 95% of the single gaussian counts (1gToF fit) with the two gaussian model. By comparing the ratio of the counts in the gaussian at channel 120 and at channel 116 from the 2gToF fit with the counts assigned to the single gaussian at channel 118 from 1gToF, we can determine the decrease in the computed background counts from the 2gToF fits. These ratios are labeled as G@120 and G@116 respectively in table VI.C.1. Typically, the measured counts in the ToF-peak at channel 120 are about 50–55% of the counts in the single ToF-peak at channel 118. This is a factor of 2 improvement in the S/B ratio for the ToF-peak at channel 120. Henceforth, the 2gToF model is adopted as the preferred method to compute the forward-peak count rates in the 4.2 to 9 MeV range.

V.E. Prompt Background Component: Veto Growth Curves

V.E.1 Overview

Plots of event rate versus the veto rate are called veto-growth-curves or VGCs. The event rate usually increases or "grows" with the veto rate, hence the terminology. For a given energy interval, the VGCs are determined by first fitting the ToF spectrum for seven veto2-rate bins. The veto2-rate bins are generated with veto2-bin boundaries at 650, 800, 900, 1000, 1200, 1500, 2000 and 2500 veto2 rate. All data are livetime corrected.

There are 3 distinct regions in ETOT space that are not influenced by the long-lived background, these are (1) the 2.2 MeV line; (2) the 4.2–9 MeV region, dominated by prompt type C events; and (3) the 9–30 MeV region where the background is from type A events. We also expect the exponential and the constant components of the ToF spectrum to be prompt since they are produced by the prompt local photon flux.

The prompt background modulates with the cosmic-ray flux incident on COMPTEL. The veto rate is a direct measure of the instantaneous cosmic-ray intensity. The basic goal is to model the prompt background by parameterizing the measured event rates with the veto rates. Once the framework to model the prompt background is developed, we can then correct for its effects by extrapolating to a zero cosmic-ray intensity. Previous gamma-ray experiments have also used an extrapolation technique to measure the cosmic diffuse emission. The balloon experiments have usually used *atmospheric growth curves*. These are generated by ordering the event rate with the amount of atmosphere above the detector (Schönfelder,

Graml, and Penningsfeld 1980, White et al. 1977). The atmospheric photon flux decreases with altitude, therefore the instrument measures a decreasing rate as it ascends to a higher altitude. The Apollo 17 gamma-ray spectrometer was mounted on a boom (Trombka et al. 1977). Measurements at various boom extensions was used to estimate the spacecraft induced background. Mazets et al. (1975) used the modulation of the instrumental 511 keV line with rigidity to model the background.

The technique for constructing a VGC is as follows: for each ETOT energy bin, I first generate and fit the ToF spectrum derived from the sum of all veto-rate bins. From this fit I determine the mean gaussian-position, gaussian-width and the exponential-linear term. Then I fit the veto-separated ToF spectrum keeping these 3 parameters fixed and only letting the normalization parameters vary freely; namely the normalization for the gaussian(s) and exponential and a constant. By this method I reduce the number of free parameters from 6(7) to 3(4) while fitting the veto-separated ToF spectra. The numbers in parenthesis are for the 2gToF model used in the 4.2–9 MeV range.

V.E.2 The 2.2 MeV VGC

The 2.2 MeV VGC behavior, being a pure prompt background component, serves as a diagnostic of the relationship between the general prompt-background and the veto rates. The behavior of the 2.2 MeV photon rate is well described with an exponential function in cutoff-rigidity and a linear function in Earth-center elevation angle (GCEL). The measured 2.2 MeV count rate is consistent with zero 2.2 MeV photon rate at infinite cutoff-rigidity (Weidenspointner et al. 1996).

The 2.2 MeV line intensity is determined by fitting such ETOT spectra with an exponential plus gaussian function (5 parameters). The ETOT fit for the 2.2 MeV photopeak using P15VSGP data is shown in figure V.E.1 showing that the fit function adequately describes the data. The measured mean position and width are ~2237 keV and ~75.5 keV, whereas the expected values from ground calibrations are 2223 keV and 67 keV respectively (Schönfelder et al. 1993). The 2.2 MeV events necessarily have large scatter angles to register telescope events. This represents a larger energy loss fraction in D1 compared with external 2.2 MeV photons. Since the energy resolution of D1 is poorer than that of D2, the internal

2.2 MeV events have a broader energy resolution. Furthermore, fluctuations in PMT gains in orbit also contribute to broadening the peak.

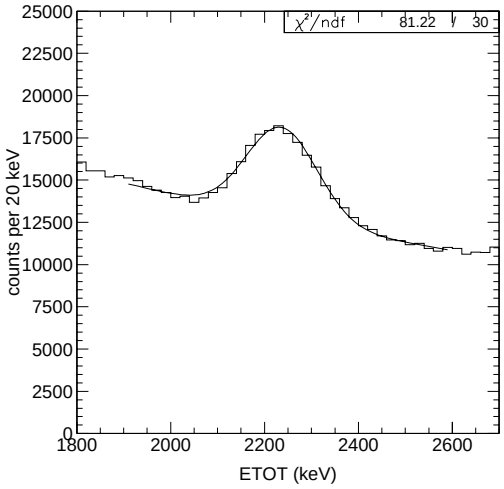

Figure V.E.1 The 2.2 MeV ETOT fit for the veto-integrated P15VSGP data showing that the fit function adequately describe the data.

There are no large fluctuations in the average 2.2 MeV position, resolution and the average 2.2 MeV count rate for the eight different data subsets (see figures V.E.2 and V.E.3). The instrument configuration appropriate to the Phase 1 Virgo data (see chapter IV) results in a lower effective area and hence the P12V event rate is artificially lower compared to the others phases. Except for the P12V data, the 2.2 count rate is stable over time indicating no significant global variation in the cosmic-ray intensity.

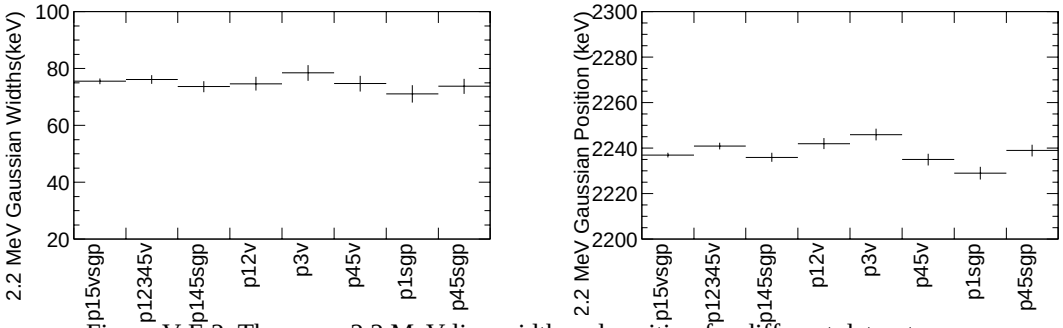

Figure V.E.2 The mean 2.2 MeV line width and position for different datasets.

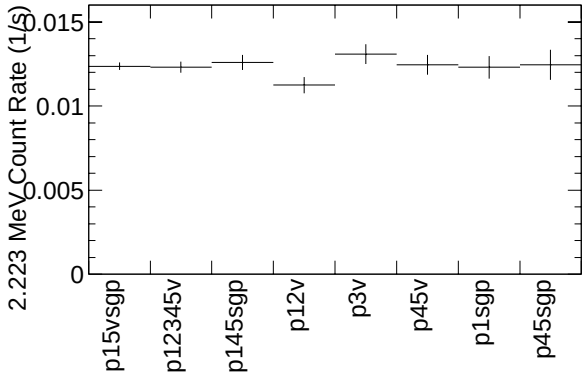

Figure V.E.3 The mean 2.2 MeV line count rate for different datasets.

In all cases, the 2.2 MeV peak widths are constant for all veto2 rates (see figure V.E.4). However, the peak positions does show a trend for a decreasing line position with increasing veto2 rate, from 2245 to about 2225 keV (see figure V.E.4). The variation is small (~1.5%) but significant and is probably due to the lower 2.2 MeV S/B with decreasing veto2 rate.

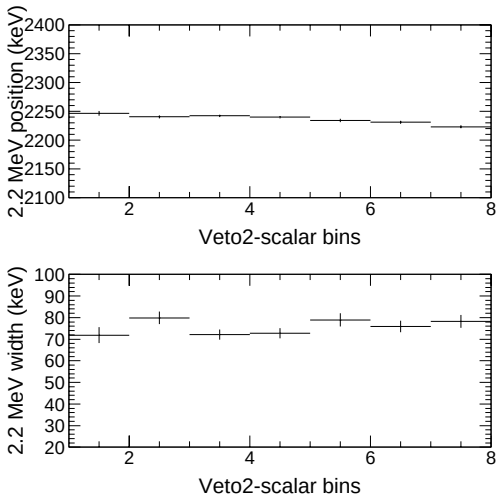

Figure V.E.4 The 2.2 MeV line width and line position as a function of veto rate.

The resulting 2.2 MeV VGC for P15VSGP data is shown in figure V.E.5. The 2.2 MeV VGC is linear and has been fit with a linear function (y=mx+c) and a proportionality function (y=ax). The 2.2 MeV VGCs for the P12345V and P145SGP data are plotted in figures V.E.6 and the results of these fits are tabulated in table V.E.1 and shown in figures V.E.6. To generate the 2.2 MeV VGCs for smaller datasets of P12V, P3V, P45V, P1SGP and P45SGP

observations, the 2.2 MeV line position and width were held fixed. A detailed comparison of the fit results by letting all parameters vary and fixing the gaussian position and width for the P15VSGP, P12345V and P145SGP data yielded no differences in the fit parameters except that the errors in the amplitude of the 2.2 MeV line decreases because of fewer free parameters. The shift in 2.2 line position of ~20 keV is much less than the instrumental line resolution (~80 keV).

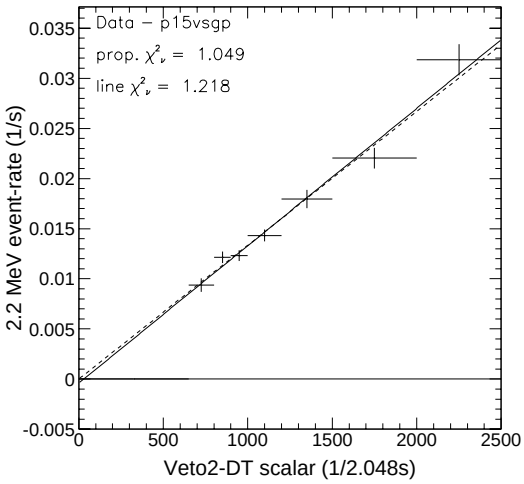

Figure V.E.5 The 2.2 MeV VGC for P15VSGP data fit with a linear and a proportional function.

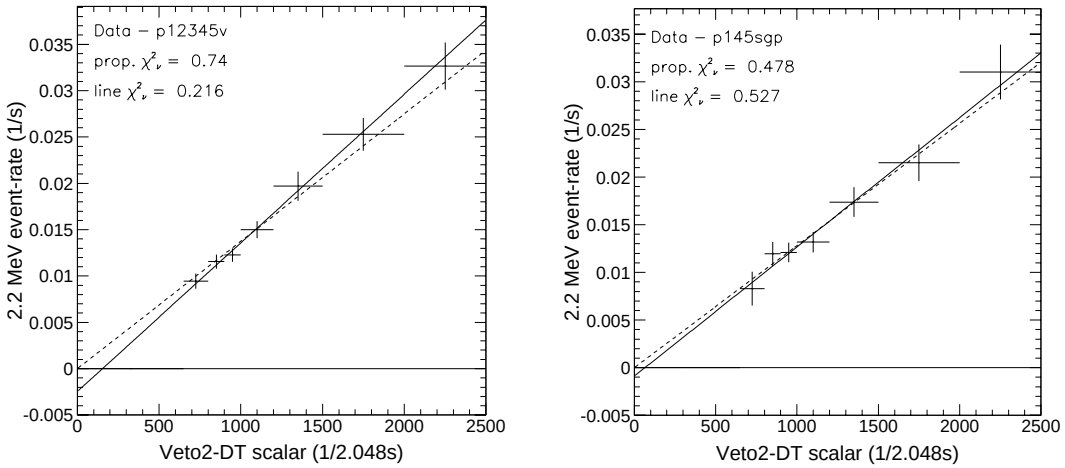

Figure V.E.6 The 2.2 MeV VGC for (a) P12345V data and (b) P145SGP data fit with a linear and a proportional function.

Table V.E.1 The 2.2 MeV VGC fit results.

Data	VGC fit parameter	linear function	proportional function
P15VSGP	red. chi-square	1.218	1.045
	slope	(1.370 ± 0.084) E-5	(1.335±0.024) E-5
	constant	-0.000409 ± 0.000917	
	veto2-rate intercept	29.87 ± 66.94	
P12345V	red. chi-square	0.2161	0.7408
	slope	(1.605 ± 0.131) E-5	(1.375±0.036) E-5
	constant	-0.002467 ± 0.001348	
	veto2-rate intercept	153.71 ± 83.99	
P145SGP	red. chi-square	0.5279	0.4780
	slope	(1.356 ± 0.161) E-5	(1.282±0.046) E-5
	constant	-0.000887 ± 0.001839	
	veto2-rate intercept	65.41 ± 135.62	

All of the 2.2 MeV VGCs fits have acceptable reduced chi-squares, for both the proportional and linear models (see figure V.E.7). For the straight-line model fits, the total P15VSGP data (which has the smallest statistical uncertainty) show a non-zero *x*-intercept only at the +0.5σ level corresponding to 29.9 ± 66.9 veto2 rate. The P12345V data show a positive *x*-intercept at the 2σ and the P145SGP data show positive *x*-intercept at the +0.5 sigma level. The *x*-intercept from linear fits to the 2.2 MeV VGCs for different datasets are listed in table V.E.2 and plotted in figure V.E.8.

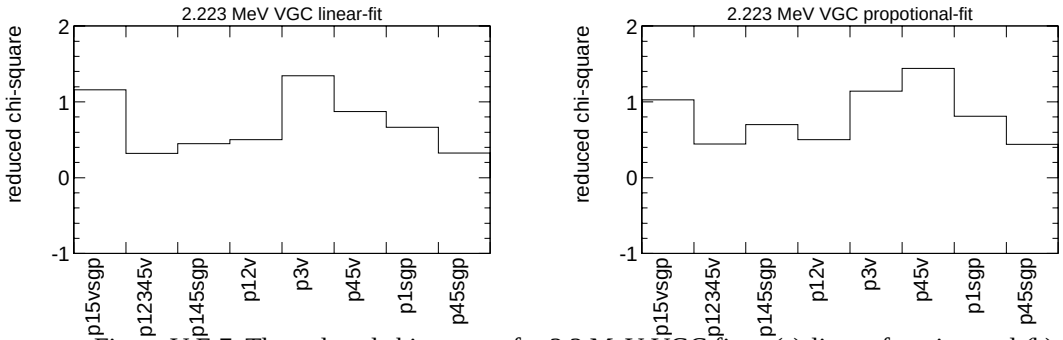

Figure V.E.7 The reduced chi-squares for 2.2 MeV VGC fit to (a) linear function and (b) a proportional function.

The proportional model gives acceptable reduced chi-squares in all cases and is a valid description of the data. There are no indications to suggest any systematic deviation from proportionality. Hence the 2.2 MeV line rate can be considered to be consistent with a zero rate at zero veto2 rate. This, in turn, suggests that the prompt background (especially the prompt background within the forward-ToF peak) extrapolates to zero at zero veto rate.

Table V.E.2 The 2.2 MeV *x*-intercepts for different datasets.

Data	2.2 MeV *x*-intercept
P15VSGP	29.87 ± 66.94
P12345V	153.87 ± 83.99
P145SGP	65.41 ± 135.62
P12V	72.25 ± 102.58
P3V	-42.65 ± 113.31
P45V	219.09 ± 105.47
P1SGP	-203.61 ± 158.25
P45SGP	-154.63 ± 152.18

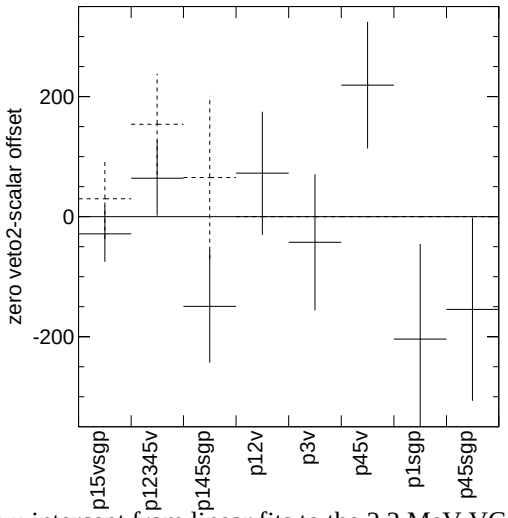

Figure V.E.8 The *x*-intercept from linear fits to the 2.2 MeV VGCs for different datasets.

I have used the 1σ error in the x-intercept of the P15VSGP 2.2 MeV data as a measure of the 1σ systematic uncertainty on the assumption of a zero prompt background at zero veto2 rate. The effect of using this offset value in deriving the CDG fluxes is discussed later (see section VI.G).

V.E.3 The VGCs above 4.2 MeV

Figure V.E.9–11 shows the P15VSGP VGCs for the gaussian, exponential and constant components in five ETOT bins above 4.2 MeV (bin boundaries at 4.2–6–9–12–17–30 MeV). The gaussian component refers to the single gaussian in the 1gToF model above 9 MeV and to the gaussian at channel 120 in the 2gToF model between 4.2 and 9 MeV. Between 4.2 and 9 MeV the contribution of the second gaussian at ~116 has been added to the exponential component. We first note that a straight line fit adequately describes all VGCs in all energy ranges. The count rates typically modulate by a factor of 2 to 3.5 between the veto endpoints.

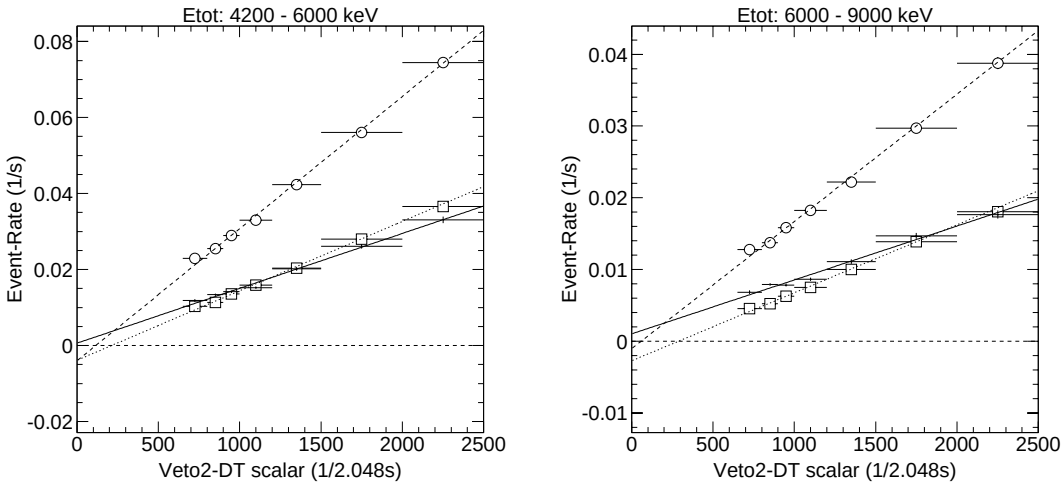

Figure V.E.9 The P15VSGP VGCs for the three ToF components in 4.2–6 and 6–9 MeV regions (+: gaussian, square: constant, circle: exponential).

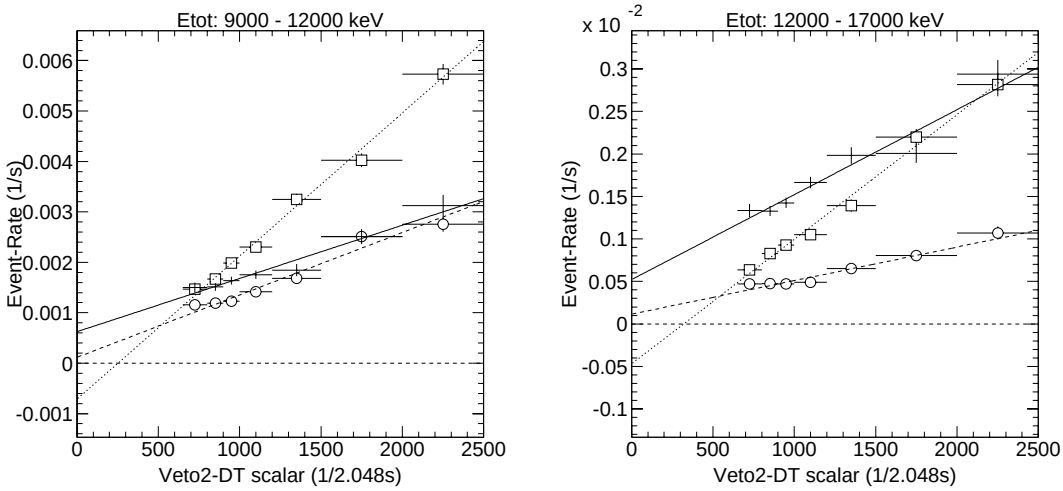

Figure V.E.10 The P15VSGP VGCs for the three ToF components in 9–12 and 12–17 MeV regions (+: gaussian, square: constant, circle: exponential).

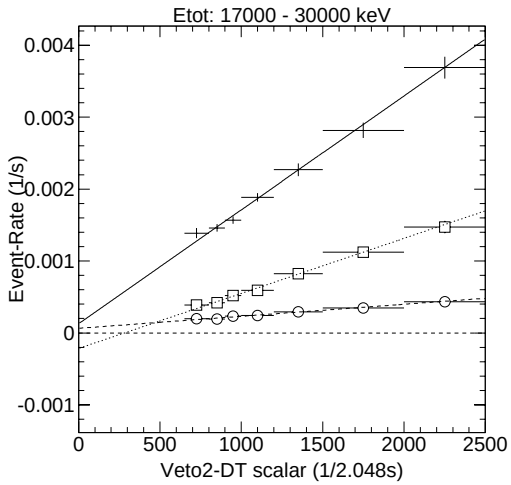

Figure V.E.11 The P15VSGP VGCs for the three ToF components in the 17–30 MeV region (+: gaussian, square: constant, circle: exponential).

VGC slopes

The VGC slope is a direct measure of the modulation in the VGCs. The slopes of the 3 ToF components as a function of ETOT are plotted in figure 4.E.12. The slopes of the exponential and constant components are monotonically decreasing with energy, i.e., the VGCs are getting flatter. The gaussian slope shows a more complicated behavior, it decreases from 4.2–10 MeV, above which it increases with energy. The gaussian count spectrum also shows an increased rate above 9 MeV, while the exponential and constant continues to decrease in intensity. The increasing slope above 9 MeV implies that the increased ToF-peak rate above 9 MeV is from prompt background events. The prompt component above 9 MeV is associated with type A events since the ToF peak is located near channel 120. The photon energies are above the nuclear-energy domain (1–9 MeV) suggesting that they not associated with nuclear interactions. The new prompt background component is probably electromagnetic in origin, electron bremsstrahlung photons or photon from pair-production above the veto domes. Similar gaussian VGC behavior is also seen for other datasets.

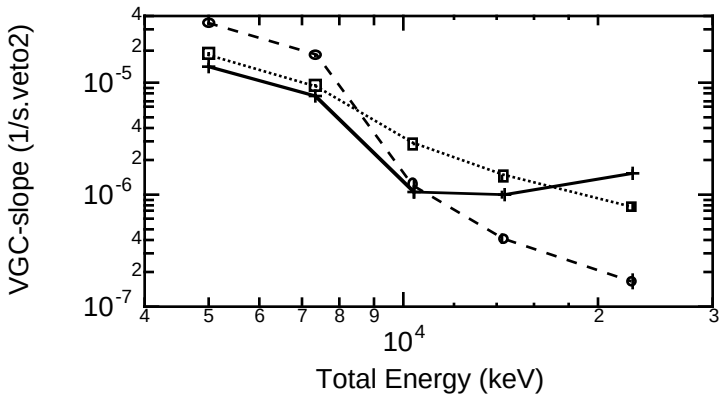

Figure V.E.12 The VGC slopes for the three ToF components above 4.2 MeV (circle: exponential, square: constant, +: gaussian).

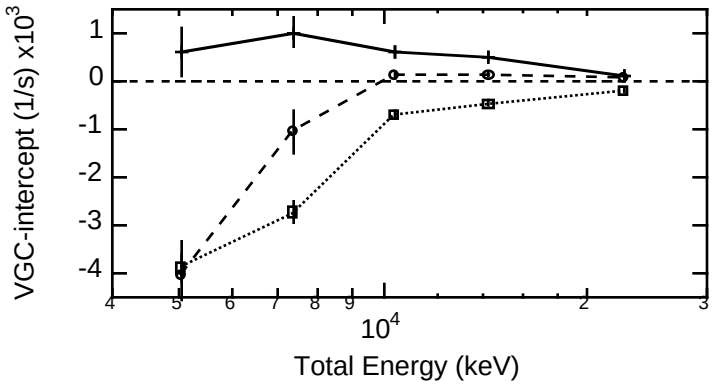

Figure V.E.13 The VGC *y*-intercepts for the three ToF components above 4.2 MeV (circle: exponential, square: constant, +: gaussian).

The VGCs for the Exponential component

The exponential component consists of multiple photon events (type C) originating from the spacecraft and are presumed to be prompt in nature and hence should modulate with the veto rates. The linear modulation with veto rates is seen at all energies. Although it is encouraging that the exponential component linearly modulates with veto rate, the resulting *y*-intercept is not well behaved, at least for the P15VSGP dataset, where the intercept is negative below 9 MeV and positive above it (see figure V.E.13). The *y*-intercept for exponential component in the 4.2–9 and 9–30 MeV VGCs are shown in figure V.E.14. The exponential intercepts in 9–30 MeV are similar for the different datasets showing a positive intercept at the 1σ level. The exponential intercept in 4.2–9 MeV shows a much greater fluctuation and varies from zero to a significantly negative intercept (P3 and P45 data). There

are no apparent systematic trends for the exponential intercept. Naively, we expect the exponential VGC to pass through zero as it is a prompt component, but this is not the case. There are no general trends to suggest an explanation, the reasons for such an exponential-intercept behavior is not well known.

Recall that the fits to the exponential component fail far from the ToF peak, meaning that the continuum far from the ToF peak is not exponential in shape. An exponential (or quadratic) function is used simply to represent the continuum underneath the forward-peak. The exponential and constant rates are determined from the ToF-peak region, which is not best suited to study them. The low ToF channels, the region between channel 100–105 are better suited to study the exponential component as these events are dominated by type C events originating in the spacecraft. A detailed study of the exponential component is not related to the goals of this thesis. Nevertheless, even with the high rates assigned to the exponential and the overall approximations stated above it is encouraging to see that a linear VGC is able to predict a zero intercept to within <10% of the average exponential rate.

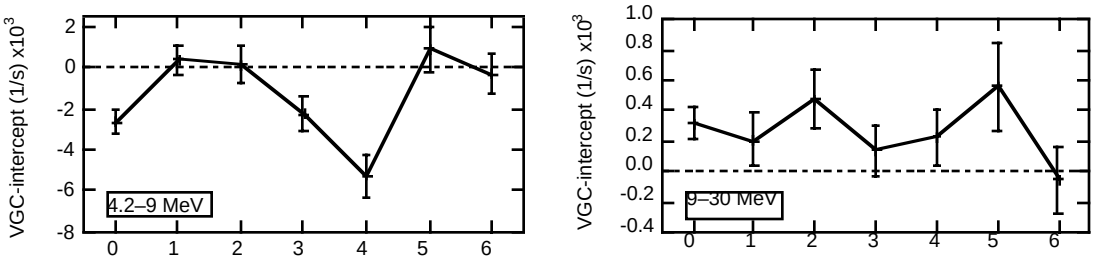

Figure V.E.14 The (a) 4.2–9 MeV and (b) 9–30 MeV exponential-component VGC intercepts for the eight datasets (P15VSGP, P12345V, P145SGP P12V, P3V, P45V, P1SGP and P45SGP).

The VGCs for the Constant component

The constant component is comprised of chance coincidence events (type B) triggered by the photon bath surrounding COMPTEL. The accidental events are produced when two separate photons independently interact with each of the two detectors within the required ToF window. The photons are prompt in nature and are expected to modulate with the veto rates. The linear modulation with veto rates is seen at all energies. In principle, the accidental event rate between two detectors is equal to the product of the two individual detector rates multiplied by the time-window for accepting events. The point to note is that the accidental

rate is proportional to the product of two independent rates, where each of the detector rates is proportional to the veto rates. Therefore, the accidental rate probably has a higher order dependence (such as a quadratic) with veto rate, rather than a linear modulation. The measured accidental rates, however, show no large curvature in the VGCs in the range of measured veto rates. They are well described by a straight line fit. However, the straight line fits to the accidental VGCs consistently have negative *y*-intercepts as one would expect from a linear extrapolation of a quadratic function. Since the straight line fit cannot account for the flattening of the accidental VGC at low veto rates it yields in a negative y-intercept. As mentioned before the ToF fits are optimized to calculate the gaussian components. An accurate study of the accidental events requires examining the events at higher ToF values.

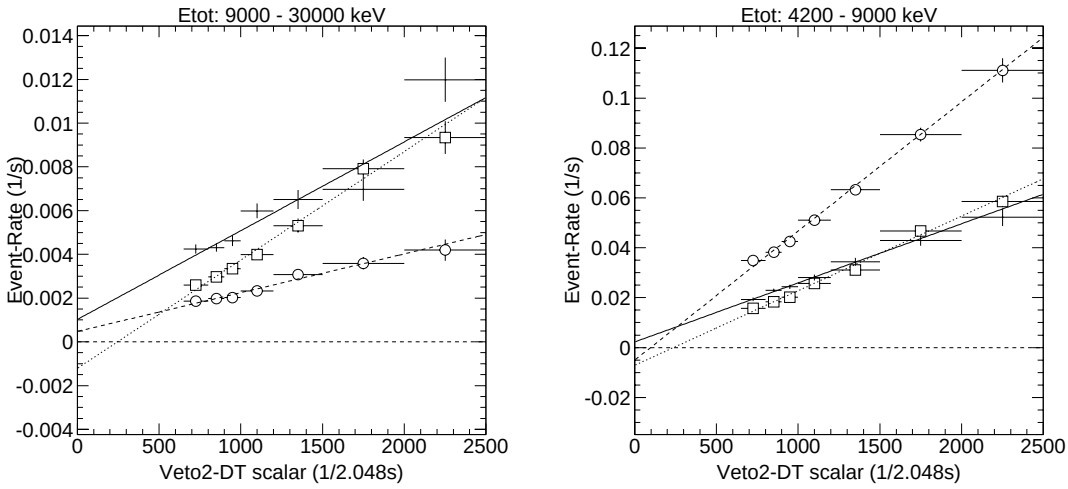

Figure V.E.15 The 9–30 MeV and 4.2–9 MeV VGCs for the P12V data (+: gaussian, square: constant, circle: exponential).

The VGCs for the Gaussian component

The gaussian component (at channel 120) shows a clear linear dependence on veto rate. The presence of modulation, the fact that the VGCs are not flat, is indicative of the presence of prompt background within the gaussian count rates. The gaussian counts consist of contributions from the prompt background in addition to the CDG component. The gaussian VGCs have a non-zero positive *y*-intercept giving a measure of the steady-state emission at zero cosmic-ray intensity. The behavior of the 2.2 MeV VGC is relevant to the background in the ToF-peak events since they both are type A events and contribute to the ToF peak at 120.

In addition, the 2.2 MeV photons and the prompt background are produced by the same parent neutron flux. Hence, the background event rate that contaminate the forward-peak modulates in the same manner as the 2.2 MeV rate. A vanishing 2.2 MeV rate at zero veto rate is a strong argument for a zero prompt background in the ToF-peak rates at zero veto rate. Above 4.2 MeV (with no long-lived background) the veto-extrapolated steady-state rate is the CDG count rate.

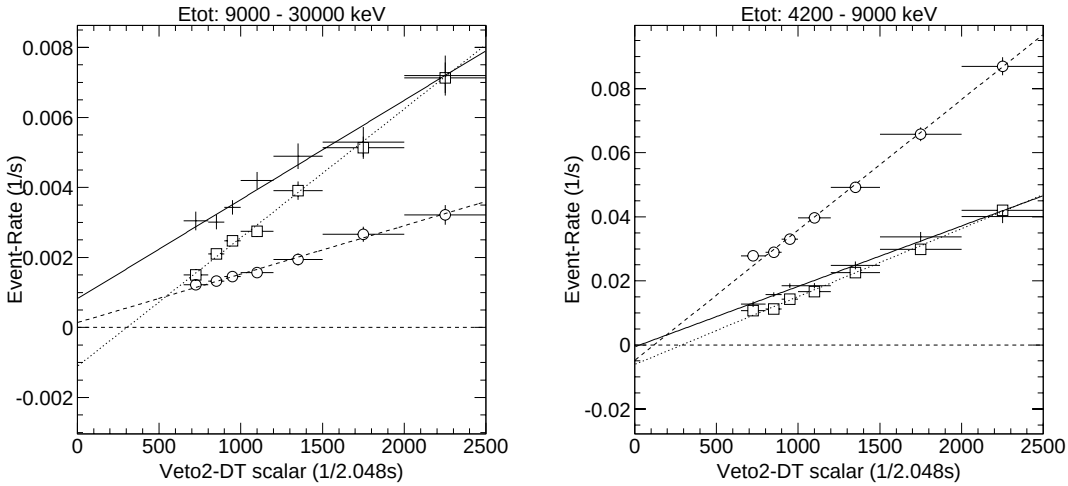

Figure V.E.16 The 9–30 MeV and 4.2–9 MeV VGCs for the P3V data (+: gaussian, square: constant, circle: exponential).

The 4.2–9 and 9–30 MeV VGC are shown in figures V.E.15–19 for subsets of data. The 9–30 gaussian MeV *y*-intercepts and slopes for the data subsets are plotted separately in figures V.E.20. The 9–30 MeV gaussian VGCs are well behaved with roughly the same *y*-intercepts and similar slopes for all datasets. The 4.2–9 gaussian MeV y-intercepts and slopes for the data subsets are plotted separately in figures V.E.21. The 4.2–9 MeV gaussian VGCs are less well behaved, although they still have consistent *y*-intercepts and similar slopes for the different datasets. Improved data selection (as those used in the CDG analysis, section V1.C) further increases the S/B in the 4.2–9 MeV bin resulting in better behaved VGCs.

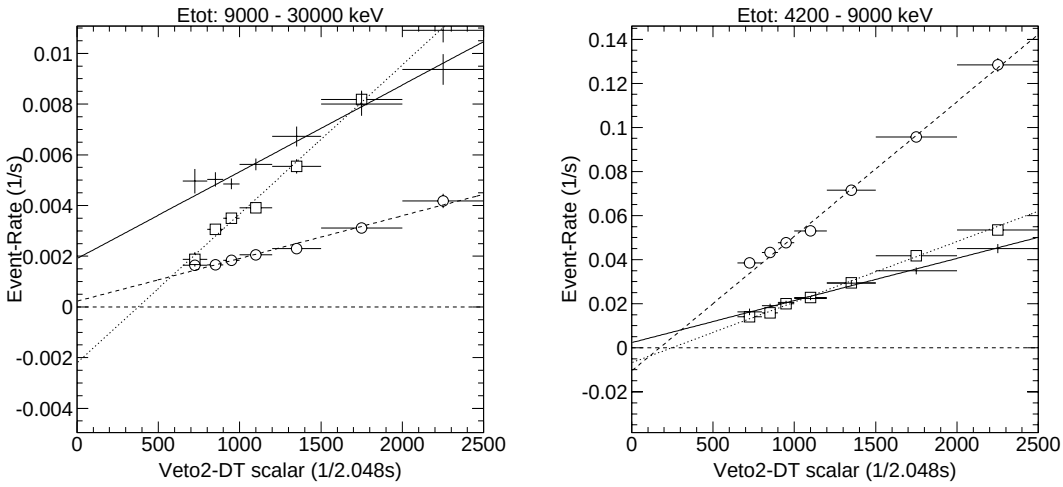

Figure V.E.17 The 9–30 MeV and 4.2–9 MeV VGCs for the P45V data (+: gaussian, square: constant, circle: exponential).

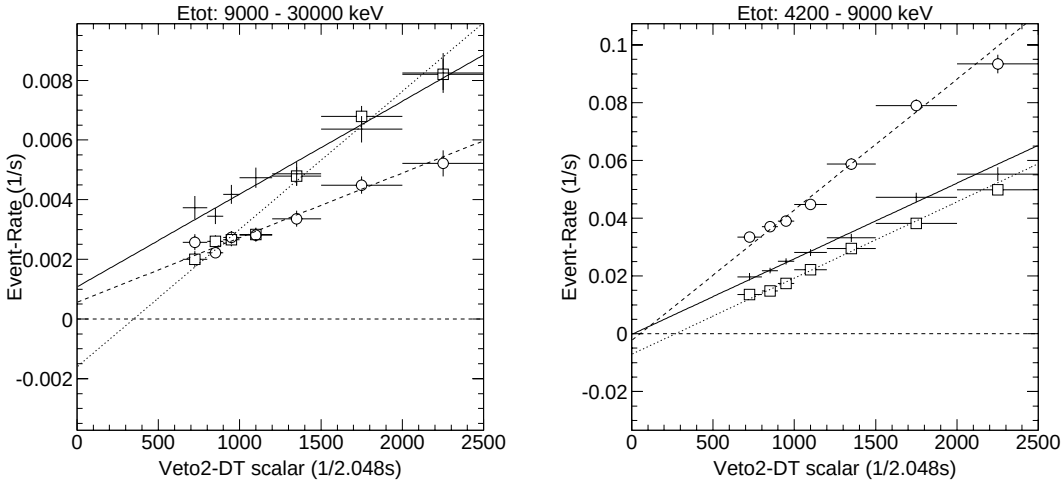

Figure V.E.18 The 9–30 MeV and 4.2–9 MeV VGCs for the P1SGP data (+: gaussian, square: constant, circle: exponential).

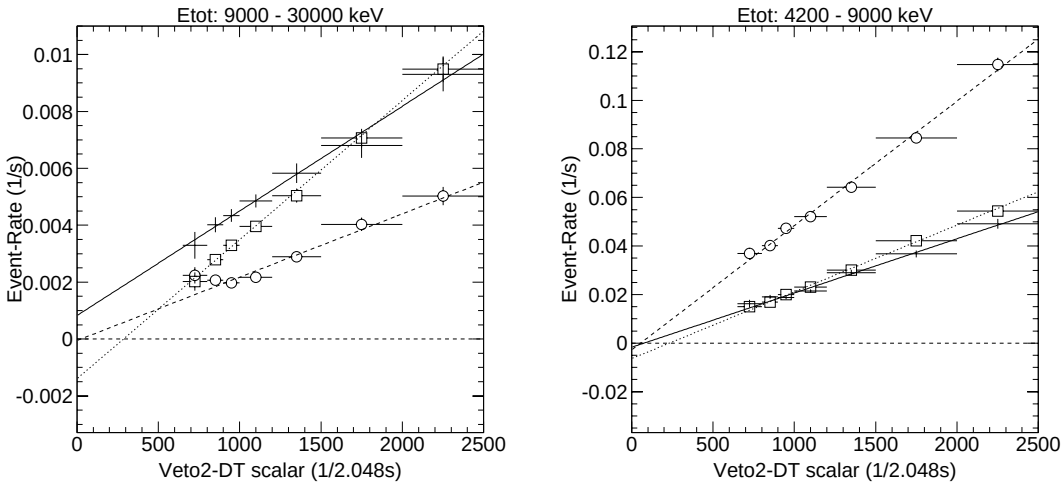

Figure V.E.19 The 9–30 MeV and 4.2–9 MeV VGCs for the P45SGP data (+: gaussian, square: constant, circle: exponential).

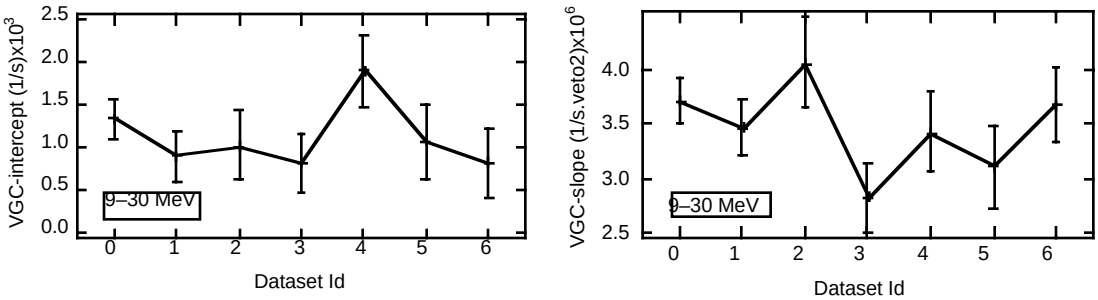

Figure V.E.20 The (a) VGC intercepts and (b) VGC slope in 9–30 MeV for the eight datasets.

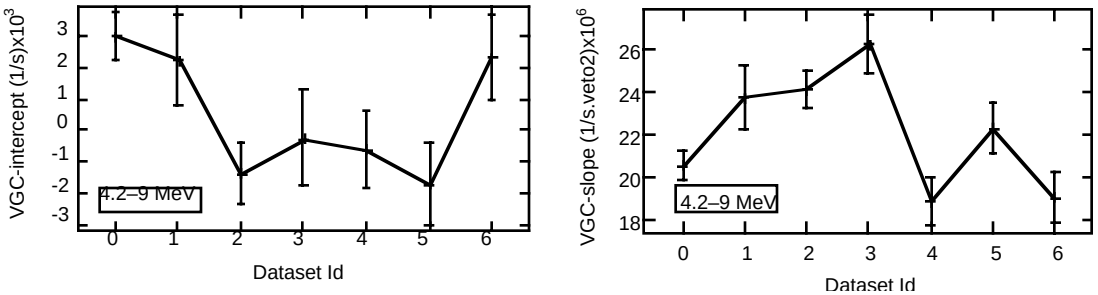

Figure V.E.21 The (a) VGC intercepts and (b) VGC slope in 4.2–9 MeV for the eight datasets.

V.E.4 The VGCs below 4.2 MeV

Above 4.2 MeV the data contains only prompt background. By veto-rate extrapolation we can eliminate the prompt component to determine the CDG count rates. The veto-extrapolation method is valid for any energy interval containing only prompt background and CDG counts. However, below 4.2 MeV the count rates consist of long-lived background

events in addition to the prompt and CDG component. The long-lived background component is not modulated by the instantaneous cosmic rays. The structure of long-lived background events in the VGC is phenomenological and depends on the SAA dose, the isotope half-life and on the orbital SAA-rigidity geometry. The structure of the long-lived background events in veto space and the correct procedure to account for the prompt and long-lived background components are discussed here.

The ^{24}Na VGCs in individual phases

The ^{24}Na long-lived background component is examined as an example of long-lived background VGC. ^{24}Na is a main source of long-lived background in the 1.8 to 4.2 MeV region. Figures V.E.22–25 show the ^{24}Na VGCs for the P1, P4, P5 and P2345 Virgo observations. The VGCs for individual phases show an approximate decreasing ^{24}Na rate with increasing veto rate. Due to the long half-life of ^{24}Na (~15 hours) one might expect a flat ^{24}Na VGC, however as figures V.E.22–24 illustrate, variations from 50% to a factor of 2 are observed for different phases, whereas the P23a ^{24}Na VGC is flat with VGC (see figure VI.D.3). The structure in the ^{24}Na VGC suggests a correlation between the veto-rate environment and time after SAA. In principle, the expected distribution could be calculated by taking into account the ^{24}Na activation and the SAA-rigidity geometry experienced by COMPTEL in orbit.

In figures V.E.22–25 I have also plotted the 2.7–4.2 MeV ToF-peak VGCs for the same observations. The ^{24}Na counts in the 2.7–4.2 MeV region are also shown together with the ^{24}Na-subtracted ToF-peak VGC. The non-linear features in the 2.7–4.2 MeV ToF-peak rate are due to the ^{24}Na component (or in general the long-lived component). The ^{24}Na-subtracted ToF-peak VGC are once again linear with only the prompt and CDG components (Kappadath et al. 1997). The effects of the 2.6 and 3.0 MeV are ignored here. The detailed calculation the CDG flux taking into account the contribution from these lines is presented in section VI.D.

The conclusion we draw from the individual phases ^{24}Na VGCs are (1) the ^{24}Na VGCs are not a constant but show complex structure with veto rate; (2) the observed long-lived background structure in veto space is phenomenological; and (3) subtracting the ^{24}Na

components first from the 1gToF peak rates results in VGCs that contain contributions from only the CDG counts and prompt background. They can be subsequently extrapolated to remove the prompt background.

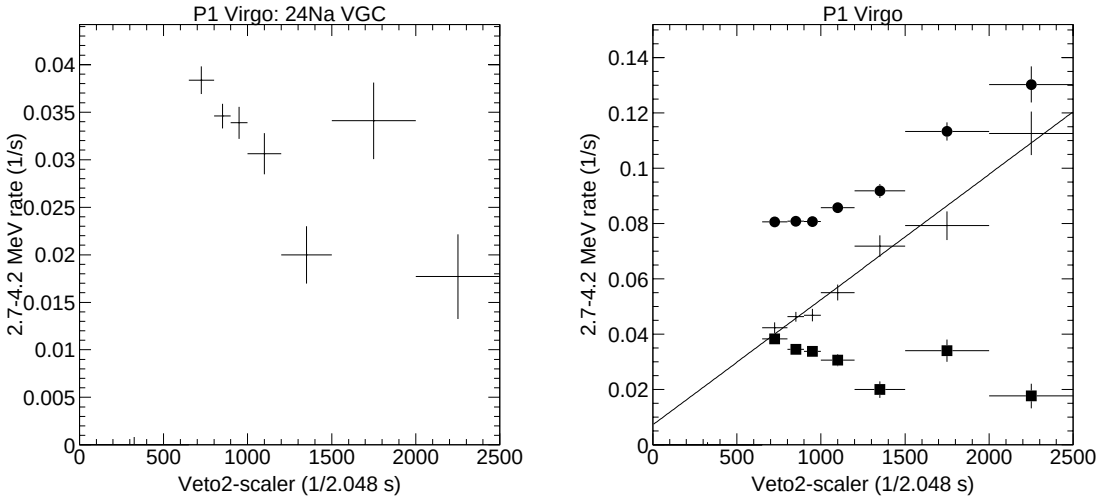

Figure V.E.22 P1V data (a) the ^{24}Na VGC and (b) the 2.7–4.2 MeV VGC; circle: ToF-peak, +: ^{24}Na, square: ToF-peak–^{24}Na.

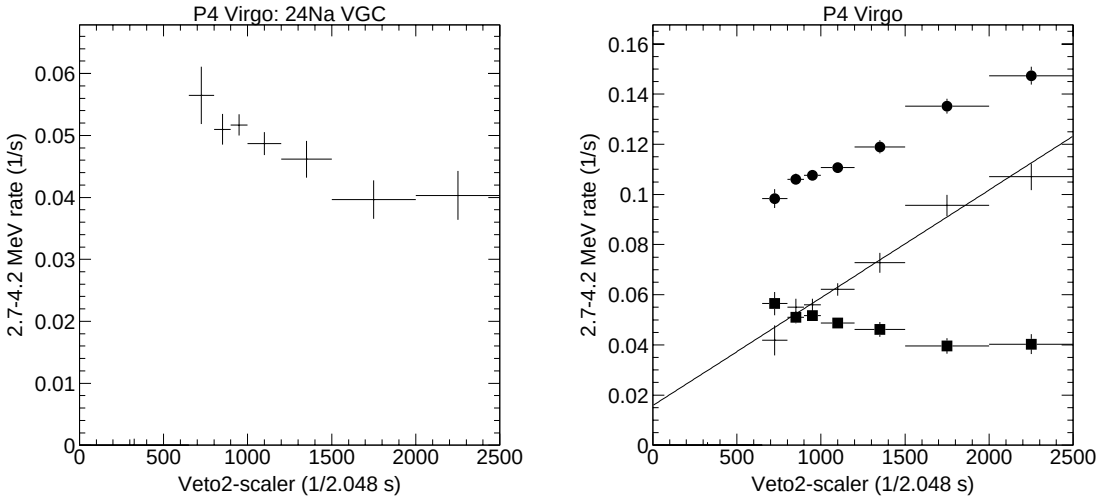

Figure V.E.23 P4V data (a) the ^{24}Na VGC and (b) the 2.7–4.2 MeV VGC; circle: ToF-peak, +: ^{24}Na, square: ToF-peak–^{24}Na.

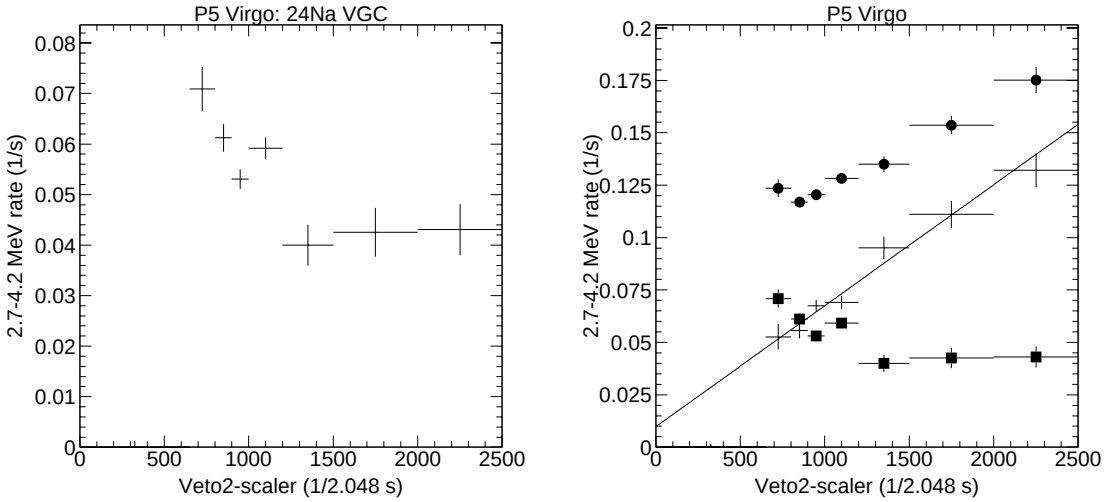

Figure V.E.24 P5V data (a) the ^{24}Na VGC and (b) the 2.7–4.2 MeV VGC; circle: ToF-peak, +: ^{24}Na, square: ToF-peak–^{24}Na.

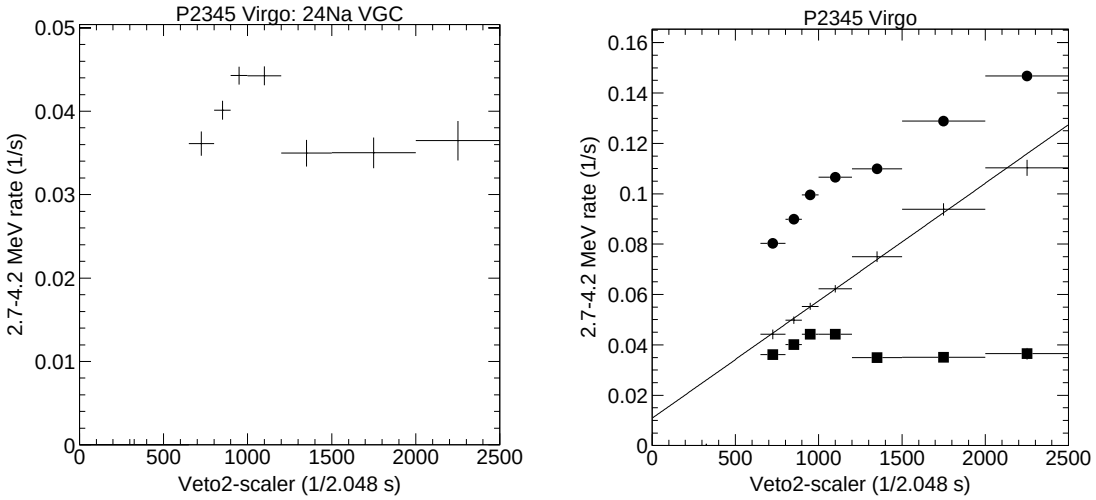

Figure V.E.25 P2345V data (a) the ^{24}Na VGC and (b) the 2.7–4.2 MeV VGC; circle: ToF-peak, +: ^{24}Na, square: ToF-peak–^{24}Na.

The ^{24}Na VGCs for combined Phase data: "veto-excess"

The ^{24}Na VGC for the P2345 combined data is shown in figure V.E.25. The ^{24}Na VGC is very different than the individual phase ^{24}Na VGCs. The P2345 combined data show a strong excess, dubbed the *veto-excess* between 800–1000 rate values (Weidenspointner et al. 1997). This excess is also seen in the 2.7–4.2 MeV ToF-peak VGC. Subtracting the ^{24}Na contributions removes this structure and effectively linearize the ToF-peak VGCs (Kappadath et al. 1997).

Clearly the individual phases do not show the veto-excess as is seen in the combined data. The excess is an artifact of adding data with varied activation. To understand how the excess is created we first need to realize that (1) the intrinsic ^{24}Na activity varies from phase to phase due to the varied SAA dosage; (2) the distribution of veto-rates is skewed with a peak between 800 and 1000 rate and a flat tail extending to higher rate values (see figure V.E.26); (3) to determine the average rate for the combined dataset, all of the counts are added from each veto-bin and divided by the total exposure in each veto bin (identical to taking the weighted average of the individual rates); and (4) the total exposure for the different phases are different.

An explanation for the veto-excess

To illustrate the generation of a veto-bump, we sum two constant VGCs at different intensities with the veto exposure typical of COMPTEL data. Assume constant count rates in Phase 4 and Phase 2 Virgo observations at 20 and 10 (1/s), respectively (see figure V.E.27). The exposures for each veto bin in the two phases are plotted in figure V.E.27.

Each phase has the same count rate, but since the exposure time is different for different veto bins the total counts vary between the veto bins within a phase. Adding the counts from each veto bin for both phase and dividing by their total livetime results in a VGC plotted as "average rate" in figure V.E.27. The average rate is not a constant rate in veto but show a veto-excess around 1000 veto rate. Since the phase 4 data has a higher rate and longer exposure, the average rate is more heavily weighted by phase 4 rate resulting in a veto-excess.

The creation of the veto excess is due to (1) the difference in total livetime for the two phases as the average rate for each phase is weighted by its exposure within each veto bin; (2) the difference in count rates for the two phases because the average rate depends on the total counts; and (3) the non-uniform exposure for the veto bins since different veto rates are weighted differently due to the first two effects [see Weidenspointner 1998].

The correct technique to account for the long-lived and prompt background below 4.2 MeV is as follows: The E2 fits as described in section V.D is used to compute the isotope intensities as a function of veto rate, effectively producing the VGCs for the long-lived background component. Then subtract the contributions of long-lived background

components from the ToF-peak rates. The long-lived background corrected VGCs now contain only the prompt background and CDG counts. Because we have explicitly subtracted the long-lived background, their complex structure in veto-space does not influence the veto-extrapolation. The long-lived background corrected VGCs are linear and an extrapolation to zero veto rate will yield the CDG count rate [see Weidenspointner 1998].

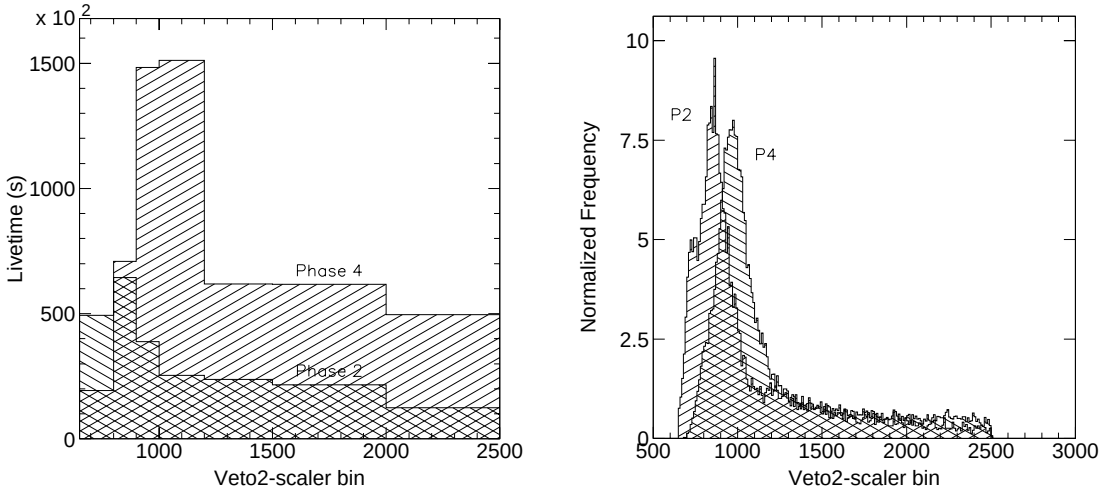

Figure V.E.26 The non-uniform veto exposure, typical of COMPTEL data, for Phase 2 and Phase 4 Virgo observations.

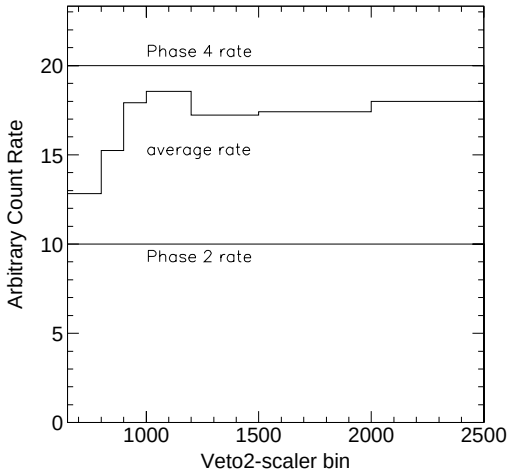

Figure V.E.27 The veto-excess constructed by averaging two constant rates.

The VGCs for various line components

Besides the VGCs for the 2.2 MeV, ^{24}Na and ^{40}K lines, we can construct VGCs for other long-lived background components too. The 1.8 MeV (^{28}Al) VGC (P23a data) is plotted in figure V.E.28. Its linear behavior with veto rate suggests a prompt emission. The short half-life of the ^{28}Al isotope together with the prompt VGC for the 1.8 MeV line in E2 adds support to associating the 1.8 MeV line in E2 with the ^{28}Al isotope decay.

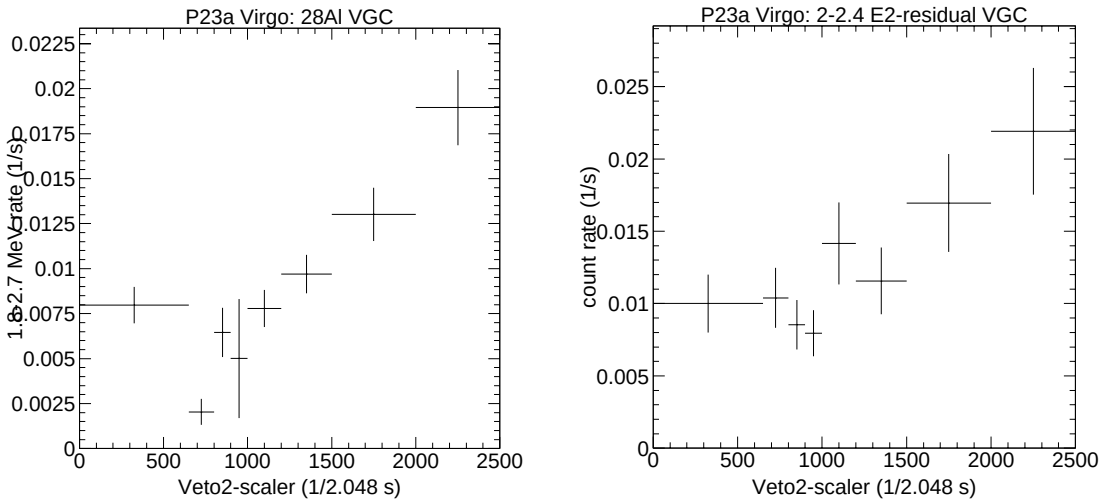

Figure V.E.28 The VGC for the 28Al isotope and the 2-2.4 MeV excess in the E2 spectrum — prompt background.

The 2000-2400 keV excess VGC (P23a data) is plotted in figure V.E.28. The linear behavior for this excess also suggests a prompt origin. The VGCs for ^{22}Na and the 1.4 MeV line in E2 (P2345 data) are shown in figures V.E.29. A veto excess is evident for both lines. The ^{22}Na and 1.4 MeV line VGCs for P23a data are shown in section VI.F.

The P4 and P5 2.6 MeV gaussian VGCs are plotted in figures V.E.30. Both VGCs are indicative of a prompt origin for the 2.6 MeV line. The P4 and P5 2.9 MeV gaussian VGCs are plotted in figures V.E.31, they are both relatively flat indicative of a long-lived origin of the 2.9 MeV excess.

Of the four unidentified features, the 1.4 and 3.0 MeV lines appear to originate from long-lived isotopes, whereas the 2.6 MeV line and the 2000-2400 keV excess in E2 appears to be prompt in nature. The suggestions for a prompt or a long-lived nature for the

unidentified residual are used in the CDG analysis to properly account for their contributions in the data.

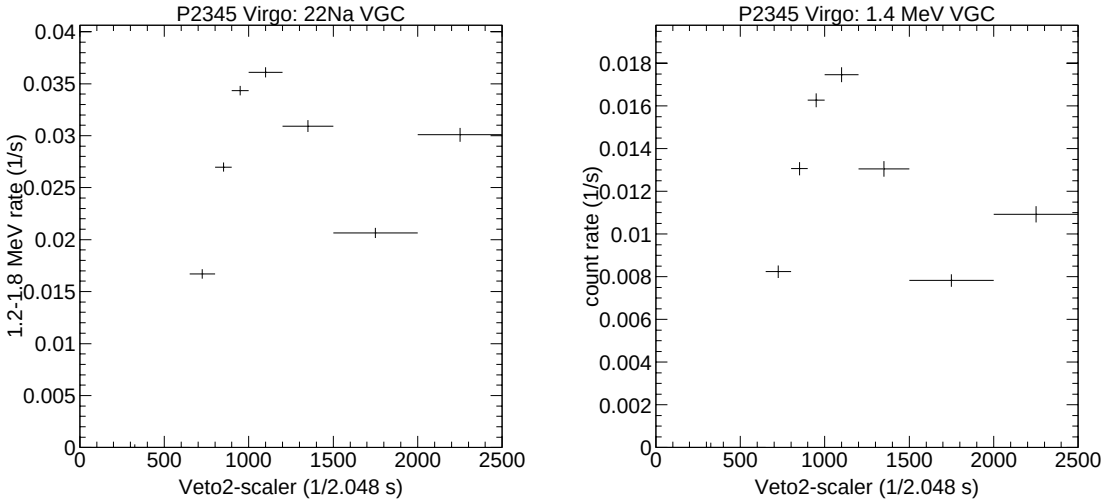

Figure V.E.29 The VGCs for ^{22}Na and the 1.41 MeV peaks in the E2 spectrum — long-lived background.

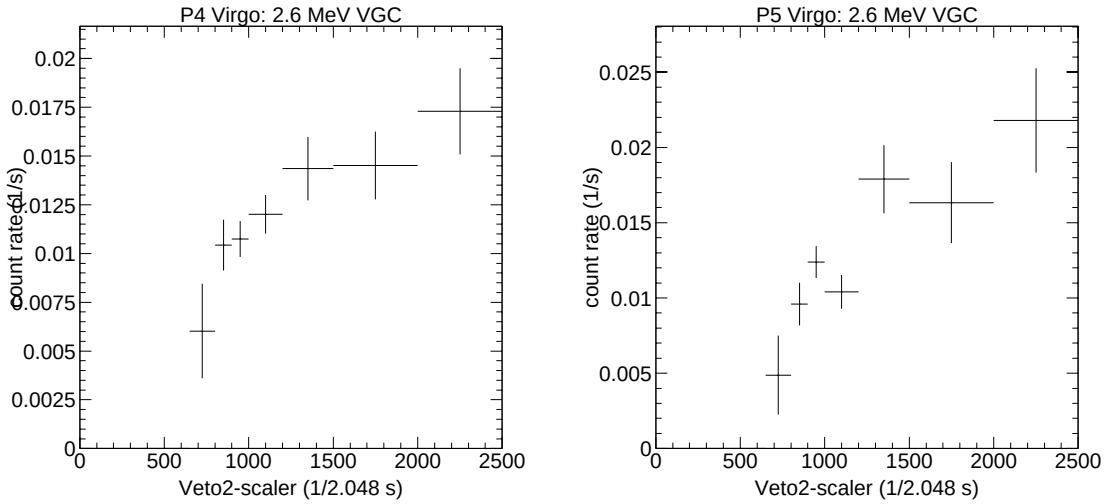

Figure V.E.30 The 2.58 MeV VGC in Phases 4 and 5 — prompt background.

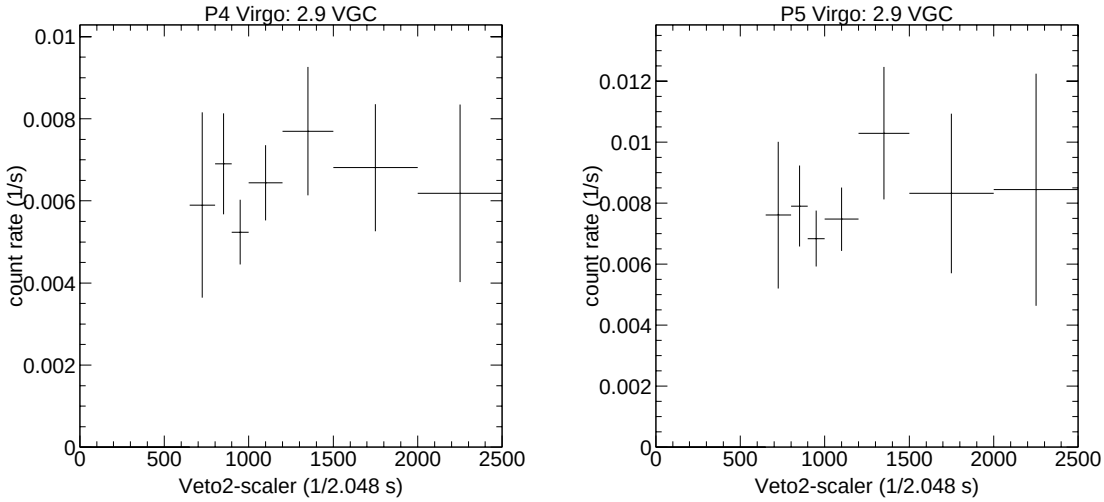

Figure V.E.31 The 2.94 MeV VGC in Phases 4 and 5 — long-lived background.